

Magnetic cooling and on-chip thermometry for nanoelectronics below 10 mK

Inauguraldissertation

zur

Erlangung der Würde eines Doktors der Philosophie

vorgelegt der

Philosophisch-Naturwissenschaftlichen Fakultät

der Universität Basel

von

Mario Palma

aus Italien

Basel, 2017

Originaldokument gespeichert auf dem Dokumentserver der Universität Basel

edoc.unibas.ch

Genehmigt von der Philosophisch-Naturwissenschaftlichen Fakultät auf Antrag von

Prof. Dr. D.M. Zumbühl

Prof. Dr. C. Enss

Prof. Dr. R. P. Haley

Basel, den 19. September 2017

Prof. Dr. Martin Spiess

Dekan

"Nos esse quasi nanos gigantum humeris insidentes"

Bernardo di Chartres

Abstract

Cooling of electronic devices below 1 mK is a challenging task, since the thermal coupling with the dilution refrigerator becomes weak at low temperatures and electronic devices are extremely susceptible to external heat leaks such as microwave radiation and electrical noise. Despite these technological challenges, there is a completely new world of physics which can be explored once low temperatures are achieved.

To reach such ultra-low temperatures, we implemented a parallel network of Nuclear Refrigerators, to adapt magnetic cooling to electronic transport measurements. The cooling scheme relies on the cooling of each individual lead by its own nuclear refrigerator to transfer cooling power down to the sample. Here, we present the implementation of a parallel network of nuclear refrigerators for the first time on a cryo-free system. One challenge is the increased vibrations level compared to the wet cryostat, but a careful damping of the vibrations is possible, thus enabling low temperature experiments. The setup successfully cools the electronic temperature of the nuclear refrigerant down to 150 μK and limits a residual heat leak of few nW per mole of copper, allowing to stay below 1 mK for several days. A simple thermal model capturing the demagnetization process, the heat leak, the coupling between electron and nuclei as well as the efficiency of the process typically above 80 %.

To characterize the cooling capacity of our system, we cool several electronic devices well below 10 mK. We cool a normal metal-insulator-superconducting tunnel junction down to 7.3 mK. Further lowering temperatures might be limited by the heat release of the socket. However, a theoretical estimate shows that such a device has the potential to reach 1 mK, since the overheating effects turn out to be negligible. Indeed, by using the thermal broadening of sub-gap current steps, we demonstrate the cooling of the tunnel junction down to 4 mK. These steps are novel features which are weakly-coupled and more robust than the conventional NIS thermometry, and we can model them as Andreev bound states enhanced by disorder and the geometry of the junction. Addi-

tionally, other physical properties of the junction are investigated experimentally and numerically, such as two-particle sub-gap tunneling current promoted by the disorder and the geometry of the junction and magnetic field suppression of a minigap.

Further improvement on the cooling of the electronic device is achieved by on-chip magnetic refrigeration. We demonstrate magnetic cooling of an array of Coulomb Blockade Thermometers with huge copper islands. The lowest temperature reached is 2.8 mK, which is the lowest temperature measured to date in a solid state electronic device. The reduction in temperature is roughly a factor 8 during the demagnetization process, showing an improved efficiency of the cooling technique compared to the previous experiments. The temperature might possibly be further reduced below 1 mK, by introducing non-inductive filters and damping more the vibrations, which would lead to a lower precooling temperature and an improved efficiency of the on-chip magnetic cooling.

Acknowledgement

I would like to thank Prof. Dr. Dominik Zumbühl to give me the opportunity to do my PhD thesis in his group. He is a very supporting supervisor and we had always valuable discussions about the physics of the project and the technical challenges in the construction of the setup. I am grateful for his supporting words, which gave me the strength to face the initial difficulties of the project, when nothing was working.

I would like to thank Prof. Dr. Christian Schönenberger and the Swiss Nanoscience Institute for the financial support of my PhD program and for organizing many interesting social activities. On this note, I am very thankful to Dr. Michel Calame for the organization of the several annual meetings and winter schools, where I learned a lot from the inspiring talks of the invited speakers. The PhD program of the Swiss Nanoscience Institute gave me the opportunity to share experience and discuss with other PhD students coming from different fields of the nanosciences. Additionally, I am grateful to the all administrative staff of the Swiss Nanoscience Institute in the persons of Audrey Fisher, Claudia A. Wirth, Dr. Kerstin Beyer-Hans, Dr. Michèle Wegmann and Dr. Christel Möller.

During this work we had a fruitful collaboration with the group of Prof. Dr. Jukka Pekola, to design and to develop on-chip thermometer below 10 mK. In particular, I would like to thank Dr. Matthias Meschke and Dr. Anna Feshchenko for the fabrication of the devices used in this thesis and for the discussions about the working principles of the devices.

All this work has been possible thanks to the former members of the the Microkelvin project, which started and advanced the project before me. In particular, I thank Dr. Dario Maradan, who introduced me to the world of low temperature physics. Together, we built the setup presented in this thesis and solved all the huge amount of troubles caused by the Bluefors fridge in the first two year. Then, I would like to thank Dr. Lucas Casparis for his availability to discuss about the physics of the project

and for his useful advises, which guided me along my time as a PhD.

One of the strength of our group is the nice working environment. All the group member help each other and discuss with each other. I am grateful to Dr. Christian Scheller, who supervised me for the last year and giving many good inputs to reach the good results presented in this thesis. I would like to thank Dr. Liuqi Yu, who helped me with the corrections of this thesis and for the time shared outside of work. Then, I am thankful to Pirmin Weigele for sharing with me the PhD since the first day. I consider him a good friend and good luck for your defense. I would also like to thank all members of the Zumbühl group that I met during my time in Basel.

Special thanks to the mechanical workshop of the Physics department of the University of Basel to realize in a short time every mechanical piece needed for the setup. Additionally, I am grateful to Astrid Kalt and Barbara Kammermann for taking care of my bureaucracy documents.

I am thankful to all my family to support me along the four years of my PhD. Then I would like to thank Olimpia Tamaro, who has been always on my side and helped me emotionally to overcome the stressful periods along my PhD thesis.

Last but not least, I am grateful to all the people met here in Basel, who gave me the opportunity to enjoy my time in Basel.

Contents

Contents	I
1 Introduction	1
2 Magnetic cooling for microkelvin nanoelectronics on a cryofree platform	10
2.1 Introduction	12
2.2 Nuclear Refrigerator Network on a Cryofree Platform	13
2.3 Noise Thermometry	16
2.4 Nuclear Refrigerator Performance	19
2.5 Conclusions	26
2.6 acknowledgments	26
2.7 Supplementary Material	27
2.7.1 Setup	27
2.7.2 High Performance System	28
2.7.3 Warm up	31
2.7.4 Socket	33
2.7.5 Gradiometer Design	35
3 Thermal model AND process	37
3.1 Introduction	37
3.2 Theory of the Adiabatic Nuclear Demagnetization	38
3.3 Degrees of Freedom in a Cu Plate	40
3.3.1 Electron-Phonon Coupling	41

3.3.2	Hyperfine Interaction	41
3.4	Simulation AND	44
4	Tunnel-Junction Thermometry Down to Millikelvin Temperatures	49
4.1	Introduction	50
4.2	Theoretical Background	51
4.3	Experimental Realization and Measurement Techniques	54
4.4	Results and Discussion	56
4.5	Thermal Model	58
4.6	Conclusions	59
4.7	Appendix	60
5	Sub-gap bound-states in normal metal-insulator-superconductor junctions	67
5.1	Introduction	68
5.2	NIS Device and Setup	69
5.3	Temperature and Thickness Dependence	71
5.4	In-plane Magnetic Field	74
5.5	Discussion and Model	76
5.6	Conclusion	79
5.7	Supplementary material	79
5.7.1	Current Steps in Differential Conductance	79
5.7.2	Numerical Simulation	80
5.7.3	Magnetic Field Dependence	84
5.7.4	Resonances versus B -field	85

5.7.5	Background Conductance and Minigap	86
5.7.6	Photon Absorption	87
5.7.7	Perpendicular B-field	90
5.7.8	Demagnetization	92
6	On-and-off chip cooling of a Coulomb blockade thermometer down to 2.8 mK	94
6.1	Introduction	95
6.2	Experimental Setup and CBT Device	96
6.3	Measurements	99
6.4	Magnetic Cooling of a CBT and Cu Plate	102
6.5	Thermal Model	104
6.6	Conclusion	106
6.6.1	Acknowledgments	107
6.7	Supplementary Material	107
6.7.1	Sample Fabrication and Mode of Operation	107
6.7.2	Experimental Setup	110
6.7.3	Warm up With Heat Applied to the Cu Plates	110
6.7.4	High Charging Energy CBT	112
6.7.5	Vibrations and Electrical Noise	113
7	Conclusion & Outlook	116
	References	120
	List of Figures	137

1 Introduction

Modern physics revolves around quantum mechanics, which gives a mathematical description of matter, radiation and the interactions among them in the microscopic world. Usually, the quantum mechanical phenomena are characterized by small length scales and small energies. Therefore, at room temperature most of these phenomena are not observable since typical energy scales are much smaller than the thermal excitation at room temperature. To overcome this limitation, scientists and engineers started to develop cooling techniques to decrease the temperature and make the exploration of uncharted sections of quantum mechanics possible. First, cooling techniques were obtained by liquefying gases such as N_2 and O_2 reaching temperatures below 100 K at the end of the 19th century. An important step forward has been made in 1908, when the Dutch scientist and Nobel laureate Heike Kamerlingh Onnes liquified He^4 for the first time and reached a temperature of 4.2 K [1].

As shown in Fig. 1.1, many techniques have been developed in the past hundred years to reach even lower temperatures, which are several orders of magnitude lower than the lowest natural temperature in the universe. The first technique able to cool below 1 K was the electronic magnetic refrigeration performed with paramagnetic salts, e.g. Chromium Potassium Alum (CPA), Cerium Magnesium Nitrate (CMN), Ferric Ammonium Alum (FAA). This technique is based on the adiabatic demagnetization of the electronic magnetic moments of the ions within the salt. The lowest temperature achievable is given by the ordering temperature of the paramagnetic salt, as low as 2 mK [1] for standard paramagnetic salts, see Fig. 1.1. A mixture of $He^3 - He^4$ isotopes is used in the dilution refrigeration technique to cool down to roughly 10 mK, where specially optimized setups can reach a lowest temperature of ~ 2 mK [2, 3] in continuous operation mode. To reach temperatures below 1 mK, it is necessary to use the magnetic demagnetization of nuclear magnetic moments instead of electronic magnetic moments, since for the nuclei the magnetic ordering temperature is determined by the

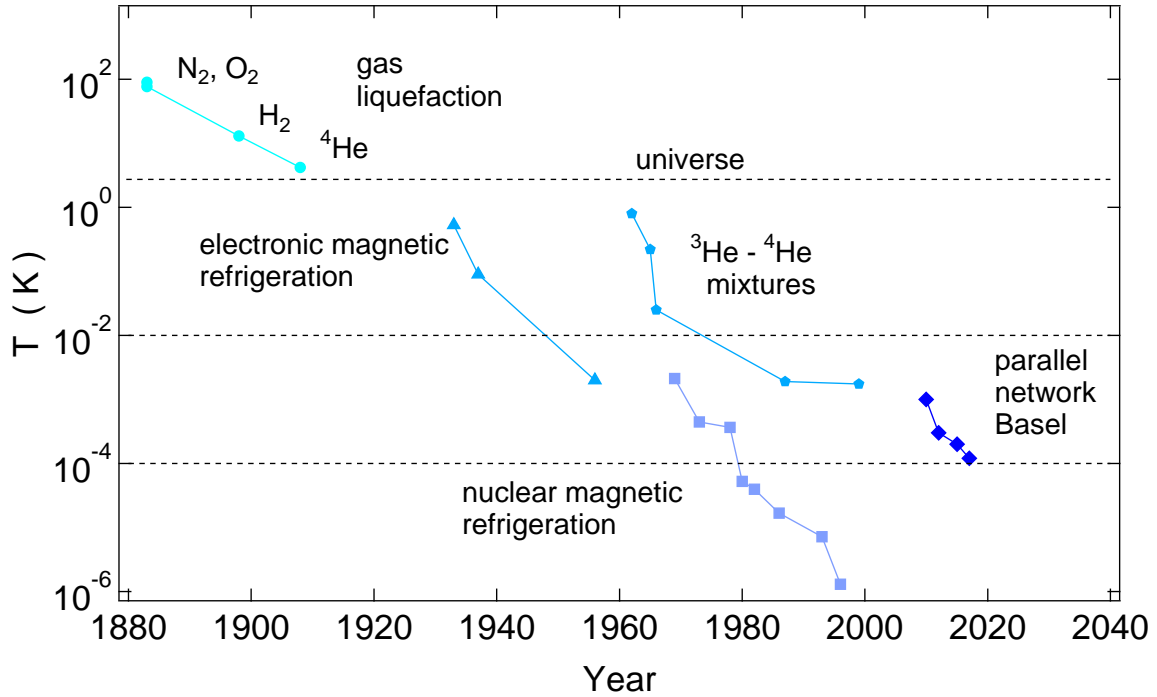


Figure 1.1: History of refrigeration techniques developed in the past 160 years. The graph reproduces a previous graph shown in Ref. [1], but we add the experimental results obtained with a nuclear refrigeration network. Note that the network of nuclear refrigerator is not an entirely new technique, but rather is adapting nuclear magnetic demagnetization for the specific needs of cooling nanoelectronic devices.

weak dipole-dipole interaction of the nuclei and it is well below $\sim 1 \mu\text{K}$ [1].

Nowadays, dilution refrigerators are widely used in transport experiments to investigate physics on low energy scales. Some new physical phenomena, however, are predicted to manifest at energy scales below 1 mK only, such as fragile fractional quantum Hall states [4–6], with small energy gaps on the order of few mK. These states are predicted to exhibit non-Abelian statistics, which could be used for topological quantum computation [7–10]. Furthermore, novel electron mediated nuclear spin phases [11–13] are predicted to occur at temperatures below ~ 1 mK, where nuclei should align ferromagnetically with helical order, eliminating nuclear spin fluctuations, which are predicted as main source of decoherence in semiconductor based spin qubit [14, 15]. In addition, the coherence of semiconductor and superconducting qubits [16, 17] as well as hybrid Majorana devices [18–20] could benefit from the lower temperatures.

Often electronic temperatures in transport experiments are roughly ~ 100 mK, despite

the fact that they are performed in dilution refrigerators with a far lower base temperatures. Since electronic devices are susceptible to external heat leaks such as microwave radiations, heat release and electrical noise.

Tremendous efforts are necessary for cooling of electrons below 10 mK. This milestone has been initially reached by the quantum Hall community, by utilizing He^3 immersion cells. In these experiments a semiconductor device is glued onto a heat exchanger to provide cooling through the substrate and the sample is electrically connected with In contacts to Ag sinters with a large surface area to reduce the Kapitza resistance. These parts are located inside an immersion cell, which is cooled down to 0.5 mK with a PrNi_5 magnetic refrigerant. Despite the low temperatures of the He^3 the device is cooled down only to 4 mK [4, 21–25]. This approach relies on cooling electrons through electron-phonon coupling and the Kapitza boundary resistance, both of become weak at low temperatures, due to their strong temperature dependence. To overcome the limits of this approach and reach lower temperatures a new approach is needed.

In order to pursue our goal, we need to find a cooling technique, which is able to reach μK temperatures, and then adapt it for transport experiments. The most powerful technique utilized to cool to the μK range is adiabatic nuclear demagnetization [1, 26, 27], which was already very well established in the low temperature physics community. It was used in many low temperature physics experiments [28–30] to cool nuclear spins systems in metal or superfluid He^3 . However, these experiments utilized a massive piece of nuclear refrigerants, e.g. Cu, Pt, PrNi_5 , which are not suitable to perform transport experiments where we need well cooled individual leads to avoid transport of heat to the sample. Therefore, we built a parallel network of Nuclear Refrigerators (NRs) [31–33], where each experimental lead has its own nuclear refrigerator, to cool electronic devices through the leads. The cooling scheme is designed to take advantage of the electronic conduction, which leads to a heat flow scaling with T^2 , instead of the T^5 dependence of the electron-phonon coupling, which is therefore strongly suppressed at low temperatures. The first prototype of NRs was successfully implemented in a wet

dilution refrigerator and cooling well below the dilution refrigerator temperature of 10 mK, has been demonstrated [31]. Figure 1.1 shows the progress obtained in Basel in the implementation of the network of NRs, which is a new concept aimed to achieve μ K temperatures in nanoelectronic devices.

Once the low temperature setup is available, the next challenging task is to transfer the cooling capacity to electronic device. It is extremely difficult to cool efficiently electronic devices below 10 mK, since the thermal coupling to the refrigerator becomes weak at low temperatures. Further, they are extremely susceptible to various sources of heat leaks such as radiation, electrical noise or heat release. Therefore, it is important to properly shield and filter the setup, thus additional effort needs to be spent to design multiple shields, attached at different temperatures stages to progressively reduce the black body radiation. In addition, every lead is heavily filtered, by using RC filters and home built microwave filters [34].

In the recent years, the interest for ultra-low temperature systems has been increasing, due to the arrival of a new cryogen-free technology, which makes it possible to perform low temperatures experiments everywhere, independently of the He⁴ liquifying facilities. This gains importance because Helium is a non-renewable resource extracted mostly from natural gas, its price has constantly been increasing in the last decades due to the limitation on the extraction and due to the increasing demand of Helium in several applications, e.g. medical imaging scanners and semiconductor industry [35, 36]. For these reasons, it is further important to have a recovery system for Helium, however even the best recovery system has losses on the order of ten percent. An economical solution is given by the cryogen-free system, where a fixed amount of ⁴He is used in the closed cooling cycle of the system. Additionally, wet cryostats offer very limited space for the experiment, and suffer from regular, periodic liquid Helium transfers interrupting and often warming up the experiment. However, the cryogen-free systems have an increased vibrations level compared to traditional wet systems, leading to additional heat leaks that make the implementation of an AND setup on these systems

even more challenging.

The first attempts to combine AND with cryo-free refrigerator, was demonstrated in experiments using a massive pieces of nuclear refrigerants [37–39], which are unpractical to use transport experiments, since electrically isolated leads are required. As a consequence, using a single nuclear refrigerant the thermalization of the leads should occur through an insulator, making the cooling inefficient. Therefore, we were motivated to show that our approach of individual parallel NRs can be implemented in cryogen-free setup to directly perform transport experiment. By ad-hoc modifications of the NR design we demonstrate their implementation on a Bluefors cryo-free dilution refrigerator. We prove cooling of the NRs down to $150\ \mu\text{K}$, which is measured with a magnetic field fluctuation thermometer implemented in our setup. In addition, a simple thermal model is presented, which describes well the demagnetization and an improved efficiency of the AND process to more than 80 % even at low magnetic fields. The details of the setup are described in chapter 2, while more details about the model can be found in chapter 3.

Thanks to NRs, we have the possibility, to cool electronic devices below 10 mK, therefore we need to find on-chip thermometers to measure such low temperatures. Jukka Pekola and his group are pioneers and a leading group of on-chip cooling and thermometry. For this reason we collaborate to improve the design and to test different on-chip thermometers such as arrays of metallic Coulomb Blockade Thermometers (CBTs) and a single junction normal metal-insulator-superconducting (NIS) device. Both on-chip thermometers demonstrated cooling below the mixing chamber temperature, proving the effectiveness of our cooling scheme. In particular for the NIS junctions, we demonstrate operation down to $\sim 7\ \text{mK}$, however our theoretical model shows the opportunity to cool it down to 1 mK, see chapter 4.

A more careful analysis of the NIS devices reveals new physics, which is manifested through sharp current steps in the sub-gap region of the I-V curve. The steps show thermal broadening down to 4 mK, which serves as primary on-chip thermometer. In

addition they show a clear dependence on the thickness of the metal layer and on the in-plane magnetic field. Thermal cycling of the device suggests disorder within the junction as possible origin of the steps. Numerical calculation shows that the steps can be explained with Andreev bound states enhanced by the disorder and the geometry of the junction. Furthermore, the simulation predicted a sub-gap conductance given by two-particle tunneling current due to interference effects enhanced by the geometry of the junctions and the appearance of a minigap suppressed by the magnetic field. The sub-gap steps are the topic of the chapter 5 of this thesis work.

Despite the important technological achievements in cooling of electronic devices, it is still challenging to reach electron temperature below 1 mK. Remarkable results have been achieved by using CBT devices with electroplated islands, which were cooled as low as 3.8 mK in an He³ immersion cell [40] and to ~ 5 mK by on-chip magnetic cooling [41]. Cooling through the leads is efficient for samples, which are connected to the leads through a low resistive path. However the cooling becomes rather inefficient for high resistance devices with more than one tunnel junction in series e.g. CBTs. For this reason, we changed our approach going from cooling electronic devices through the leads to direct on-chip demagnetization cooling of Cu island of the CBT array. Metallic CBTs with huge Cu islands (with a volume of $\approx 800 \cdot 200 \cdot 0.2 \mu\text{m}^3$) offer a reasonable spin reservoir together with a partial thermal isolation of the device due to the high resistance of the array structure. We demonstrate on-chip magnetic cooling of the CBT down to 2.8 mK, which is the lowest temperature reported so far, with an increased cooling efficiency of the device compared to the previous experiments, leading to a factor ~ 8 in temperature reduction. The experimental findings about the on-chip magnetic cooling are described in chapter 6.

Here, we summarize the progress in the design and the fabrication of on-chip thermometers such as NIS thermometers and CBTs, which resulted in lower temperatures measured in the last decades in several research groups. To give an idea of the progress in cooling of the on-chip thermometers, we plot in Fig. 1.2.(a) and (b) a selection of

the lowest temperatures for NIS and CBT for each year. The Table. 1 shows some of the lowest temperatures measured at this time. In the Ref. [42], corresponding to point (1) in Fig. 1.2.(a), a saturation of the thermometer around 70 mK is observed while the temperature of the fridge goes down to 40 mK. The saturation maybe attributed to a poor thermalization of the electrons in the normal metal lead or at a large electrical noise. For several years, it has been challenging to cool such devices below 10 mK, until in the Ref. [43], see point (3) Fig. 1.2.(a), where we introduced large metallic pads to ensure a good thermalization of the electrons. Additionally, the setup is improved compared to the early work of Nahum, to reach lower temperatures. The lowest temperature (point (4) in Fig. 1.2.(a)) is reached by using the thermal broadening of the sub-gap steps appearing in the I-V curve of a NIS junction down to 4 mK.

Remarkable results have been obtained also in cooling of the CBT in the past 20 years, demonstrating a reduction of the CBT temperature from 4 K measured by Pekola in the 1994 (point (5)) down to 2.8 mK presented in this thesis work, see Fig. 1.2.(b). Reaching temperature below 10 mK has been really challenging for many years and it required improvements in the design of the CBTs and of the experimental setups. As reported in Ref. [34] (points (8) and (9)) the introduction of microwave filters helped to further lower the temperature, by reducing electrical noise and high-frequency radiation. To further decrease the temperature of the CBT it is necessary to reduce the charging energy by enlarging the volume of the CBT island. For this reason in Ref. [40, 41], see points (10) and (11) Fig. 1.2.(b), the volume has been increased, by electroplating a thick metal layer, which also helps the thermalization of the electrons in the CBT through the substrate, by increasing the strength of the electron-phonon coupling. In the recent year the magnetic cooling of CBT give the opportunity to further lower the temperature, see (11) and (12).

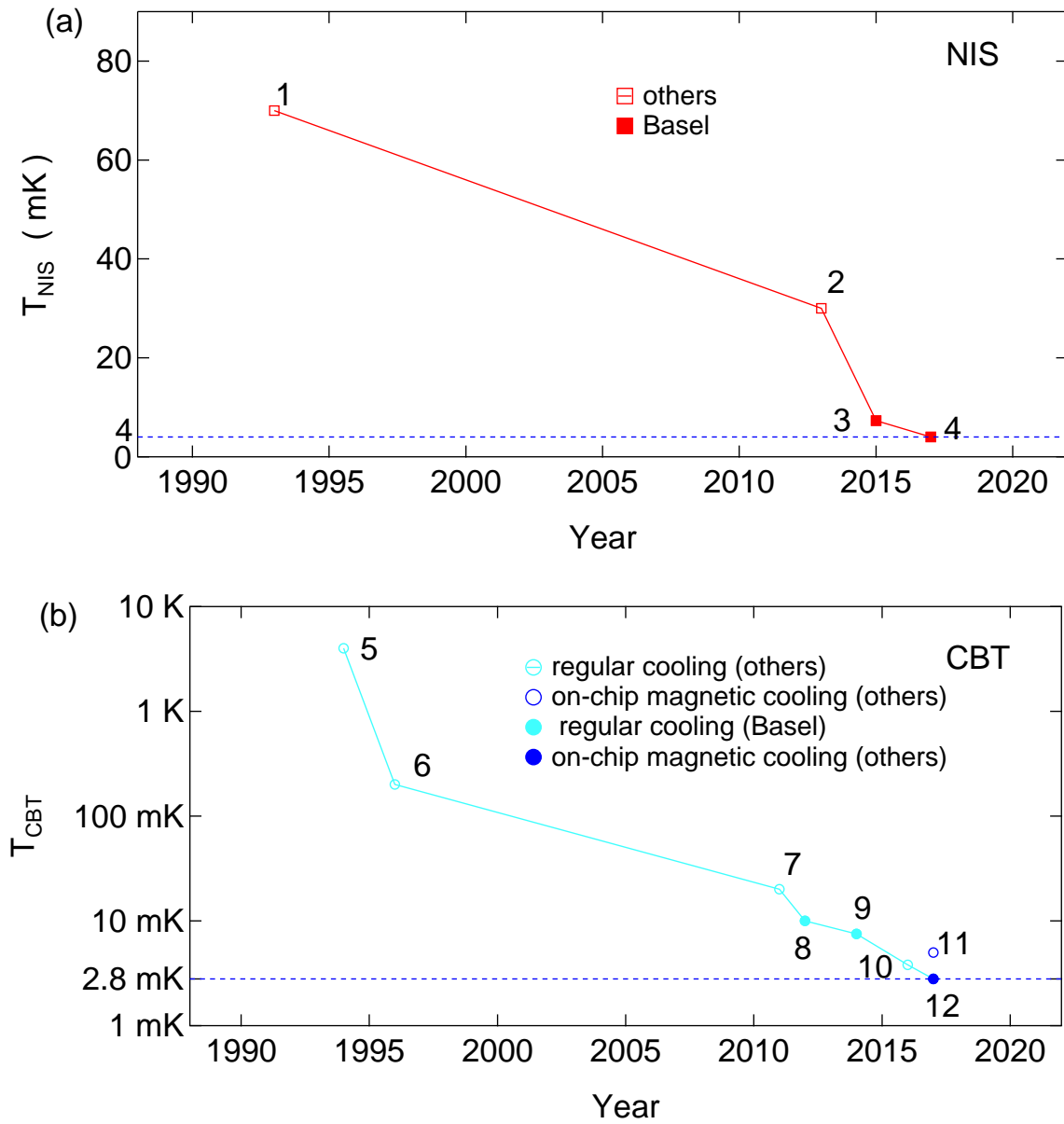


Figure 1.2: (a) Lowest temperatures measured in the past 30 years in NIS junctions. (b) Lowest temperatures measured in past 30 years in CBTs. The dashed blue lines indicate the lowest temperatures reached for NIS junctions and CBTs

references	lowest T	location
(1) M. Nahum, <i>et al.</i> , <i>Appl. Phys. Lett.</i> (1993)	70 mK	NIST (USA)
(2) H. Q. Nguyen, <i>et al.</i> , <i>Phys. Rev. Appl.</i> (2014)	30 mK	Aalto University (Finland)
(3) A. V. Feshchenko, <i>et al.</i> , <i>Phys. Rev. Appl.</i> (2015)	7.3 mK	University of Basel (Switzerland)
(4) M. Palma, <i>et al.</i> in preparation for publication (2017)	4 mK	University of Basel (Switzerland)
(5) J. P. Pekola, <i>et al.</i> , <i>Phys. Rev. Lett.</i> (1994)	4.2 K	University of Jyväskylä, (Finland)
(6) S. Farhangfar, <i>et al.</i> , <i>J. Low Temp. Phys.</i> (1997)	200 mK	University of Jyväskylä, (Finland)
(7) M. Meschke, <i>et al.</i> , <i>Int. J. Thermophys.</i> (2011)	23 mK	Aalto University (Finland)
(8) L. Casparis, <i>et al.</i> , <i>Rev. Sci. Instrum.</i> (2012)	10 mK	University of Basel (Switzerland)
(9) C. P. Scheller, <i>et al.</i> , <i>Appl. Phys. Lett.</i> (2014)	7.5 mK	University of Basel (Switzerland)
(10) D. I. Bradley, <i>et al.</i> , <i>Nat. Commun.</i> (2016)	3.8 mK	Lancaster University (UK)
(11) D. I. Bradley, <i>et al.</i> , <i>Sci. Rep.</i> (2017)	5 mK	Lancaster University (UK)
(12) M. Palma, <i>et al.</i> , in preparation for publication (2017)	2.8 mK	University of Basel (Switzerland)

Table 1: Relevant publications in cooling of NIS (1-4) and CBT (5-12) devices in past 30 years shown in Fig. 2.

2 Magnetic cooling for microkelvin nanoelectronics on a cryofree platform

M. Palma^{*1}, D. Maradan^{1,2*}, D. Casparis^{1,3}, T.-M. Liu^{1,4}, F.N.M. Froning¹ and
D. M. Zumbühl¹

¹ *Department of Physics, University of Basel, CH-4056 Basel, Switzerland*

² *Physikalisch-Technische Bundesanstalt (PTB), Bundesallee 100, 38116
Braunschweig, Germany*

³ *Center for Quantum Devices and Station Q Copenhagen, Niels Bohr Institute,
University of Copenhagen, 2100 Copenhagen, Denmark*

⁴ *Department of Applied Physics, National Pingtung University, Pingtung City,
Taiwan*

* These authors contributed equally to this work.

This chapter was published in *Rev. Sci. Instr.* **88**, 043902 (2017).

Abstract

We present a parallel network of 16 demagnetization refrigerators mounted on a cryofree dilution refrigerator aimed to cool nanoelectronic devices to sub-millikelvin temperatures. To measure the refrigerator temperature, the thermal motion of electrons in a Ag wire – thermalized by a spot-weld to one of the Cu nuclear refrigerators – is inductively picked-up by a superconducting gradiometer and amplified by a SQUID mounted at 4 K. The noise thermometer as well as other thermometers are used to characterize the performance of the system, finding magnetic field independent heat-leaks of a few nW/mol, cold times of several days below 1 mK, and a lowest temperature of 150 μ K of one of the nuclear stages in a final field of 80 mT, close to the intrinsic SQUID noise of about 100 μ K. A simple thermal model of the system capturing the nuclear refrigerator, heat leaks, as well as thermal and Korringa links describes the main features very well, including rather high refrigerator efficiencies typically above 80 %.

2.1 Introduction

As thermal excitations represent an ubiquitous energy scale in solid state systems, advancing to lower temperatures might open up the way to the discovery of new physical phenomena such as fragile fractional quantum Hall states [4] and electron-mediated nuclear phase transitions, both in 2D and 1D systems [11–13]. To investigate such phenomena, one needs to access lower temperatures beyond what a dilution refrigerator could achieve. Adiabatic Nuclear Demagnetization (AND) [27, 31] is a very well established technique with the potential to open the door to the μK -regime for nanoelectronics. In many laboratories, the sample is only weakly coupled to the coldest spot of the refrigerator, resulting in sample temperatures significantly higher than the base temperature of the refrigerator. In order to efficiently couple sample and refrigerator, a parallel network of Nuclear Refrigerators (NRs) was proposed [31, 43], where every lead is well thermalized through the mixing chamber (MC) and has its own NR. Our approach relies on the Wiedemann-Franz cooling of the conduction electrons [32], which is the main cooling mechanism in the mK-regime and below.

The implementation of a parallel network of NRs on a cryofree system is very challenging due to the increased vibration level compared to a wet system. However, cryogen-free platforms will become more important for low temperature experiments, because they offer ample experimental space and operation without liquid helium, thus reducing costs and dependence on helium infrastructures. In addition, particularly referring to AND, cryogen-free systems are suitable for longer precooling and extended hold time compared to the traditional wet system, due to liquid He transfers increasing the temperature of the entire system. First operative AND systems on cryogen-free platforms have been implemented using both PrNi_5 and Cu as nuclear refrigerant [37–39]. In contrast to the single nuclear stage experiment, the parallel network of NRs amends itself for nanoelectronics providing direct cooling of the electrons in each of the wires connected to the sample.

In this article, we present a successful implementation of a parallel network of Cu NRs on a cryogen-free platform demonstrating cooling with high efficiency close to ideal adiabatic behavior down to $150\ \mu\text{K}$. The temperature is measured using an inductive Johnson noise thermometer [44–46], which operates over a broad range of temperatures from 4 K down to $150\ \mu\text{K}$. The noise thermometer is an ideal choice for low temperature applications, because self-heating is reduced due to the inductive read-out and the thermometer has the potential to reach the low μK -regime. We measure field independent heat leaks of less than $2\ \text{nW/mol}$ for magnetic fields below 1 T, allowing the NRs to stay below 1 mK for roughly 50 hours at 80 mT. We model the AND process and obtain a dynamic heat leak independent of the magnetic field ramp rate. Thus, it is possible to increase the efficiency of the AND process by reducing the duration of the B -field ramping.

2.2 Nuclear Refrigerator Network on a Cryogen-Free Platform

Recently, AND experiments have been successfully implemented on a cryogen-free platform, using PrNi_5 and Cu as nuclear refrigerant [37–39]. With PrNi_5 , reaching ultra-low temperatures is restricted to the rather high nuclear ordering temperature ($T \sim 0.5\ \text{mK}$) [1, 47]. In contrast, Cu can be demagnetized down to the low μK regime and it is very easy to work with and to machine, particularly compared to PrNi_5 . The high electrical conductivity of Cu makes it susceptible to eddy current heating, which arises from both ramping of the magnetic field and vibrations in a non-homogenous B -field. The pulse tube (PT) cold head is a powerful source of both cooling and vibrations, making the implementation of AND an exacting task. Adiabatic nuclear demagnetization experiments are very susceptible to heat leaks, increasing temperature and accelerating the warm up of the NRs, thus reducing the hold time. The concept of a parallel network of 16 Cu NRs presented here overcomes these challenges and leads to a straightforward integration of the AND technique into

transport measurement setups.

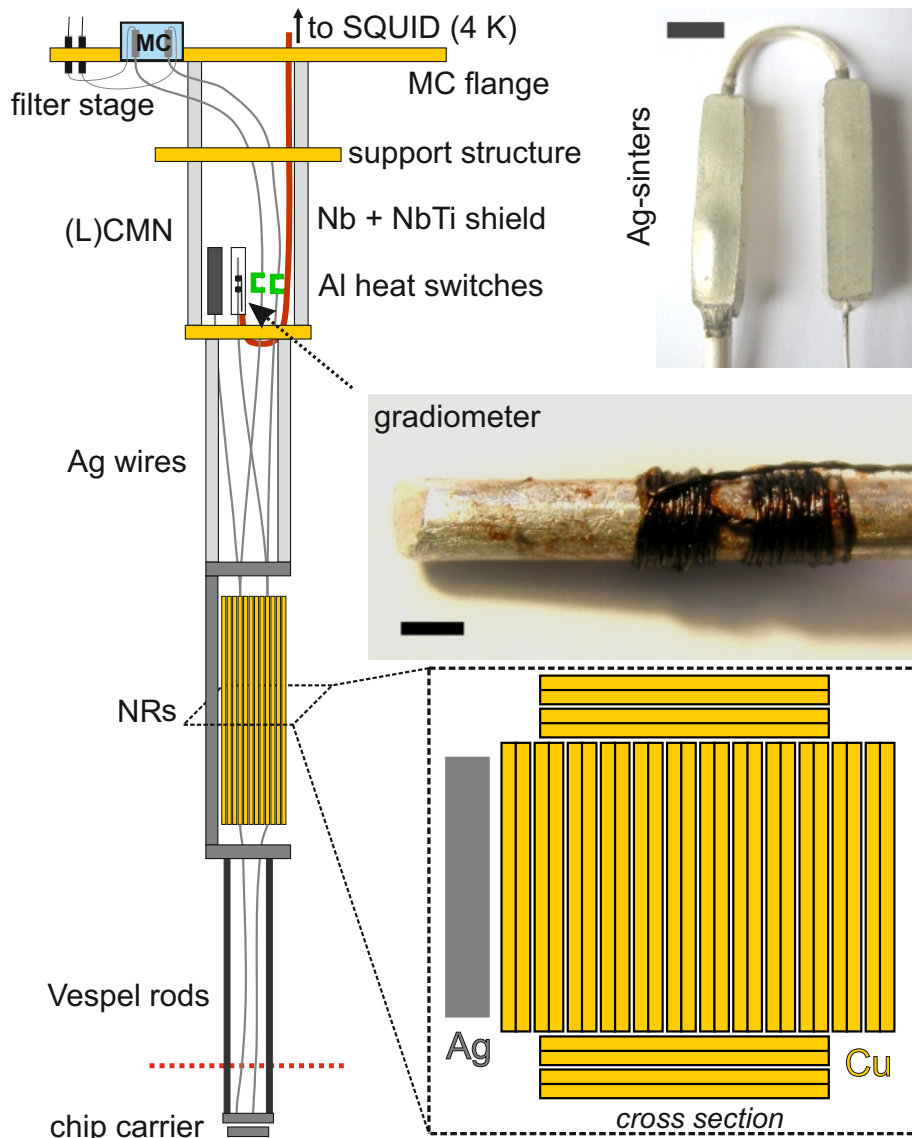


Figure 2.1: Schematic of the nuclear demagnetization stage. The measurement leads are thermalized with Ag powder sinters (*top right picture*, scale bar: 5 mm) in the mixing chamber (MC, blue) and pass through C-shaped Al heat switches (green) to the Cu plates. The gradiometer of the noise thermometer as well as the (L)CMN thermometers are positioned in a region of cancelled magnetic field between the MC and the NR stage. The gradiometer is double-shielded by a Nb tube and an outer NbTi tube (red). *Middle right inset:* photograph of the gradiometer pick-up coil made from insulated Nb wire with $100\ \mu\text{m}$ diameter. The 2×20 turns are wound non-inductively on a high-purity silver wire which is spot-welded to a NR. Scale bar: 2 mm. *Lower inset:* schematic cross section through the network of 16 parallel NRs. Each NR is 2 mol of Cu (99.99% Cu, low- H_2 content [48], $\text{RRR} \sim 500$) and consists of two half-plates, spot-welded together at the top and bottom. Each half-plate is of dimension $3.4 \times 0.17 \times 12\ \text{cm}^3$.

Figure 2.1 shows a schematic of the nuclear stage. Starting from the top, the measure-

ment leads are filtered by lossy thermocoax [49] from room temperature (RT) to the MC flange of the dilution refrigerator. Additional filtering is achieved by home-built Ag-epoxy filters [34] and double-stage RC filters bolted to the MC flange. Next, each of the 16 leads is thermalized inside the Cu MC using Ag powder sinters, as shown in the top right inset of Fig. 2.1, which are electrically insulated from the MC (ground) and each other. To allow the passage of the leads through the MC we designed super-fluid leak-tight feedthroughs on the bottom of the MC. The leads exit the MC as annealed Ag-wires, then pass through the Al heat switches with fused joints [50] and finally they are spot-welded to the Cu plate NRs. At the bottom of each NR, another annealed Ag wire continues to the chip carrier, providing a platform for nanostructured samples on an easily exchangeable chip carrier, see Fig. 2.1. Therefore, each lead provides a thermally highly conductive path from the sample to the NR, electrically insulated from all other wires and ground. The chip socket below the red dashed line in Fig. 2.1 was not mounted during the measurements in the main text, but can easily be added without significant influence on refrigerator performance. For additional details about the measurement setup see the supplementary materials paragraph

Magnetic fields up to 9T can be separately and independently applied to the AND stage and the sample. The C-shaped Al pieces are used to implement the concept of heat switches allowing to choose between excellent or very poor thermal conductivity, while always keeping the sample electrically connected. In the superconducting state Al is a thermal insulator while in its normal state, when the superconductivity is broken by a small magnetic field (≥ 10 mT), it is an excellent thermal conductor. All the thermometers used in the experiment are susceptible to magnetic fields; therefore they are positioned together with the Al heat switches in a region of canceled magnetic field between the MC and the NRs and are double shielded by Nb and NbTi tubes. The three thermometers in use are a Cerium Magnesium Nitrate (CMN) thermometer, a Lanthanum diluted CMN (LCMN) thermometer and the Johnson noise thermometer. Each thermometer is connected to its own NR through a massive Ag wire of 25 cm

length.

Although there are no mechanically moving parts in state-of-the-art pulse tubes, vibrations caused by high-pressure gas oscillations and the compressor package are transmitted to the refrigerator. Despite significant progress in recent years, cryogen-free systems tend to have drastically increased vibration levels compared to standard systems (i.e. dewars with cryo liquids). To account for these challenges, special care was taken on damping all connections to the fridge and decoupling the PT cold head [51] mechanically while maintaining a good thermal link. This was done with soft but massive Cu braids linking the cold head stages to the refrigerator and spring-loading the room temperature mount of the cold head. The PT motor was mounted remotely and was shielded, and the connection hose to the cold head was rigidly held in place. Altogether, this reduces the vertical displacement from $\sim 6 \mu\text{m}$ to below $0.3 \mu\text{m}$, as measured with an accelerometer. The circulation pumps were isolated with a massive concrete block fixing the pumping lines, and the entire system was mounted on a vibration isolation table. Further, the presented setup was improved from a previous wet system [31, 43] to particularly meet the demands of a cryogen-free system [51]. We introduced a rigid support structure and an adapted geometry of the NRs. Compared to the wet system version [32], we decreased the cross section relevant for eddy current heating and simultaneously doubled the amount of Cu per plate. Further, the surface area of the Ag-sinters was tripled to now 9 m^2 per lead and the diameter of the Ag wires is doubled, since these thermal resistances have been identified as a bottle neck during precooling [31].

2.3 Noise Thermometry

Measuring temperatures in the μK regime is a challenging task, since many thermometers suffer from self-heating and are very susceptible to heat leaks, often leading to a saturation of the thermometer. Here we use a specific type of noise thermometer, the magnetic field fluctuation thermometer (MFFT), based on an inductive read-out [44–

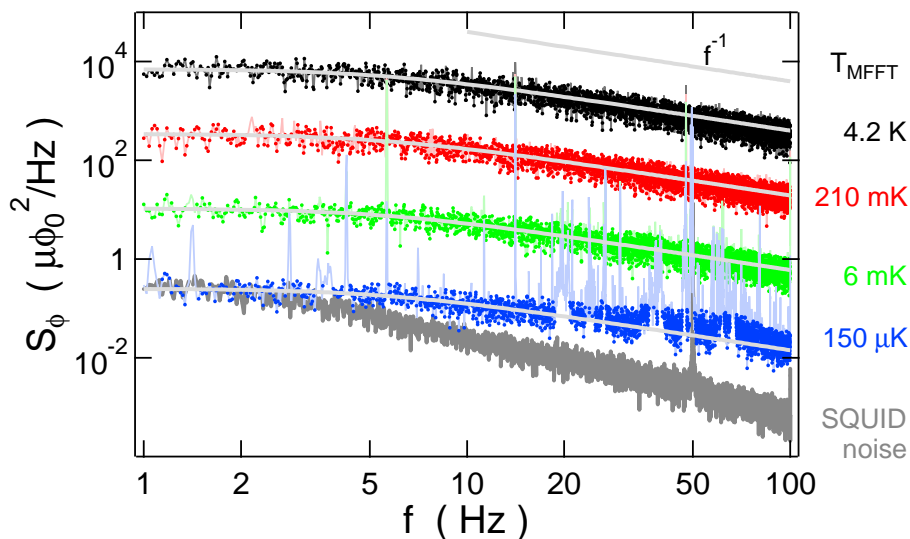


Figure 2.2: Power spectral density $S_\phi(0, T_{\text{MFFT}})$ of the magnetic flux noise, in units of the flux quantum ϕ_0 , at various NR temperatures. The light gray solid curves are fits using Eq. (2.2) which are converted to T_{MFFT} as described in the text using the reference spectrum at $T_{\text{ref}} = 4.2\text{K}$. The noise peaks become more visible at lower temperatures where the thermal noise becomes smaller. The SQUID noise shown here in grey is from a similar SQUID with the inputs shorted, not from the SQUID used to measure the MFFT.

46, 52] using a SQUID amplifier¹, which is designed to reduce internal and external heat leaks. In fact, we reduce the external heat leaks onto the thermometer by mechanical and electrical decoupling of shield and thermal noise source, see supplementary material paragraph. In addition, thanks to the inductive read-out, the thermal noise is detected without any bias applied, thus reducing self-heating of the thermometer. Our improvements allow us to measure temperatures down to $150\ \mu\text{K}$, whereas the lowest measurable temperature is roughly $100\ \mu\text{K}$ given by the SQUID noise floor. Figure 2.2 shows the spectra for various temperatures. Note that for the lowest temperature (blue) the spectrum is just above the SQUID noise spectrum (grey).

The temperature of electrons in a metal is related to their thermal (Brownian) motion, which generates current noise given by the Johnson-Nyquist formula [53, 54]:

$$S_I = \frac{4k_B T}{R}. \quad (2.1)$$

¹1-stage Current Sensor C4L1W DC-SQUID, Magnicon GmbH, Hamburg, Germany.

Here, S_I is the power spectral density of the current noise, k_B is the Boltzmann constant, T is the temperature of the electrons in the conductor and R is the resistance of the metal. The read-out of the thermal noise is done by a gradiometer, consisting of two counter-wound superconducting pick-up coils (detector) wrapped tightly around a Ag wire (thermal noise source) of radius r . The working principle is the following: thermal currents are transformed, by self-inductance, into magnetic flux fluctuations, detected by the pick-up coil. In the low frequency range, the power spectral density of the magnetic flux noise [52, 55] can be written as $S_\phi(0, T_{\text{MFFT}}) = 4k_B T_{\text{MFFT}} \sigma G \mu_0^2 r^3 / 2\pi$, where μ_0 is the vacuum permeability, T_{MFFT} is the electronic temperature measured with the MFFT, G is a geometric factor [52] and σ is the electrical conductivity at low temperatures, which is assumed temperature independent in the mK range. The electrical conductivity is defined as $\sigma = \sigma_{\text{RT}} * \text{RRR}$, with RRR being the residual resistivity ratio and σ_{RT} the room temperature conductivity. Note that $S_\phi(0, T_{\text{MFFT}})$ depends linearly on temperature T_{MFFT} , since σ is constant at low frequency where the skin effect is negligible. Figure 2.2 shows that all the spectra have a low-frequency plateau.

The Skin effect forces high frequency current fluctuating to the metal surface. As a consequence the conductivity of the Ag wire becomes frequency dependent, resulting in a low-pass like shape of $S_\phi(f, T_{\text{MFFT}})$. Such a frequency dependence is described by the following equation:

$$S_\phi(f, T_{\text{MFFT}}) = \frac{S_\phi(0, T_{\text{MFFT}})}{\sqrt{1 + \left(\frac{f}{f_c}\right)^2}}, \quad (2.2)$$

where the cut-off frequency is given by $f_c = 4.5/(\pi\mu_0\sigma r^2)$ [52]. As expected in Fig. 2.2 the amplitudes of the spectra decrease as $1/f$ at high frequencies.

In order to measure² the power spectral density, we need to acquire 10 real-time noise

²The DC-SQUID is operated in a flux-locked loop mode with XXF-1 electronics, including a second order Bessel-type low-pass filter ($f_{3\text{dB}} = 10$ kHz). After a room temperature voltage preamplifier with another low-pass filter ($f_{3\text{dB}} = 1$ kHz), the signal is acquired with a digital-to-analog converter.

traces with 50 s duration each, which are averaged after Fourier transformation. Noise peaks appear mostly at frequencies corresponding to higher harmonics of the rotation frequency of the PT motor (1.4 Hz), see light blue spectrum in Fig. 2.2. The peaks become more evident at low temperatures due to the lower thermal noise background. To eliminate these peaks we fit every spectrum first with a polynomial of 10th order and eliminate any data that exceeds the polynomial by more than an empirically determined threshold factor.

The MFFT is used as a secondary thermometer calibrated against the MC thermometer at 4.2 K. From the fit of Eq. (2) to the reference spectrum at 4.2 K, we extract a value of $f_c \sim 5$ Hz independent of temperature and corresponding to a RRR of about 2000, which matches typical RRRs determined in independent transport measurements. Thus, we fix $f_c = 5$ Hz and extract T_{MFFT} as the only fit parameter from the fit to Eq. (2.2).

To achieve optimal performance of the MFFT, we addressed and solved the following technical issues. First, to avoid effects from homogeneous magnetic fields, the pick-up coil is non-inductively wound around the Ag wire. Second, the gradiometer shown in Fig. 2.1 is connected by a long section of twisted Nb wires to the SQUID, which is anchored to the quasi-4 K-flange of the refrigerator. The twisted Nb wires are double-shielded with a Nb and NbTi tube, both thermalized at the mixing chamber plate, cold plate and still plate. Finally, we mounted the SQUID at 4 K to avoid low-frequency excess flux noise [56], which can arise at sub-K temperatures.

2.4 Nuclear Refrigerator Performance

The nuclear refrigerator technique is based on a single shot cycle consisting of the following steps: magnetization in an initial field $B_i=9$ T, precooling down to $T_i=10$ mK (three days), and demagnetization down to a final field B_f . Finally, low temperatures can be explored over a period of time while the system continuously warms up due to a small parasitic heat leak (\dot{Q}) absorbed by the NRs. During the AND process the nuclear

temperature of the Cu plate is lowered from the initial temperature T_i down to the final temperature T_f . During magnetization and precooling, the Al heat switches are set to conduct heat excellently (normal state) to cool the NRs via the MC. While demagnetizing and warming up, the heat switches are superconducting to prevent heat flowing from the MC into the NRs. In this refrigeration technique, the nuclear spin degree of freedom has by far the largest heat capacity, absorbing the heat leaks coming into the NRs. This can lead to non-equilibrium configurations where other degrees of freedom (e.g. electrons, phonons) can be at different temperatures than the nuclear spins, due to the finite thermal conductivity between them.

We need to characterize the heat leak of the system, which then defines the efficiency $\xi = (T_i/T_f)/(B_i/B_f)$ of the AND process. An efficiency of 100% indicates a fully adiabatic and reversible process while ξ less than 100% signifies the presence of heat leaks, which spoil the adiabaticity of the AND process. One distinguishes two types of heat leaks: a static heat leak (\dot{Q}) appearing already at fixed magnetic field and attributed mainly to heat release, radiation and vibrations. Beyond that, an additional dynamic heat leak (\dot{Q}_{dyn}) appears when sweeping the magnetic field.

To determine the static heat leak onto a NR, we read a sensor temperature T_s as a function of time during the warm up, see Fig. 3.1, displaying T_s^{-1} . Our sensor cannot operate directly on the NR due to the magnetic fields present, and thus is placed at some distance and is thermally well connected to the NR through a high-conductivity Ag wire. Over time, the temperature is continuously increasing until it saturates at rather high temperature ~ 50 mK, far exceeding the MC temperature $T_{\text{MC}} \sim 7$ mK. At this point, the heat leaking from the NR through the Al heat switches into the MC balances the static heat leak, keeping the Cu stage at a constant temperature. One can model the warm up behavior of the NRs [1, 27] by assuming a constant static heat leak \dot{Q} flowing entirely into the Cu nuclear spins:

$$T_{\text{e,Cu}}^{-1}(t) = T_{\text{ex}}^{-1} - t \left(\frac{\lambda_n B_f^2}{\mu_0 \dot{Q}} + \kappa \right)^{-1}, \quad (2.3)$$

where $T_{e,Cu}$ is the electronic temperature of the Cu plate, T_{ex} is the extrapolated electronic temperature of the Cu plate at the beginning of the warm up, μ_0 is the vacuum permeability, λ_n is the molar nuclear Curie constant of Cu and κ is the Korringa constant [27] for Cu. The Korringa constant quantifies thermal coupling and thus the temperature gradient between the electrons and the nuclei. As Eq. (2.3) shows, $T_{e,Cu}^{-1}$ is an affine function of time. In the intermediate temperature regime, but away from saturation, we fit Eq. (2.3) to the data, shown as dashed lines in Fig. 3.1(a). The fits are in very good agreement with the data for intermediate temperatures, which indicates that the heat leak is constant over a long period of time.

From the fit we extract \dot{Q} and T_{ex} . The black crosses in the inset of Fig. 3.1(b) show the measured \dot{Q} for ANDs at various final fields. As seen, \dot{Q} is roughly 1 nW/mol and independent of B_f below 1 T. This is striking since it indicates negligible eddy current heating. During a warm up, the magnetic field is held constant but eddy current heating could still arise due to vibrations in an inhomogeneous magnetic field: $\dot{Q} \propto (dB/dt)^2 = [(dB/d\mathbf{r})(d\mathbf{r}/dt)]^2$.

As shown in Fig. 3.1(a), the temperature sensor shows a saturation in the low temperature regime and lies below the theory curve of inverse temperature. Such an elevated sensor temperature T_s can be caused by heat release, e.g. at the thermometer itself. The temperature gradient between the sensor and the NR can be taken into account using a heat flow equation, that fits the sensor temperature of the MFFT in the whole dynamic range. The total static heat leak can be decomposed into a sensor heat leak \dot{Q}_s and a remaining heat leak directly acting onto the NRs. The temperature gradient due to the heat leak \dot{Q}_s can be written as :

$$T_s^2(t) - T_{e,Cu}^2(t) = \frac{2}{\kappa_0} \dot{Q}_s. \quad (2.4)$$

The difference between the square of the two temperatures comes from the integration of the thermal conductivity of the metallic link between the sensor and the NR, which

is linear in temperature. The coefficient $\kappa_0 = \pi^2 k_B^2 / 3e^2 R_{\text{tot}}$, where e is the electron charge, depends on the total resistance $R_{\text{tot}} \sim 1 \mu\Omega$ comprised in similar parts from the spot-welded junction between the Ag wire and the Cu plate and the resistance of the Ag wire. Note that the low temperature resistivity is reduced by a RRR ~ 2000 , achieved by annealing the high purity Ag wire. By plugging Eq. (2.3) into Eq. (2.4), we obtain T_s^{-1} as a function of the time with \dot{Q}_s as an additional fit parameter. The solid blue curves in Fig. 3.1(a) show the best fit, exhibiting excellent agreement down to the lowest temperatures. The sensor heat leak \dot{Q}_s is between 5 and 20% of \dot{Q} , indicating a rather small heat leak emanating from the MFFT.

Performing a complete AND experiment to extract \dot{Q} for different B -fields is very time-consuming. In order to procure \dot{Q} faster, we introduce an abbreviated precool and warm up (PW) cycle: The Cu stage is precooled at fixed magnetic field and subsequently warms up due to the heat leak \dot{Q} , after being thermally isolated from the MC with the heat switch. Figure 3.1(b) shows the warm-up of a PW cycle at a B -field of 0.5 T for all the thermometers in use. For all three sensors, the inverse of the temperature decreases linearly in time and eventually saturates at high temperature. Note that each of the three thermometers have their own saturation temperature (high T) and warm up time, indicating different heat leaks. By using Eq. (2.3) (dashed line in Fig. 3.1(b)) we extract a \dot{Q} for the MFFT of around 1 nW/mol and find higher values of 2 nW/mol for the CMN and 4.8 nW/mol for the LCMN. The heat leaks extracted with PWs for different B -fields are consistent with the ones from warm ups after AND, see inset of Fig. 3.1(b). Note that for the MFFT a minute amount of GE Varnish is used to fix the superconducting pick-up coil to the silver wire while for the packaging of the (L)CMN, a considerable amount of epoxy is used, which is a well-known source of heat release.

Next, we compare the electronic temperature of the Cu plates $T_{e,\text{Cu}}$ as extrapolated from the warm up curves after AND (T_{ex}) with the measured electronic temperature T_{MFFT} , finding excellent agreement, as seen in Fig. 2.4, blue squares. Even though the thermometers used for the extrapolation (CMN and LCMN) become fully saturated

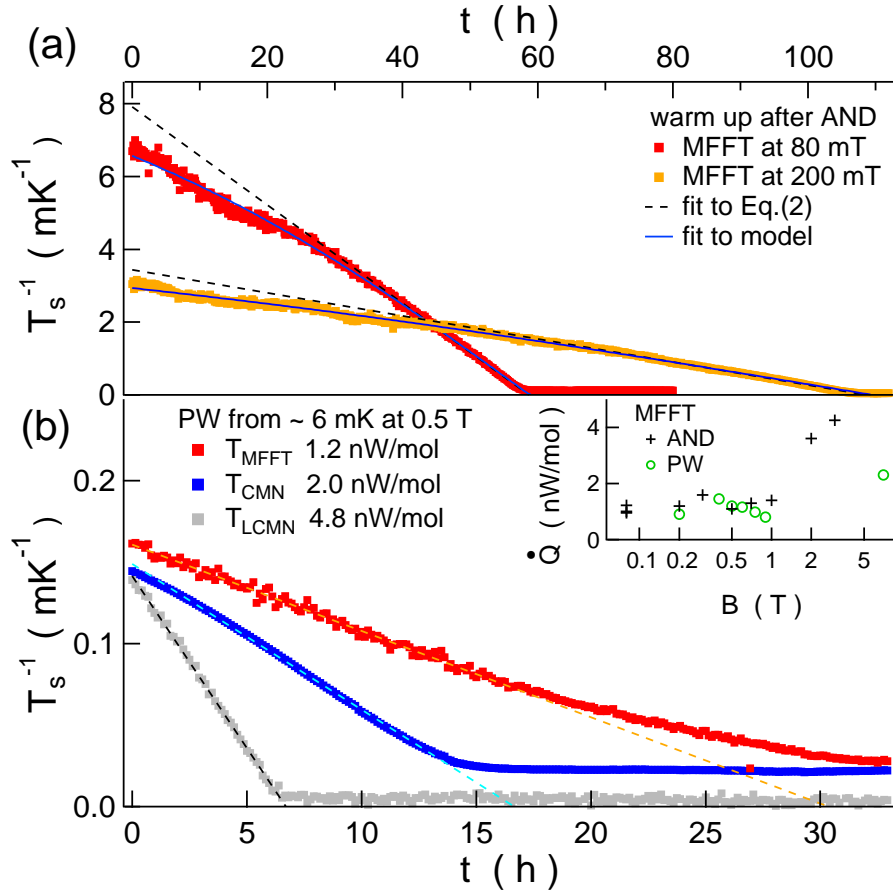


Figure 2.3: Warm-up curves: (a) Inverse of T_s measured with the MFFT versus time during the warm up at 80 mT (red squares) and 200 mT (orange squares) after AND. The linear fits (black dashed lines) reveal extrapolated electron temperatures $T_{\text{ex}} = 126/280 \mu\text{K}$ at the beginning of the warm up and heat leaks of $\dot{Q} = 0.9/1.16 \text{ nW/mol}$ for 80 mT and 200 mT, respectively. The solid blue curves are the fits to the heat flow model (see main text) with $\dot{Q}_s = 6\%$ at 80 mT and 18% at 200 mT of the total static heat leak. (b) Precool and warm up (PW) measurements: T_s^{-1} during warm up, from MFFT, CMN and LCMN thermometers versus the time after opening the heat switches at $B = 0.5 \text{ T}$, resulting in $\dot{Q} = 1.2/2.0/4.8 \text{ nW/mol}$, respectively. Inset: static heat leak \dot{Q} to the nuclear stage per mol of Cu, measured with the MFFT at various B -fields, extracted using Eq. (2.3) after AND (black crosses) and after PW (green circles).

at rather high temperatures, here around 2.5 mK, the extrapolation method – as also relied on in our previous works [31, 32, 43] – is seen here to work rather well down to the lowest temperatures measured. As shown in Fig. 2.4 below 400 μK , T_{MFFT} starts to be slightly higher than $T_{\text{e,Cu}}$, reaching a maximum deviation of 20 % for the lowest temperature. At 150 μK the MFFT is mainly limited by the SQUID noise level and hence slightly higher than the lowest extracted temperature $T_{\text{ex}}=120 \mu\text{K}$. In the high temperature regime, the MFFT is tested against a calibrated RuO_2 thermometer sitting on the MC flange, showing excellent agreement of the temperature reading of the two thermometers, see red squares in Fig. 2.4.

To complete the characterization of the AND system, we now turn to the efficiency of the process. As shown in the inset of Fig. 2.4 the efficiency decreases monotonically from almost 100 % at high final magnetic field down to 70 % for the lowest final field. The reduction of the efficiency for lower magnetic fields is a result of the smaller heat capacity of the Cu nuclei, which is proportional to B_f^2 . We simulated the efficiency of the AND process assuming \dot{Q}_{dyn} depending linearly or quadratically on B or \dot{B} as one would expect for \dot{Q}_{dyn} arising from vibration or eddy current heating, but in these cases the simulations completely missed the experimental points. In contrast, assuming a fixed \dot{Q}_{dyn} of 29 nW/mol, independent of B or \dot{B} , reproduces the data well (green dashed curve in inset of Fig. 2.4). Thus, the simulation suggests that \dot{Q}_{dyn} is constant in time and independent of the ramp-rate of the B -field, which gives the opportunity to increase the efficiency by reducing the duration of the demagnetization process. This hypothesis was successfully tested in the experiments by doubling the ramp speed of the AND, as shown by the blue crosses in the inset, where ξ increases significantly for the faster rate – albeit the simulation predicts slightly different efficiencies than those measured.

To estimate the dynamic heat leak, we first open the switches, then we ramp the magnetic field from zero to a finite B -field and back to avoid any nuclear contribution to the heat capacity. We measured the temperature of the Cu plates and by integrating

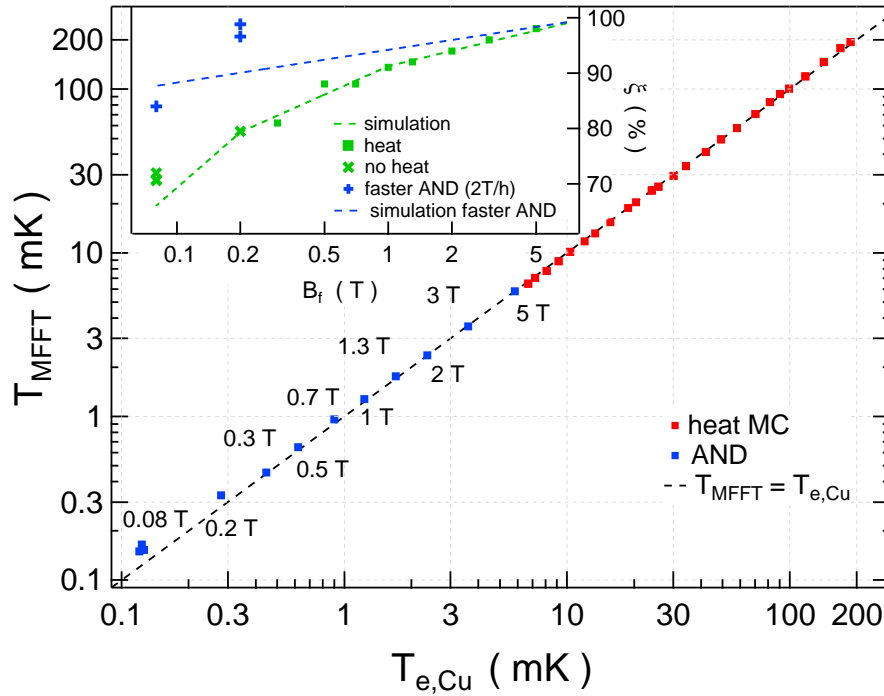


Figure 2.4: Temperature measured by the noise thermometer T_{MFFT} versus temperature of the nuclear stage $T_{\text{e,Cu}}$. Above 7 mK, $T_{\text{e,Cu}}$ is measured with a calibrated RuO_2 thermometer sitting on the MC (red squares). In this temperature range the MC and the Cu stage are well thermally coupled. For temperatures below 7 mK, $T_{\text{e,Cu}}$ is extracted from warm ups after AND (blue squares) (see text and Fig. 3.1(a)). The black dotted line represents $T_{\text{MFFT}} = T_{\text{e,Cu}}$. *Inset:* the efficiency ξ as function of the final magnetic fields B_f . The dashed curves show simulations of the AND process, carried out at two different ramp speeds. The markers show the efficiency extracted from different AND runs as labeled.

the electron heat capacity we obtain the energy stored in the system. In addition, we estimate the heat leaking through the superconducting Al heat switches due to phonon-dislocation scattering processes [1, 57]. This estimation yields \dot{Q}_{dyn} of 22 nW/mol for a ramp-rate of 1 T/h, which is comparable to the value used in the simulation. However, the \dot{Q}_{dyn} estimated with this protocol is dependent on the ramp-rate, which is in disagreement with the simulation. Our simple model needs further work to fully understand the origin of \dot{Q}_{dyn} and its dependence on the sweep rate.

2.5 Conclusions

In summary, we have implemented a parallel network of 16 electrically separated NRs on a cryogen-free platform. These 16 plates are part of the measurement leads and can be straightforwardly used to cool nanostructured samples. The nuclear stage is equipped with a magnetic field fluctuation thermometer, showing excellent agreement with the NR temperature $T_{e,\text{Cu}}$ down to 400 μK . After AND to $B_f = 0.08$ T, the lowest temperature reading is limited to 150 μK while the extrapolated electron temperatures is 120 μK , indicating good agreement between the model and measurements. The heat leak measured on the NRs is around 1 nW/mol and allows the AND stage to stay below 1 mK for roughly 50 hours, see supplementary material paragraph. Higher B_f allow for even longer hold times, while still supplying reasonably low temperatures. In addition, we characterized the dynamic heat leak, which appears to be constant in time and independent of the sweep rate of the magnetic field, making possible significantly increased efficiency at faster magnetic field sweep rates.

2.6 acknowledgments

We would like to thank H. J. Barthelmeß, R. Blaauwgeers, G. Pickett, M. Steinacher and P. Vorselman for useful input and discussions. The work shop team of S. Martin is acknowledged for technical support. This work was supported by the Swiss NSF,

NCCR QSIT, the Swiss Nanoscience Institute, the European Microkelvin Platform, an ERC starting grant (DMZ), and EU-FP7 MICROKELVIN and SOLID.

2.7 Supplementary Material

The supplementary material provides a more detailed description of the setup, additional information about the precooling and warm-up stages, a discussion of the socket, as well as details of the gradiometer design.

2.7.1 Setup

Figure 2.5 shows a scheme of the dilution refrigerator from room temperature down to the chip carrier. The measurement leads from the RT flange down to the MC are made by 1.5 m long lossy thermocoaxes, providing an attenuation of 100 dB for frequencies above 3 GHz. Then the leads are connected to microwave filters [34], which provide an attenuation of 100 dB above 200 MHz and thermalization for the electrons. In addition, we have a second filter stage that consists of two-pole resistor-capacitor filters ($2 \times [2 \text{ k}\Omega / 680 \text{ pF}]$). In order to further improve the thermalization of the measurement leads we use Ag-sinters, where each one of them has dimensions of $[4 \times 4 \times 20] \text{ mm}^3$ and a surface area of 4.5 m^2 measured with Brunauer-Emmett-Teller (BET) surface area analysis [58]. Doubling the number of sinters per lead compared to the previous setup [43] allows us to reach a lower precooling temperature in less time. As discussed in the main text we further doubled the diameter of the annealed high-purity 5N (99.999%) Ag wire ($\varnothing = 2.54 \text{ mm}$) coming out of the MC, to enhance the cooling. Each Ag wire is spot-welded to a Cu plate, resulting in the parallel network of 16 nuclear refrigerators. In addition, we doubled the amount of Cu per plate by spot-welding 2 half plates together. Each half plate has dimensions of $[34 \times 1.7 \times 120] \text{ mm}^3$, corresponding to 1 mol. In order to shield the 16 NRs, we use radiation shields which are attached to the still flange (around 650 mK) and mixing chamber flange (below 7 mK). As indicated below the dashed red line in Fig. 2.5, we design a sample holder

with 15 commercial pins for transport experiments. The sample holder is made of sapphire, which is a low heat release material, has a hole in the center to allow an annealed Ag wire to pass through and cool the metallic plane of the plug-in sapphire chip carrier. Using plug-in pins is practical to exchange samples, but the plug-in mechanism might cause strain, which is a possible source of heat release. The chip carrier is enclosed in a Faraday cage that functions as sample shield. The sample holder and the chip carrier were not installed at the time of the measurements reported in the main text and will be only considered in the last paragraphs of the supplementary material.

2.7.2 High Performance System

Figure 2.6(a) shows the temperature recorded with the MFFT (red squares) and CMN (blue line) for a typical precooling at 9 T. The temperature of both sensors decreases from 38 mK down to 9.8 mK in 85 hours. However, in 30 hours we reach a T_s of 13 mK, which could have been already used to perform an AND. As shown in Fig. 2.6(a) the cooling in the first 15 hours is less efficient than the theory [1] predicts, where at later time the experimental data follows the theory (depicted as dashed line) more closely. In order to perform electronic transport experiments, it is important to evaluate the hold time (below 1 mK). Therefore, in Fig. 2.6(b) we plot again the warm up curve for two final fields of 80 mT and 200 mT, measured with the MFFT. We obtain hold times of 50 hours for 80 mT and 80 hours for 200 mT, owing to the low static heat leak.

In the main text we discuss the static heat leak measured with the MFFT for various B -fields (inset of Fig. 3(b)). In Fig. 2.7, we present the same measurements for the CMN and LCMN thermometers. The static heat leak \dot{Q} is B -field independent below 1 T for both sensors, as observed for the MFFT. In addition, the static heat leak for the LCMN ($\dot{Q}=3$ nW/mol) and the CMN ($\dot{Q}=2.2$ nW/mol) thermometer is higher compared to the MFFT, possibly because of an increased amount of heat release of the thermometers.

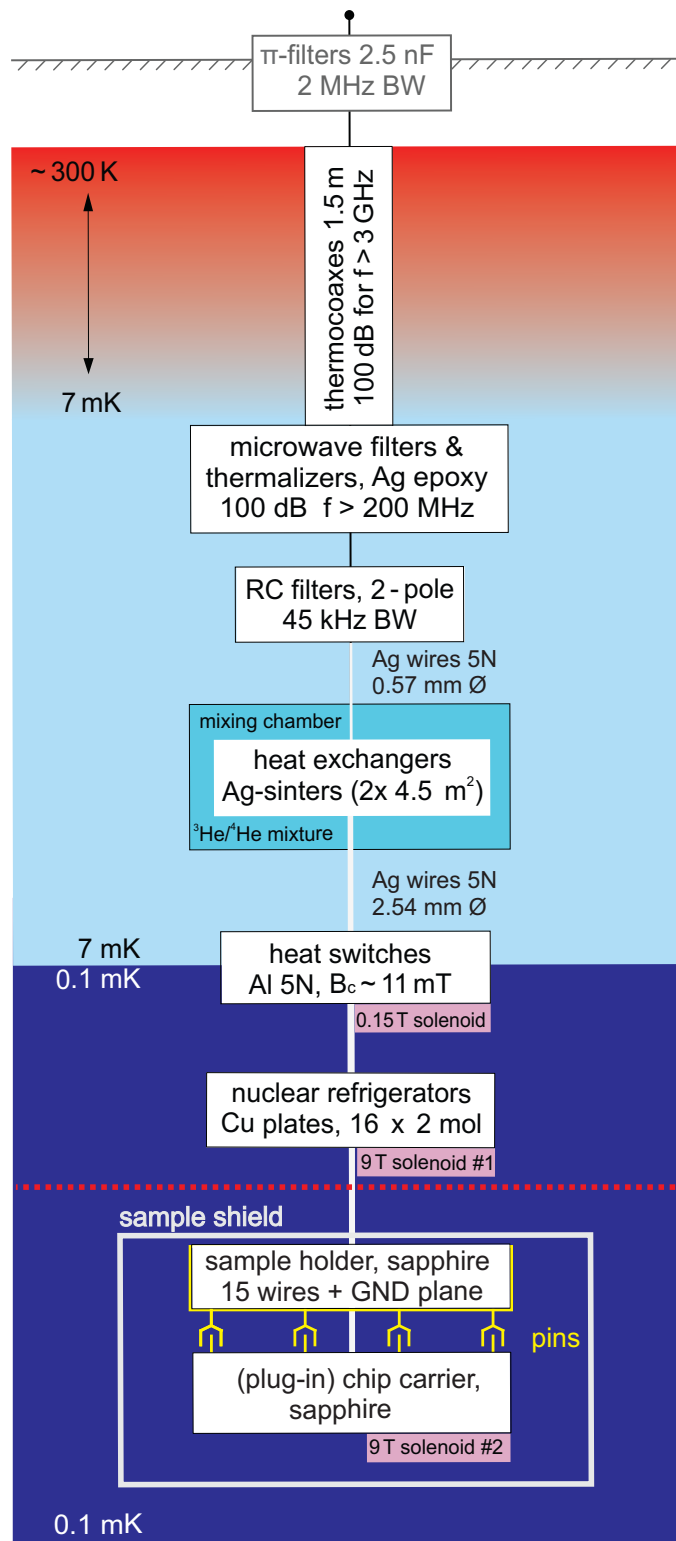


Figure 2.5: Scheme of the dilution unit together with NRs. Compared to Ref. [3] we doubled the number of sinters per lead, the diameter of the silver wires and the amount of Cu per plate. Below the dashed red line, the socket design for future transport experiments is illustrated. The abbreviations in the figure are bandwidth (BW), critical magnetic field (B_c) and the electrical ground (GND).

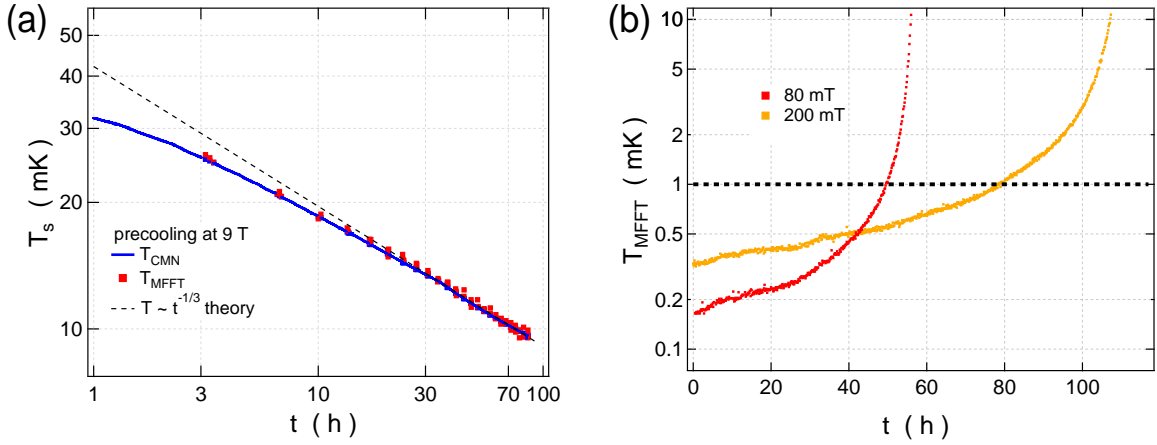


Figure 2.6: (a) shows the temperature of the CMN thermometer and MFFT as function of the time during the precooling at 9 T. The dashed line indicates the behavior of the precooling temperature predicted from the theory [1]. (b) T_{MFFT} versus time for warm ups at 80 mT and 200 mT. The dashed line points out the hold time below 1 mK, which is important for transport experiments.

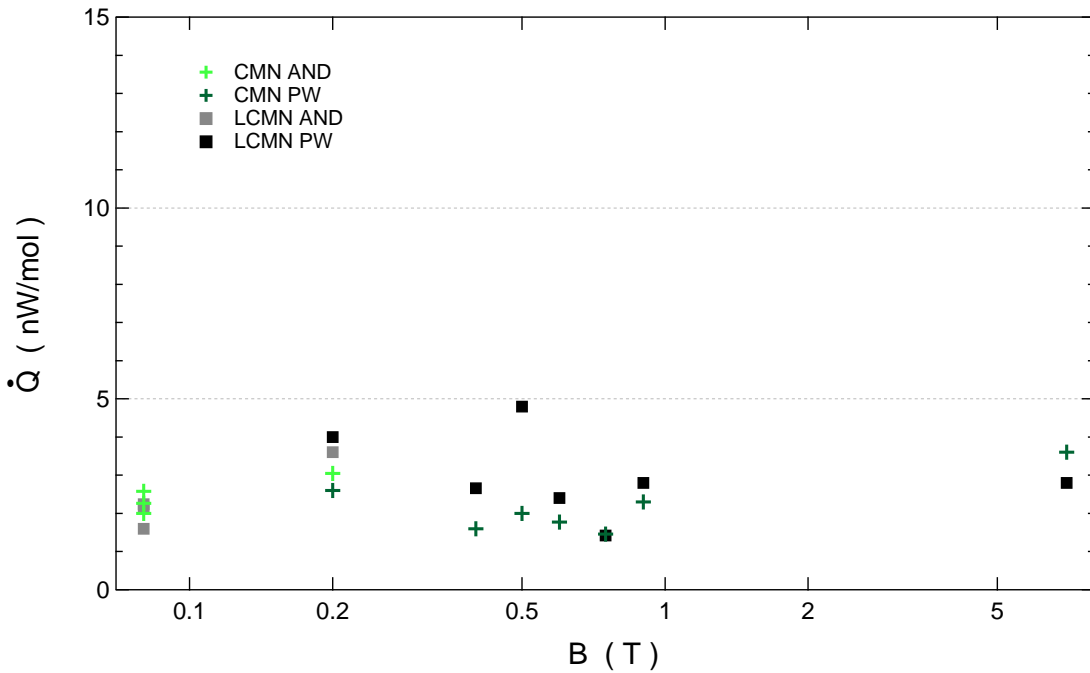


Figure 2.7: \dot{Q} at various B -fields measured with CMN and LCMN thermometers. The static heat leaks \dot{Q} are extracted with PW and AND methods introduced in the main text.

2.7.3 Warm up

As shown in Fig. 2.8, the inverse of T_s measured with CMN and LCMN thermometers is fitted with Eq. (2) of the main text. The extrapolated Cu electron temperature T_{ex} is close to the value obtained from the fit of the MFFT data in Fig. 3(a) of the main text. In Fig. 2.8(b) we show that the thermal model, presented in Eq. (3) of the main text, reproduces well the experimental data for the CMN and the LCMN thermometer. The CMN thermometer is still cooling in the first hours of the warm up in contrast to the LCMN thermometer, possibly due to the higher heat capacity of the CMN [59] compared to the LCMN. From the fit of Eq. (3), we extract a sensor heat leak \dot{Q}_s around 10-20% of \dot{Q} for both thermometers, which is an indication for a small heat leak coming from the thermometer, such values are similar to the \dot{Q}_s extracted for the MFFT. The higher heat leak of LCMN and CMN could arise from the screw press contact resistance of about $100 \mu\Omega$ between the thermometers and the connection to the NRs. For the MFFT we take into account only the resistance of the Ag-wire and the weld-joint between Ag wire and the Cu plate, which gives a total resistance of about $1 \mu\Omega$.

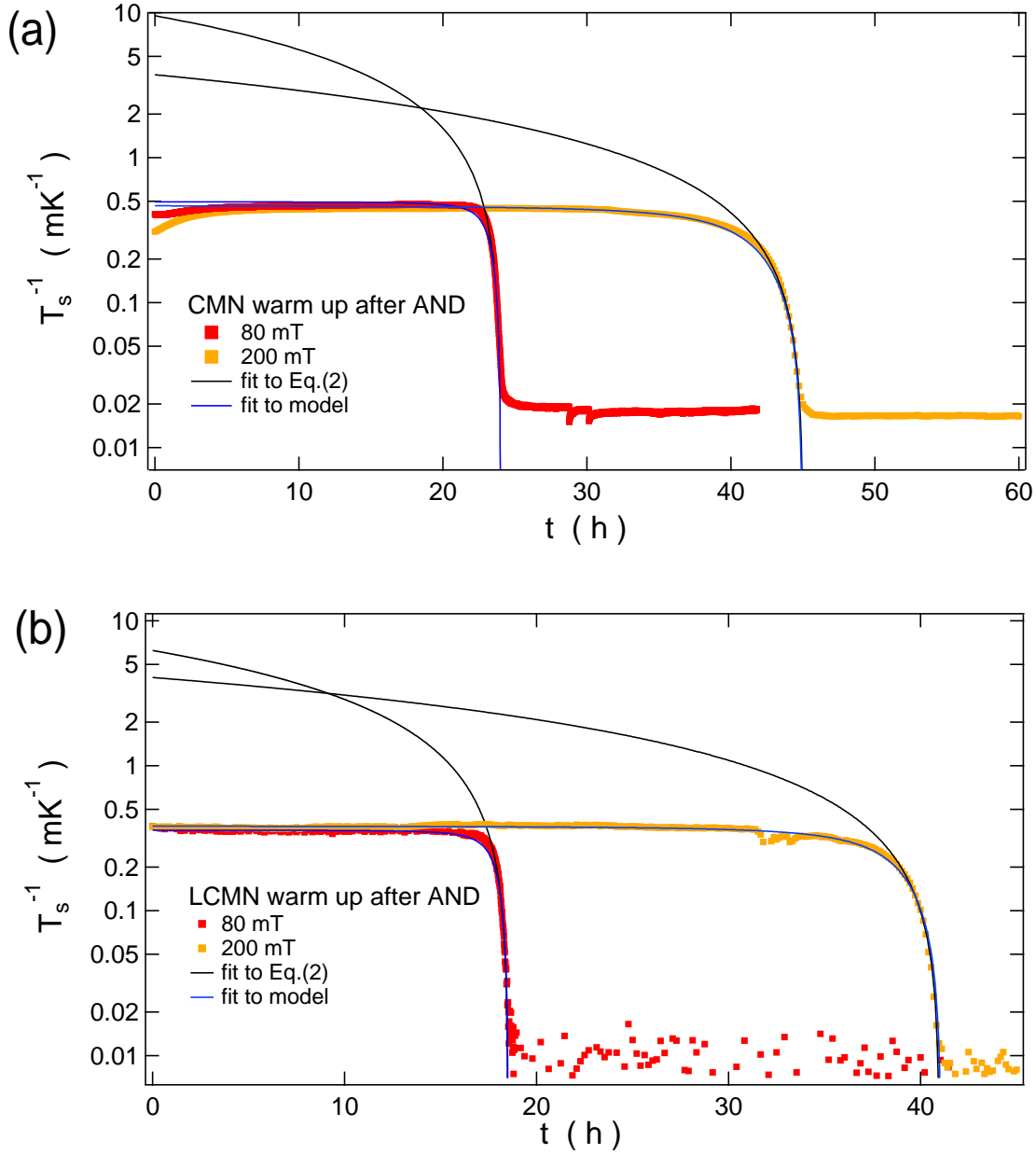


Figure 2.8: (a) inverse of T_s measured with the CMN thermometer versus time during the warm up at 80 mT and 200 mT. The warm up curves are plotted in semi-logarithmic scale, for this reason the lines appear as curves. The fit to Eq. (2) gives an extrapolated Cu electron temperature $T_{\text{ex}} = 105/268 \mu\text{K}$ and static heat leak $\dot{Q} = 2.6/3.1 \text{ nW/mol}$ for 80/200 mT, respectively. The solid blue line shows the heat flow model with $\dot{Q}_s = 9/10\%$ of \dot{Q} . (b) shows the same warm up curves for the LCMN thermometer. From the fit to Eq. (2) we extract $T_{\text{ex}} = 160/246 \mu\text{K}$ and $\dot{Q} = 2.1/3.6 \text{ nW/mol}$ for 80/200 mT, respectively. The heat flow equation reveals $\dot{Q}_s = 11/22\%$ of \dot{Q} for 80/200 mT, respectively.

2.7.4 Socket

So far we presented data only referring to NRs without any socket and carrier structure. The introduction of these additional parts might affect the performance of the NRs due to the heat load of the additional material introduced. Therefore we compared the static heat leak measured with MFFT for two different sockets. First, we used a Ag-epoxy socket with a geometry as discussed in the setup paragraph, but with an additional microwave-filter incorporated in the socket. Ag-epoxy is a conductive glue, which enhances the cooling of the chip through the substrate but, however, it is a material with heat release due to structural relaxation of low energy excitations [1]. In Figure 2.9, the heat leak for the Ag-epoxy socket (black triangles) is measured for various B -fields. We obtain an average \dot{Q} between 3 and 4 nW/mol, independent of the B -field. By comparing this data to the inset of Fig. 3(b), where no socket was installed, the heat release of the Ag-epoxy socket is a factor of 2 higher. In order to reduce the heat release we replace the Ag-epoxy by sapphire, that due to the crystalline structure is supposed to have low heat release. The measured heat leak is around 2 nW/mol and B independent below 1 T. The heat leak for sapphire socket is in general lower compared to Ag-epoxy socket but higher than with no socket.

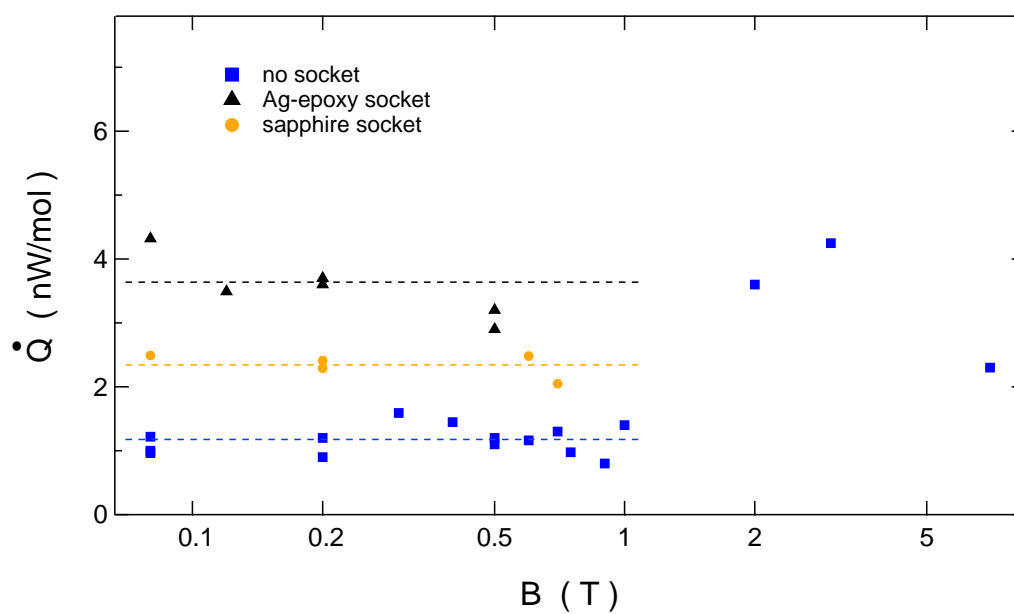


Figure 2.9: The static heat leak \dot{Q} measured with MFFT for various magnetic fields and for three different socket designs: no socket, Ag-epoxy socket and sapphire socket. The dashed lines are guides for the eyes

2.7.5 Gradiometer Design

Here, we discuss the improvements that we have done to the design of the noise thermometer. In the first design the thermometer was in direct contact with the superconducting shields, which could introduce additional heat leaks onto the thermometer. Therefore in the second design, we mounted the thermometer contact-less. We introduced a shield holder, which thermalizes the superconducting shields to the support structure without touching the thermometer. Figure 2.10 shows the data already presented in Fig. 4 of the main text for direct contact (black triangles) and contact-less mounting (blue squares and orange circles) of the thermometer. For the design with direct contact we observe a deviation of the measured temperature from the extrapolated temperature already below 2 mK, which leads to a saturation of T_{MFFT} at $740 \mu\text{K}$. In contrast, for the contact-less mounting of the thermometer T_{MFFT} agrees well with $T_{\text{e,Cu}}$ down to the lowest temperatures. Note that for the contact-less mounting of the thermometer we used two different socket configurations: sapphire socket and no socket. Despite their different heat leaks the temperature reading of the MFFT is the same. As result the contact-less mounting of the noise thermometer indeed reduces the heat leaks onto the noise source, leading to a lower temperature reading of the MFFT.

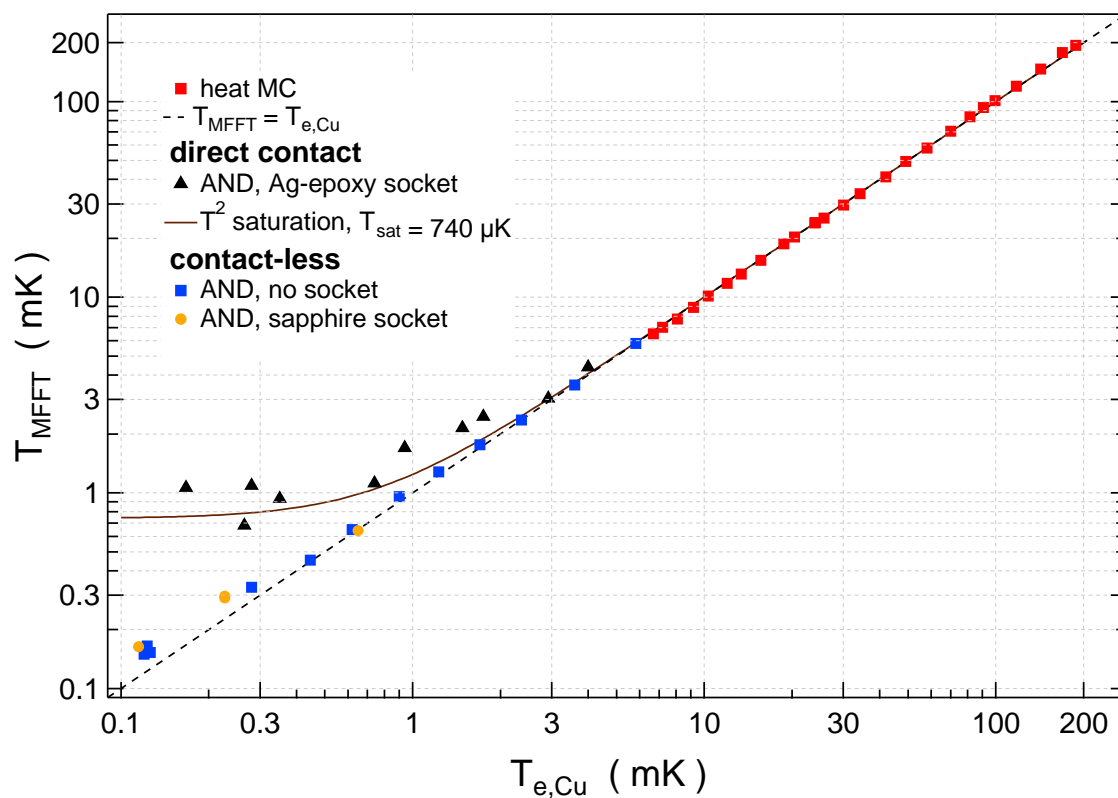


Figure 2.10: Temperature measured by MFFT versus the temperature of the nuclear stage T_{Cu} with T_{Cu} extracted as in Fig. 4 of the main text. We compare two different gradiometer designs: old design with Ag-epoxy socket and improved design realized for no socket and sapphire socket.

3 Thermal model AND process

In this section, we explain in detail the thermal model, which was introduced in the previous chapter. Starting from a thermodynamical approach for the nuclear magnetic cooling and proceeding with the analysis of the thermal interaction between the different degrees of freedom in the nuclear refrigerant, the basic equations of the thermal model are obtained. In the last part of this chapter, we describe the computational implementation of the thermal model, the improved efficiency of the process predicted by the model and the possible origin of the dynamic heat present during the demagnetization process.

3.1 Introduction

Adiabatic Nuclear Demagnetization (AND) is the most advanced cooling technique available so far to reach μK temperatures. We employed for the first time this technique in transport experiments, to cool electronic devices through the leads. We developed a model to describe the demagnetization of the Cu refrigerant and the model suggests ways to improve the process. In this Chapter, we describe the theoretical thermodynamic background of the AND technique and the thermal coupling among the degrees of freedom, which we need to take into account in our model. We introduce the equations employed in the model and the finite element algorithm used to solve the time evolution of the electron temperature and nuclei temperature. The model shows that a time *independent* heat leak is responsible for the loss of adiabaticity, indicating that we can reduce the effect of such a heat leak by reducing the duration of the process. The theoretical prediction finds support in the experiments, which demonstrate an increase of the efficiency from 67% to 82%.

3.2 Theory of the Adiabatic Nuclear Demagnetization

To understand the AND process, it is convenient to start with a thermodynamic approach to the phenomenon, which allows us to extract the equation utilized in the thermal model. We consider an ensemble of non-interacting nuclei, which have a nuclear spin \vec{I} and magnetic moment $\vec{\mu}_n$. An external magnetic field of magnitude B induces Zeeman splitting of the nuclear spin states, given by

$$E_Z = -mg_n\mu_n B, \quad (3.1)$$

where m is the the quantum number $[-I, -I+1, \dots, I-1, I]$, g_n is the nuclear g-factor and μ_n is the nuclear magneton. In the high temperatures limit where the thermal energy is dominating on the Zeeman splitting $E_Z \ll k_B T$, the molar nuclear spin entropy ($S_n(B, T)$), is expressed as

$$S_n(B, T) = R \ln(2I + 1) - \frac{\lambda_n B^2}{2\mu_0 T^2}, \quad (3.2)$$

where R is the ideal gas constant, λ_n is the molar nuclear Curie constant and μ_0 is the vacuum permeability. Using the Eq. (3.2) combined with the thermodynamic relation for the molar nuclear heat capacity C_n for a constant B ($C_n = T(\frac{\partial S_n}{\partial T})_B$), we obtain the Schoktty-law for nuclear heat capacity

$$C_n(B, T) = \frac{\lambda_n B^2}{\mu_0 T^2}. \quad (3.3)$$

Once we defined S_n and C_n , we have the elements to understand the AND process, which consists of the three steps namely magnetization, precooling and demagnetization. During magnetization, the magnetic field B is ramped up to an initial field B_i . As shown in Eq. (3.3) and Eq. (3.2), high magnetic field (typically $B=9$ T) and low temperatures (10-20 mK) are required to obtain a sizable polarization, see Fig.(3.1). In

order to precool the Cu refrigerant down to an initial temperature T_i , we need a good thermal link with the mixing chamber. Fig 3.1 shows a reduction of the molar entropy at fixed $B=B_i$ from point a to point b, leading to a decrease of the temperature. For the last step B is adiabatically reduced down to B_f , thus the molar nuclear entropy is conserved, $S_n(B_i, T_i) = S_n(B_f, T_f)$ and the temperature goes from T_i to the final temperature T_f , as indicated from b to c. The temperature during the demagnetization

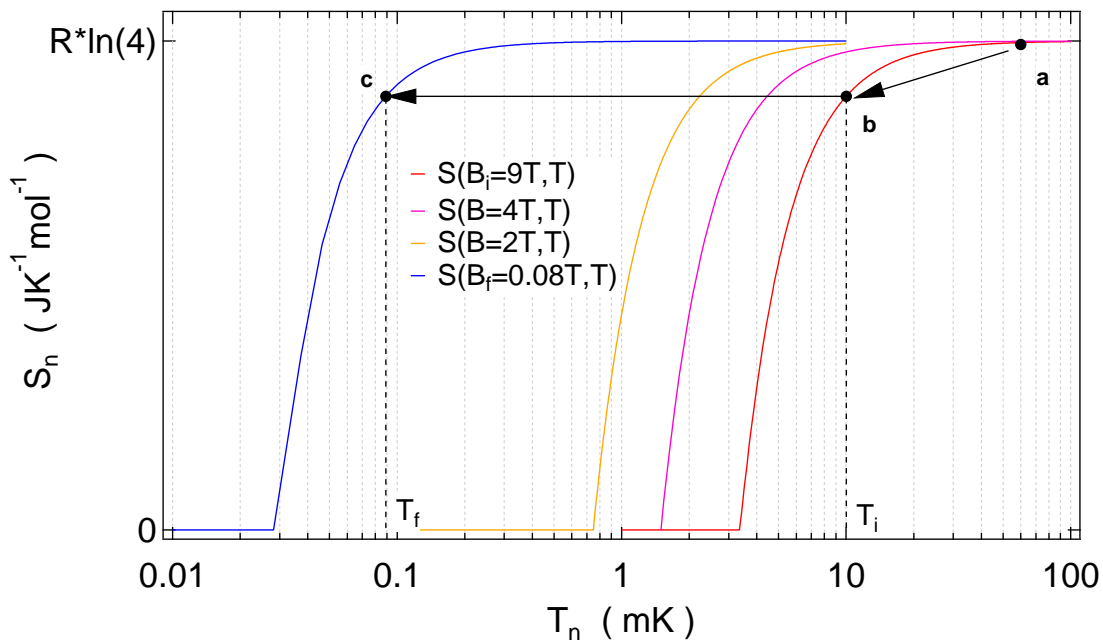


Figure 3.1: Molar nuclear spin entropy at fixed magnetic fields of $B_i = 9$ T (red curve) and $B_f = 80$ mT (blue curve) as a function of the nuclear temperature T_n . After ramping up the B -field up to 9 T, we wait and cool in the point a. During the precooling, we move along the red curve from point a to b, until we reach $T_i \sim 10$ mK. Note that for other magnetic fields, e.g. 4 T and 2 T, the molar entropy curves are shifted to the left compared to the one at 9 T, indicating lower nuclear temperatures are required to obtain the same value of S_n after precooling. During demagnetization, we move from b to c, indicated by the black arrow, the point c is located on the entropy curve at $B_f = 80$ mT with abscissa $T_f \sim 90$ μ K

process follows

$$T_f = B_f \frac{T_i}{B_i}. \quad (3.4)$$

Magnetization and precooling steps require a good thermal link between the nuclear refrigerant and the refrigerator while for the demagnetization we need to thermally insulate them to guarantee the adiabaticity of the process. Therefore, we use Al heat

switches to couple and decouple the nuclear refrigerant and the refrigerator, by switching between the normal state, i.e. good thermal conductor, and the superconducting state, i.e. thermal insulator.

In the experiments, it is difficult to obtain a complete adiabatic process due to parasitic heat leaks (\dot{Q}_{par}), which are always present in the nuclear refrigerant even when the Al heat switches are in the superconducting state. The heat leaks might be due to heat release, microwave radiation or electrical noise. These can increase the final temperature compared to the ideal process.

3.3 Degrees of Freedom in a Cu Plate

The adiabatic nuclear demagnetization cools the nuclei, which thermalize among each other within the spin-spin relaxation time τ_2 . However, our goal is to cool the electrons in the nuclear refrigerant, since those transfer the cooling power to the sample through the leads. To be able to write the heat relation between electron and nuclei, it is necessary to first consider the thermal interaction between different degrees of freedom, e.g. nuclei, electrons and phonon lattice, which coexist in the Cu refrigerant and heat exchange mechanism among each other. For perfect equilibrium configuration, all the degrees of freedom have the same temperature, while for non-equilibrium configuration the different degrees of freedom can have different temperatures with finite thermal coupling between them. As shown in Fig. (3.2) electrons and phonons exchange heat via electron-phonon interaction \dot{Q}_{e-ph} , in addition nuclei exchange efficiently heat with electrons via hyperfine interaction \dot{Q}_{en} . However, nuclei and phonons do not directly interact, as indicated in Fig. (3.2), thus the electrons function as mediator between phonons and nuclei as well as with the external environment \dot{Q}_{par} .

3.3.1 Electron-Phonon Coupling

As the first interaction between degrees of freedom, we consider the electron-phonon coupling [1], which reads

$$\dot{Q}_{e-ph} = V\Sigma(T_e^5 - T_{ph}^5), \quad (3.5)$$

where V is the volume of the nuclear refrigerant, T_e is the temperature of the electrons, T_{ph} is the temperature of the phonons, Σ the electron-phonon coupling constant, which depends on material and is for Cu $\Sigma = 2 \cdot 10^9 \text{ Wm}^{-3}\text{K}^{-5}$. Due to the T^5 dependence electron-phonon coupling is rather weak at low temperatures. The phonon heat capacity is extremely small at low temperatures compared to the electronic and nuclear heat capacities, thus we conclude that the phonons are completely thermalized with the electrons ($T_e = T_{ph}$) within an extremely short relaxation time.

3.3.2 Hyperfine Interaction

The hyperfine interaction is responsible for heat transport between nuclei and electrons. The time scale at which thermal equilibrium is reached between electrons and nuclei is determined by the spin-lattice relaxation time (τ_1). For a metal at low temperatures, $\tau_2 \ll \tau_1$, indicating that electrons and nuclei can have two different temperatures, a nuclear temperature T_n and an electron temperature T_e . Assuming that T_e is constant, one can define the spin relaxation time as follows

$$\frac{d}{dt} \left(\frac{1}{T_n} \right) = -\frac{1}{\tau_1} \left(\frac{1}{T_n} - \frac{1}{T_e} \right). \quad (3.6)$$

The hyperfine interaction is determined by the overlap integral between the electron wave function and the nuclei wave function. Only the conduction electrons are relevant for the overlap integral and their energies are distributed in a stripe of width $k_B T_e$ around the Fermi surface. Therefore, τ_1 is proportional to $1/T_e$, leading to the Korringa

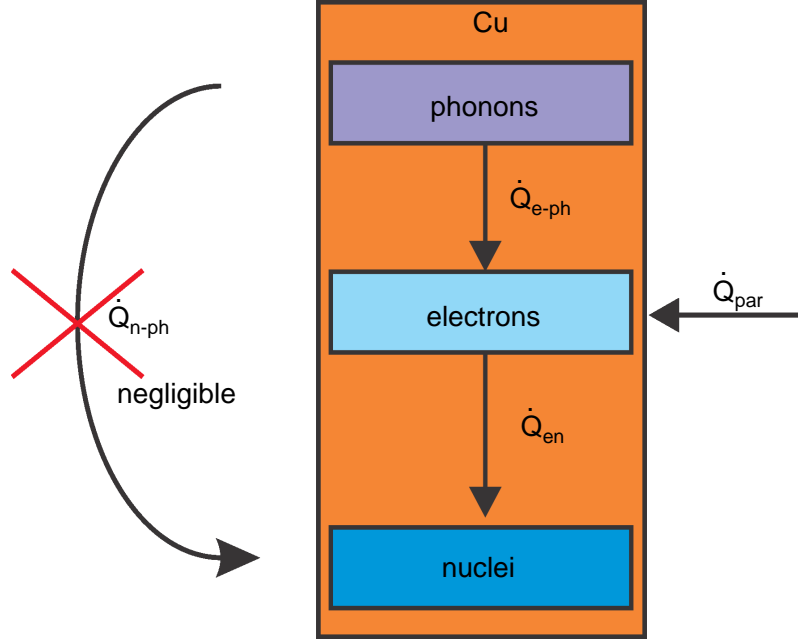


Figure 3.2: A schematic showing the different degrees of freedom present in the Cu refrigerant. Electrons and phonons interact through \dot{Q}_{e-ph} , while electrons and nuclei exchange heat via \dot{Q}_{en} . A parasitic heat leak \dot{Q}_{par} is introduced in the system through the electronic degree of freedom. The direct interaction between phonons and nuclei is negligible.

law

$$\tau_1 T_e = \kappa, \quad (3.7)$$

where κ is the Korringa constant, which is a material constant. The Korringa constant gives the strength of the hyperfine interaction between electrons and nuclei. Typical values for metals are a few K·s, e.g for Cu $\kappa = 1.2$ K·s, indicating that electrons and nuclei are well thermally coupled even at low temperatures. Using Eq. (3.7), it is possible to rewrite the Eq. (3.6) in the following way

$$\dot{T}_n = \frac{T_n}{\kappa} (T_e - T_n). \quad (3.8)$$

Usually the electrons are cold and the nuclei are hot, but during the demagnetization the heat flow is opposite and it can be written as

$$\dot{Q}_{en} = -nC_n \dot{T}_n = nC_e \dot{T}_e, \quad (3.9)$$

where C_e is the electrons heat capacity and n indicates the number of mole. Note that, in presence of an external B , the molar nuclear heat capacity is much larger than the electron heat capacity. Thus the thermal load of the electrons on the nuclei is negligible, indicating that T_e follows T_n even without an ideal adiabatic process. Therefore, we neglect the electronic contribution of Eq. (3.9). Substituting Eq. (3.3) and Eq. (3.8) into Eq. (3.9), we obtain

$$\dot{Q}_{en} = n \frac{\lambda_n B^2}{\mu_0 T_n \kappa} (T_e - T_n) . \quad (3.10)$$

This describes how the electrons are cooled during the demagnetization process through the nuclei. In presence of \dot{Q}_{par} leaking in our system, we can balance the cooling power of the nuclei \dot{Q}_{en} with \dot{Q}_{par} and we obtain the following relation

$$\frac{T_e}{T_n} = 1 + \frac{\dot{Q}_{par} \kappa \mu_0}{n \lambda_n B^2} . \quad (3.11)$$

As shown in Eq. (3.10) and Eq. (3.11), a heat leak can lead to a potentially significant temperature gradient between the electrons and nuclei. Thus, it is important to try to minimize the heat leaks to obtain an efficient cooling of the electrons via the nuclei.

3.4 Simulation AND

Here, we describe the procedure used to model the demagnetization. In order to solve numerically the differential equations utilized in the model, we consider finite small time steps (δt) in which the B -field is changed by $\delta B = \frac{dB}{dt} \delta t$, where $\frac{dB}{dt}$ is the ramp-rate of the magnetic field. In order to take into account the reduction of the nuclear temperature (δT_n) due to a ideal adiabatic demagnetization during δt , we use Eq. (3.4) rewritten in terms of δt

$$\delta T_n = T_n \frac{\delta B}{B} \longrightarrow \delta T_n = \frac{T_n}{B} \frac{dB}{dt} \delta t \quad (3.12)$$

Assuming a time independent \dot{Q}_{dyn} due to the ramping of the magnetic field, which warms up the nuclei, and a cooling power term given by δT_n . Using Eq. (3.9) and Eq. (3.12), T_n at time $t+\delta t$ is given by

$$T_n(t + \delta t) = T_n(t) + \frac{\dot{Q}_{dyn}}{C_n(T_n(t), B(t))} \delta t - \frac{T_n(t)}{B(t)} \frac{dB}{dt} \delta t, \quad (3.13)$$

The term $\frac{\dot{Q}_{dyn}}{C_n}$ accounts for loss of adiabaticity during the demagnetization, i.e. $\dot{Q}_{dyn}=0$ for an ideal adiabatic process. At time $t=0$, we assume that electrons and nuclei have the same temperature $T_e(0) = T_n(0)=9.5$ mK. It is reasonable to assume that T_e follows T_n , since the Korringa link is strong for temperatures above 1 mK and the nuclear heat capacity dominates over the electron heat capacity. Knowing $T_n(0)$, we calculate the next value $T_n(\delta t)$, using the Eq. (3.13). Next, we calculate $T_e(\delta t)$ using Eq. (3.11) with $\dot{Q}_{par}=\dot{Q}_{dyn}$ and knowing $T_n(\delta t)$, since the electrons are cooled by the nuclei through hyperfine interaction. In this way we can iteratively calculate $T_e(t)$, $T_n(t)$ and $B(t)$ for each time step. As shown in Fig 3.3, for high magnetic fields T_e follows T_n perfectly, while at low magnetic fields T_e deviates from T_n . In addition, T_n deviates from the nuclear temperature of the ideal adiabatic process $T_{n,adiabatic}$, the deviation is also due to the presence of \dot{Q}_{dyn} . The computed temperature T_e reproduces well the measured

electronic temperature T_{MFFT} . A small deviation is seen at low magnetic fields, however we observe a cooling of the MFFT after reaching B_f , due to the absence of Q_{dyn} at static B -fields, see Fig 3.3.

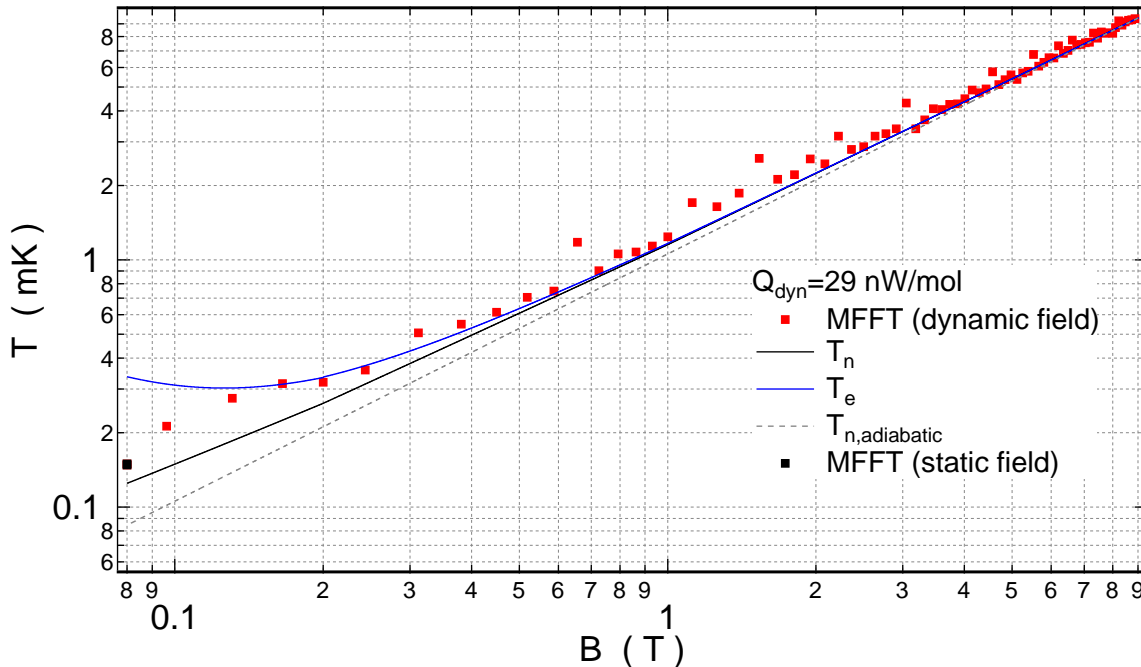


Figure 3.3: Calculated T_e and T_n as a function of the magnetic field during the demagnetization. The red squares indicate T_{MFFT} during the demagnetization, while the black square is the temperature measured at static field $B_f = 0.08$ T. The dashed line indicates the calculated nuclear temperature for the ideal adiabatic process

The detailed ramp rate series use in the experiment is fed into the model. To evaluate the performance of the demagnetization process, we use the efficiency $\xi = (T_i/T_f)/(B_i/B_f)$. Using the model, we can calculate ξ for each B -field, as shown in Fig 3.4. The calculated efficiency for the standard demagnetization rates agrees well with experimental data. As seen in Fig 3.4, changing the ramp-rates results in kinks in the simulated efficiency (orange curve), which is due to the fact that more time is needed to ramp the same difference in magnetic fields, despite a heat leak, which does not change when the ramp rate is changed. Thus, the heat absorbed per unit of magnetic field is increased for the lower ramp-rates, leading to a reduction of the efficiency, which is in agreement with the experimental data (red squares) in Fig 3.4. In addition, a constant \dot{Q}_{dyn} suggests the possibility to improve the efficiency, reducing

the duration of the demagnetization process. Indeed, doubling the ramp-rates during demagnetization increased the efficiency in the experiments, however the model shows only qualitatively the same behavior, see light blue curve Fig 3.4. The deviation between the data and the simulated efficiency for the fast AND process is not currently understood.

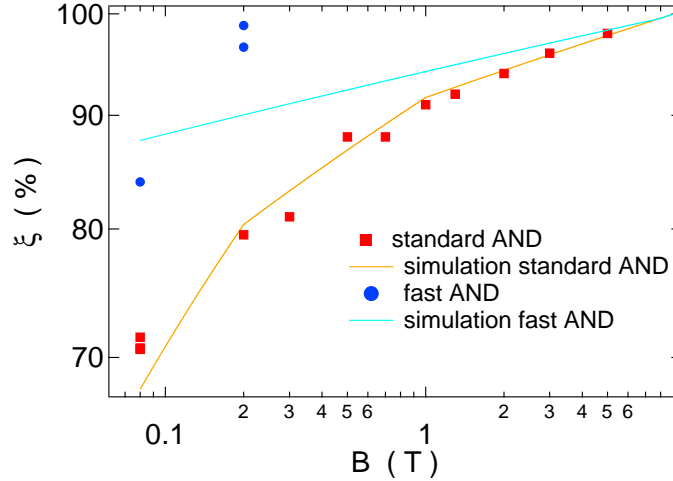


Figure 3.4: Efficiency as a function of the magnetic field. The orange line is the calculated efficiency for a standard AND, while the light blue line is the calculated efficiency obtained by doubling the ramp-rates.

Usually \dot{Q}_{dyn} is mainly due to eddy current heating, generated by sweeping of the B -field and vibrations of the Cu refrigerant relative to the magnetic field [33]. However, the model finds that \dot{Q}_{dyn} is constant in time and independent of B^2 or \dot{B}^2 , suggesting that \dot{Q}_{dyn} cannot just be explained with eddy current heating. In order to reproduce the final nuclear temperature of $\sim 120 \mu\text{K}$, which is extracted from the warm up curves presented in chapter 1, we need to assume $\dot{Q}_{dyn}=29 \text{ nW/mol}$. This value is much larger than the usual static heat leak $\sim 1 \text{ nW/mol}$, suggesting an additional unknown source of heat, which is active only while sweeping the magnetic field, but not proportional to B^2 or \dot{B}^2 . This heat needs to be transferred into the Cu reservoir through the electronic degree of freedom and then to the nuclei via hyperfine interaction. It is improbable that small magnetic field fluctuations in the present setup give rise to spin-flips processes, which would release heat into the nuclei. As a last speculation, it is possible that some heat could leak through the Al heat switches, which may be not

always in the superconducting states while sweeping the field.

Thus, we need to understand how the compensation of the magnetic field works in the region where the heat switches are located. A double 9 T magnet is used in the setup, it is designed to reduce the magnetic stray field down to few mT in the region of the heat switches using active cancellation coils. In addition to the double 9 T magnet the setup is equipped with an heat switch magnet used to tune the heat switch in the conductive or superconducting state. The heat switch field is also used to further compensate the stray field of the demagnetization magnet.

Figure 3.5 shows the heat switch field as a function of the demagnetization field during the refrigeration cycle. The experimental points are obtained by varying the demagnetization field and simultaneously adjusting the heat switch field. The superconducting transition of the heat switches is monitored by measuring the temperature of the Cu plate, which abruptly increases when the heat switches change into the superconducting state while it immediately decreases when the heat switches become normal conducting. The compensation was calibrated during the early characterization of the setup and might not be valid anymore, since at that time the magnetic thermometers were not properly working. This could introduce a systematic error in the calibration measurements and thus the calibration should be repeated. The estimation of the heat flow through a fully normal conductive heat switch is an order of magnitude higher than \dot{Q}_{dyn} needed for our simulation. Alternatively, the Al pieces (~ 1 cm in size) might only partially be normal conducting.

In conclusion we show that a simple numerical model can explain qualitatively the data and it predicts that a faster process improves the efficiency of the process to above 80 %, however the origin of the Q_{dyn} is not currently understood but it might be due to heat leaking through the switches.

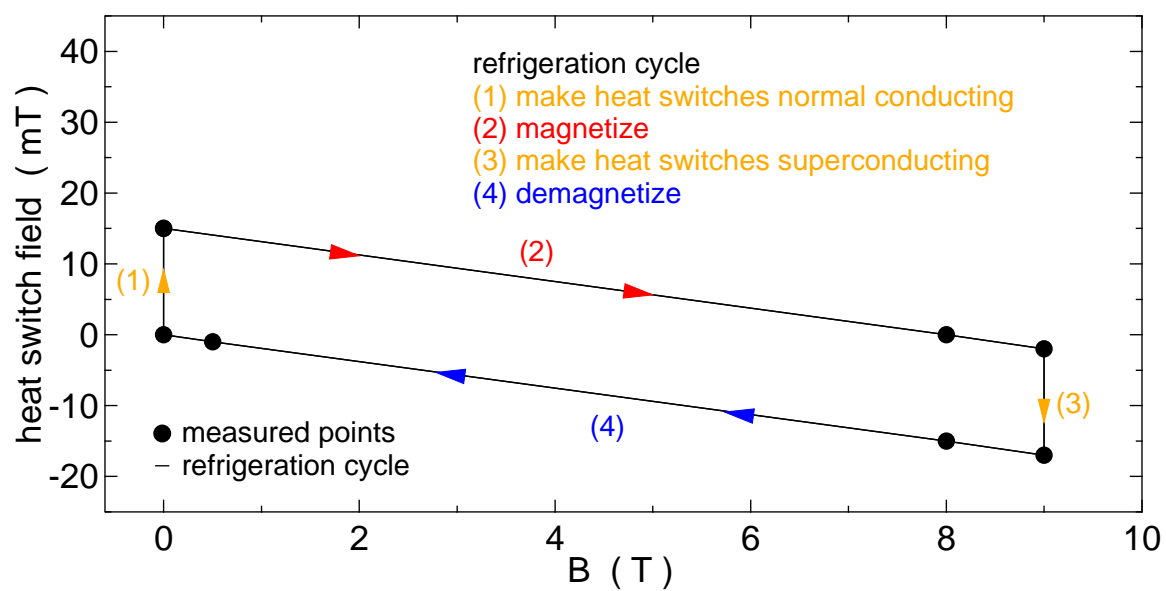


Figure 3.5: The heat switch magnet as a function of the demagnetization magnet during the refrigeration cycle. The different parts of the refrigeration path are indicated by numbers.

4 Tunnel-Junction Thermometry Down to Millikelvin Temperatures

A. V. Feshchenko^{1*}, L. Casparis^{2*}, I. M. Khaymovich¹, D. Maradan², O.-P. Saira¹, M. Palma², M. Meschke¹, J. P. Pekola¹ and D. M. Zumbühl²

¹ *Low Temperature Laboratory, Aalto University, FI-00076 Aalto, Finland*

² *Department of Physics, University of Basel, CH-4056 Basel, Switzerland*

Abstract

We present a simple on-chip electronic thermometer with the potential to operate down to 1 mK. It is based on transport through a single normal-metal–superconductor tunnel junction with rapidly widening leads. The current through the junction is determined by the temperature of the normal electrode that is efficiently thermalized to the phonon bath, and it is virtually insensitive to the temperature of the superconductor, even when the latter is relatively far from equilibrium. We demonstrate here the operation of the device down to 7 mK and present a systematic thermal analysis.

* These authors contributed equally to this work.

This chapter was published in *Phys. Rev. Appl.* **4**, 034001 (2015).

4.1 Introduction

On-chip electronic thermometry is an important part of modern research and commercial applications of nanotechnology, and it has been studied already for several decades; see Ref. [60] and references therein. Many of these thermometers are based on tunnel junctions or quantum dots [61–63]. Temperature sensors based on normal (N) and superconducting (S) metal tunnel junctions are used in a wide range of experiments [42, 64, 65] and applications [66, 67]. An example of such a device is a primary Coulomb blockade thermometer (CBT) that is based on normal-metal tunnel junctions with an insulator “I” as a tunnel barrier (NIN) [32, 68], where the electronic temperature can be obtained by measuring the smearing of the single-electron blockade. One more example is an SNS thermometer [69], whose critical current I_c depends strongly on the temperature. Primary electronic thermometry has also been successfully demonstrated down to 10 mK using the shot noise of a tunnel junction (SNT) [70–72]. Nowadays, a standard dilution refrigerator reaches a temperature of [5..10] mK, with a record of 1.75 mK [2, 3]. Nevertheless, a thermometer that has a modest structure and a simple but accurate temperature reading at sub-10 mK temperatures and does not require a complicated experimental setup is still missing. For this purpose, we present an NIS junction that is widely used both as a refrigerating element and a probe of the local electronic temperature in different experiments and applications [42, 64–67, 73–75]. The possibility to use the NIS junction at sub-10 mK temperatures makes this thermometer suited for cryogenic applications at low temperatures. For instance, quantum information is a highly focused and rapidly developing field in modern physics. For many realizations, such as superconducting and quantum dot qubits, one needs to define a set of quantum states at low temperature that are well separated and well controlled and insensitive to noise and decoherence effects [76]. Several experimental realizations of two-level systems [12, 77, 78] suggest that decreasing temperature further will increase the coherence times as well as improve charge sensitivity. We think that our thermometer will be interesting for a community who is willing to discover

new physics as well as improve already existing devices that require low temperatures for their proper functioning. The NIS thermometer is easy to operate compared to SNT [70, 71], and its thermalization is quite straightforward compared to CBT [32] due to the single junction configuration and can be combined on-chip with other solid-state devices. A measurement of the NIS current-voltage (I - V) characteristic yields a primary temperature reading.

In this paper, we study both experimentally and theoretically an on-chip electronic thermometer based on a single NIS tunnel junction at sub-10 mK temperatures. We demonstrate the operation of the NIS thermometer down to 7.3 mK. In addition, we develop a thermal model that explains our measurement data and shows that self-heating effects remain negligible for temperatures down to 1 mK.

4.2 Theoretical Background

Transport through an NIS junction has strong bias and temperature dependence. Near zero bias voltage, the current is suppressed due to the superconducting gap Δ [79]. When biased at voltage V , the current depends on temperature due to the broadening of the Fermi distribution $f_N(E) = [\exp(E/k_B T_N) + 1]^{-1}$ in the normal metal with temperature T_N and Boltzmann constant k_B . The current can be expressed as [79]

$$I = \frac{1}{2eR_T} \int_{-\infty}^{+\infty} dE n_S(E) [f_N(E - eV) - f_N(E + eV)], \quad (4.1)$$

where R_T is the tunneling resistance of the junction and E is the energy relative to the chemical potential.

In the superconductor, the Bardeen-Cooper-Schrieffer (BCS) density of states is smeared and typically described by the Dynes parameter γ , which can be expressed as $n_S(E) = |\Re(u/\sqrt{u^2 - 1})|$ (see supplemental material in Ref. [80]), where $u = E/\Delta(T_S) + i\gamma$ and T_S is the temperature of the superconductor. Possible origins of γ include broadening of the quasiparticle energy levels due to finite lifetime [81],

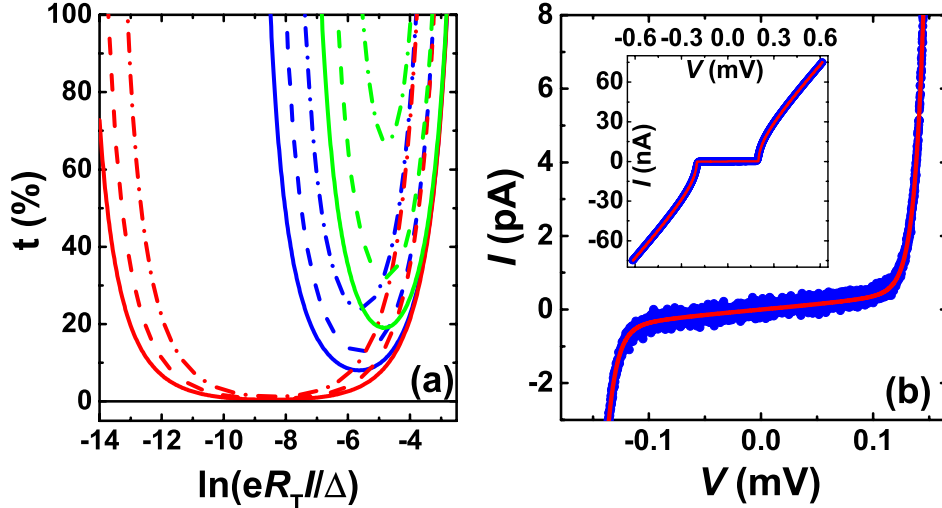


Figure 4.1: In panel (a), we show the relative deviation of the present thermometer reading using method B with a numerically calculated I - V , Eq. (4.1). Sets of curves present the values of t for three γ parameters: 10^{-7} , $2.2 \cdot 10^{-5}$ (the actual value in the experiment), and 10^{-4} shown as red, blue and green curves from left to right. For each γ , temperatures 1, 3, and 7 mK are shown as dash-dotted, dashed, and solid lines, respectively. All curves are calculated using the parameters of the measured device with $\Delta = 200 \mu\text{eV}$ and $R_T = 7.7 \text{ k}\Omega$. The main panel (b) shows the measured I - V characteristic (blue dots) together with the full fit (solid red line) enlarged in the superconducting gap region. *Inset:* Measured and calculated I - V curve on a wider voltage scale at approximately 10 mK.

Andreev current [82, 83], as well as photon-assisted tunneling caused by high-frequency noise and black-body radiation [80]. The typical experimental range of γ for Al-based³ tunnel junctions is 10^{-4} to 10^{-5} for a single NIS junction [80, 88], getting as low as 10^{-7} in SINIS single-electron transistors with multistage shielding [89].

One can determine T_N from a measured I - V curve using Eq. (4.1). As we show below, the self-heating of both N and S electrodes has a small effect on the I - V characteristic; thus, for now, we neglect these effects. Therefore, we assume temperatures to be small, $k_B T_{N,S} \ll eV, \Delta(T_S)$, and the superconducting gap to be constant and equal to its zero-temperature value Δ . In this case for $eV < \Delta$, one can approximate Eq. (4.1) by

$$I \simeq I_0 \exp\left(\frac{-(\Delta - eV)}{k_B T_N}\right) + \frac{\gamma V}{R_T \sqrt{1 - (eV/\Delta)^2}}, \quad (4.2)$$

³Tunnel junctions based on Nb, NbN or NbTiN have higher γ values, usually up to 10^{-2} [84–87]

where $I_0 = \sqrt{2\pi\Delta k_B T_N}/2eR_T$ [64, 82]. Here the second term stands for the corrections to the I - V characteristic due to smearing. It leads to the saturation of the exponential increase of the current at low bias values. In the regime of moderate bias voltages, one can neglect this term and invert Eq. (4.2) into

$$V = \frac{\Delta}{e} + \frac{k_B T_N}{e} \ln(I/I_0). \quad (4.3)$$

This equation provides a way to obtain the electronic temperature T_N^B by only fundamental constants and by the slope of the measured I - V characteristic on a semilogarithmic scale as

$$T_N^B(V) = \frac{e}{k_B} \frac{dV}{d(\ln I)}. \quad (4.4)$$

Equation (4.4) allows us to use the NIS junction as a primary thermometer, however, with some limitations. One can include the effects of γ into Eq. (4.4) by subtracting the last term in Eq. (4.2) from the current I and obtain a better accuracy. We do not take this approach here, since the main advantage of Eq. (4.4) is its simplicity as a primary thermometer without any fitting parameters.

Next, we will compare the two methods used to extract the electronic temperature from the measured I - V curves. In method A, we employ Eq. (4.1) and perform a nonlinear least-squares fit of a full I - V curve with T_N as the only free parameter. The value of T_N obtained in this manner, named T_N^A , is not sensitive to γ . Method B is based on the local slope of the I - V , see Eq. (4.4). The smearing parameter γ has an influence on the slope of the I - V characteristic and, thus, induces errors in the temperature determination. The temperature T_N^B is extracted as the slope of measured V vs $\ln I$ over a fixed I range for all temperatures where Eq. (4.4) is valid. In the experiment, it is usually difficult to determine the environment parameters precisely, but one can determine γ from the ratio of R_T and the measured zero-bias resistance of the junction. The I - V which takes the γ parameter into account, see Eq. (4.2), gives indistinguishable

results from the ones obtained by method A.

We evaluate the influence of the γ parameter on the relative deviations of the present thermometer based on method B numerically, as shown in Fig. 4.1(a). This deviation t is defined as the relative error $t = (T_N^B/T_N) - 1$. We show the values of t vs $\ln(eR_T I/\Delta)$ for two extreme cases $\gamma = 10^{-7}$, 10^{-4} and for $\gamma = 2.2 \cdot 10^{-5}$ extracted from the present experiment at temperatures of 1, 3 and 7 mK. The lowest bath temperature is 3 mK, and 7 mK is the saturation of the electronic temperature in the current experiment. The larger the values of γ and the lower the temperature, the higher the relative deviations. In addition, the range of the slope used to extract T_N^B shrinks with increasing γ and with decreasing temperature, see e.g. red curves in Fig. 4.1(a). Thus, reducing the leakage will significantly improve the accuracy of the device, especially towards lower temperatures. Possible avenues for suppressing γ include improved shielding [89, 90] and encapsulating the device between ground planes intended to reduce the influence of the electromagnetic environment [80]. Finally, higher tunneling resistance of the junction decreases Andreev current [91]. We note that one can also use $dV/d(\ln g)$ as a primary thermometer, where $g = dI/dV$ is the differential conductance – typically a more precise measurement since it is done with a lock-in technique. Compared to Eq. (4.4), this method has the minimal deviation t reduced by at least a factor of 3.5 for $T_N \geq 1$ mK (6 for $T_N \geq 10$ mK), though exhibiting qualitatively similar dependencies on γ and T_N .

4.3 Experimental Realization and Measurement Techniques

Next, we describe the realization of the NIS thermometer that is shown together with a schematic of the experimental setup in the scanning-electron micrograph in Fig. 4.2. The device is made by electron-beam lithography using the two-angle shadow evaporation technique [92]. The ground plane under the junction is made out of 50 nm of Au. To electrically isolate the ground plane from the junction, we cover the Au layer with 100 nm of AlO_x using atomic layer deposition. Next, we deposit a layer of $d_S = 40$ nm

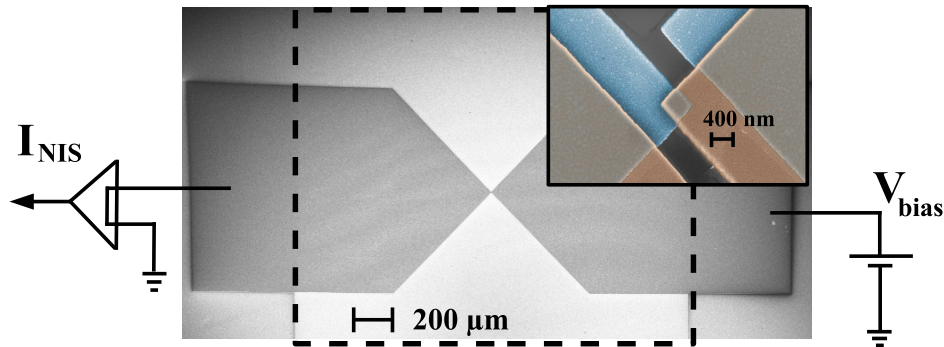


Figure 4.2: A scanning-electron micrograph of the NIS device together with a schematic of the experimental setup. In the main panel, the S and N leads of the junction visible, and underneath the pads, the ground plane of a square shape is indicated by a dashed line. The enlarged *inset* shows the actual tunnel junction where the S and N leads are indicated by blue and brown color, respectively.

of Al that is thermally oxidized *in situ*. The last layer is formed immediately after the oxidation process by deposition of $d_N = 150$ nm of Cu, thus creating an NIS tunnel junction with an area $A = (380 \times 400)$ nm². The geometry of the junction is chosen such that the leads immediately open up at an angle of 90° and create large pads with areas of $A_N = A_S = 1.25$ mm² providing good thermalization. The S lead is covered by a thick normal-metal shadow as shown in brown in the inset of Fig. 4.2, where N and S layers are interfaced by the same insulating layer of AlO_x as the junction.

The experiment is performed in a dilution refrigerator (base temperature 9 mK) where each of the sample wires is cooled by its own, separate Cu nuclear refrigerator (NR) [31], here providing bath temperatures T_{bath} down to 3 mK. Nuclear refrigerator temperatures after demagnetization are highly reproducible and obtained from the precooling temperatures and previously determined efficiencies [32]. Temperatures above ~ 9 mK are measured with a cerium magnesium nitrate thermometer which is calibrated against a standard superconducting fixed-point device. Since the sample is sensitive to the stray magnetic field of that applied on the nuclear refrigerators, this field is compensated down to below 1 G using a separate solenoid. The I - V curves (see Fig. 4.2 for the electrical circuit) are measured using a home-built current preamplifier with input offset-voltage stabilization [93] to minimize distortions in the I - V curves.

Filtering, radiation shielding and thermalization are crucial for obtaining a low γ and

low device temperatures. Each sample wire goes through 1.6 m of thermocoax, followed by a silver epoxy microwave filter [34], a 30 kHz low-pass filter and a sintered silver heat exchanger in the mixing chamber before passing the Al heat switch and entering the Cu nuclear stage. The setup is described in detail in Ref. [32] and has been further improved here (see 4.7 Appendix for more details).

4.4 Results and Discussion

In Fig. 4.1(b), the measured I - V characteristic in the superconducting gap region is shown by blue dots. The solid red line corresponds to the full fit based on method A. In the inset, we present the I - V characteristic at a larger voltage scale used to extract R_T .

In Fig. 4.3(a), the measured I - V 's of the NIS junction are shown in logarithmic scale by blue dots at various $T_{\text{bath}} = [100..3]$ mK from left to right. The full fits are shown as dashed red lines. The tunneling resistance $R_T = 7.7 \text{ k}\Omega$ and the Dynes parameter $\gamma = 2.2 \cdot 10^{-5}$ used in all these fits are determined based on the I - V 's shown in Fig. 4.1(b) at high and low voltages, respectively. For the lowest temperatures, T_N from the nonlinear fit depends strongly on the superconducting gap⁴, making it difficult to determine the gap with high enough accuracy⁵. However, Eq. (4.1) gives a possibility to perform a nonlinear least-squares fit and Eq. (4.3) gives a linear fit, where the parameters Δ and T_N are responsible for the offset and the slope, respectively. Therefore, at high temperatures (~ 100 mK in the present experiment), one can narrow down the uncertainty in Δ such that T_N becomes essentially an independent parameter for the fits. Thus, the gap extracted from the high-temperature data using Eq. (4.1) remains fixed, $\Delta = 200 \pm 0.5 \text{ }\mu\text{eV}$, for all temperatures below 100 mK. In addition, we show as solid black lines an exponential I - V dependence corresponding to method B with a fitting range between 5 and 400 pA. The enlarged inset shows the I - V curves at temperatures of 10 and 7 mK. The I - V characteristics presented in Fig. 4.3(a) agree well

⁴A reduction of the superconducting gap by 0.1 % changes T_N by 10 % at the lowest temperature.

⁵With the given experimental uncertainties, we can determine the gap with a precision of 0.25 % ($\pm 0.5 \text{ }\mu\text{eV}$).

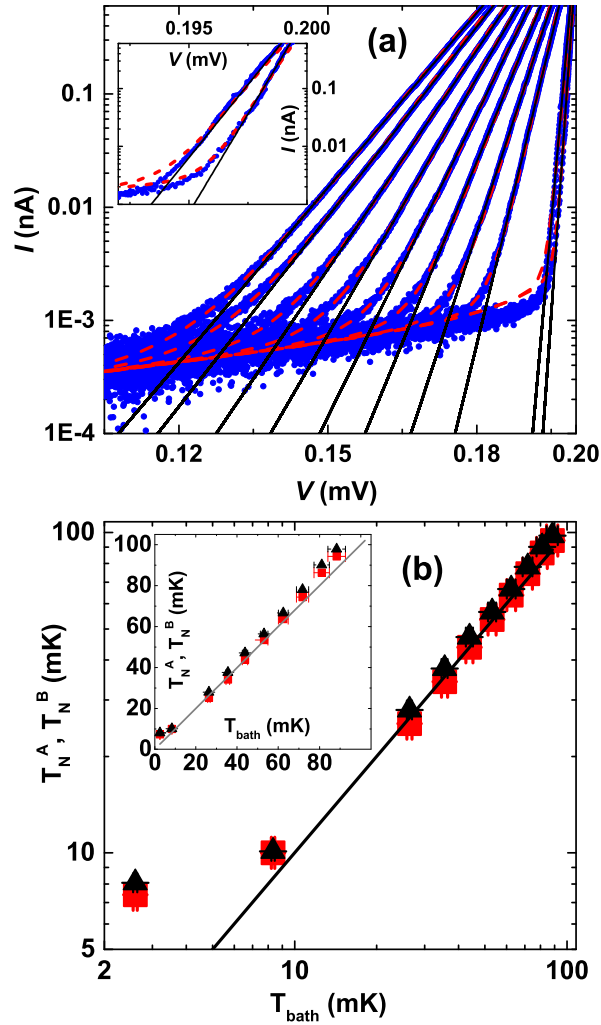


Figure 4.3: Panel (a) shows measured I - V 's (blue dots) when T_{bath} is lowered from left to right together with fits as solid black and dashed red lines (see text). *Inset:* Close-up of two I - V 's for temperatures of 10 and 7 mK. The electronic temperature extracted from both the full fit (red squares) of the I - V 's and their slopes (black triangles) are shown in (b).

with the theoretical expressions in Eqs. (4.1) and (4.2) (the latter form is not shown). In Fig. 4.3(b), we show the electronic temperatures obtained using method A (red squares) and method B (black triangles) vs T_{bath} . Method A (B) shows a relative error in the electronic temperature up to 6% (11%). The error in method B is larger, as we neglect the influence of the γ parameter.

The lowest temperature obtained from the full fit is $T_N^A = 7.3$ mK with statistical uncertainty of 5% at $T_{\text{bath}} = 3$ mK. The NIS temperature decreases slowly over time, arriving at 7.3 mK several weeks after the cool down from room temperature. This suggests that internal relaxation causing a time-dependent heat leak, e.g. in the silver epoxy sample holder, is limiting the minimum temperature. Future improvements will employ low-heat-release materials better suited for ultralow temperatures such as sapphire or pure annealed metals, e.g., for the socket and chip carrier, minimizing organic noncrystalline substances such as epoxies.

4.5 Thermal Model

The total power dissipated in the device is equal to $IV = \dot{Q}_{\text{NIS}}^N + \dot{Q}_{\text{NIS}}^S$, where \dot{Q}_{NIS}^N and \dot{Q}_{NIS}^S are the heat powers to the normal metal and to the superconductor, respectively. The heat released to the superconductor is given by

$$\dot{Q}_{\text{NIS}}^S = \frac{1}{e^2 R_T} \int E_S n_S(E) [f_N(E - eV) - f_S(E)] dE, \quad (4.5)$$

where $E_S = E$ is the quasiparticle energy. To evaluate \dot{Q}_{NIS}^N , one has to substitute E_S by $E_N = (eV - E)$ in Eq. (4.5). Almost all of the heat is delivered to the superconductor in the measured (subgap) bias range, thus, $\dot{Q}_{\text{NIS}}^S \sim IV$ and $\dot{Q}_{\text{NIS}}^N \ll \dot{Q}_{\text{NIS}}^S$.

So far, we neglect all self-heating effects both in the normal metal and in the superconductor. To justify the no-self-heating assumption, we check numerically and analytically these self-heating effects. We sketch the analytical arguments in section 4.7 Appendix. Here we state the main results obtained from the thermal model.

Self-heating of the superconductor can take place due to the exponential suppression of thermal conductivity and the weak electron-phonon (e-ph) coupling, especially at low temperatures. We find that the superconductor temperature T_S stays below 250 mK in the subgap bias range $|V| \leq \Delta/e$ and does not influence the thermometer reading. In this bias range and at $T_{\text{bath}} = 3$ mK, we estimate based on the numerical calculations the temperature of the superconductor $T_S = 145$ mK and the power injected to the superconductor is $IV \approx 90$ fW. At the same time, we evaluate the relative change of the slope to be small $|t| \lesssim 5 \cdot 10^{-3}$ at $I \lesssim 1$ nA. In conclusion, the temperatures obtained from both methods A and B are affected by less than 0.5% by self-heating of the superconductor⁶. In addition, the normal metal might get self-heated due to weak electron-phonon coupling and backflow of heat from the superconductor [94]. The influence of the self-heating of the normal metal down to 1 mK temperature affects the temperature obtained from both methods A and B by less than 0.5% as well, as in the case of self-heating of the superconductor.

4.6 Conclusions

In conclusion, we have demonstrated experimentally the operation of an electronic thermometer based on a single NIS tunnel junction. The thermometer agrees well with the refrigerator thermometer down to about 10 mK and reaches a lowest temperature of 7.3 mK at $T_{\text{bath}} = 3$ mK, currently limited by a time-dependent heat leak to the sample stage. We have discussed several possible improvements of the present device and experimental setup. Finally, we have shown that self-heating in the normal metal and in the superconductor on the full I - V or its slope is negligible, paving the way for NIS thermometry down to 1 mK if the experimental challenges can be overcome.

⁶The temperature of the superconductor will affect T_N through the dependence of the I - V curve on the magnitude of the gap. The geometry of the device can influence the number of quasiparticles and, consequently, the effective temperature of the superconductor.

Acknowledgments

We thank G. Frossati, G. Pickett, V. Shvarts, and M. Steinacher for valuable input. We acknowledge the availability of the facilities and technical support by Otaniemi Research Infrastructure for Micro- and Nanotechnologies (OtaNano). We acknowledge financial support from the European Community FP7 Marie Curie Initial Training Networks Action Q-NET 264034, MICROKELVIN (Project No. 228464), SOLID (Project No. 248629), INFERNOS (Project No. 308850), EMRP (Project No. SIB01-REG2), and the Academy of Finland (Projects No. 284594 and No. 272218). This work is supported by Swiss Nanoscience Institute, NCCR QSIT, Swiss NSF, and an ERC starting grant under agreement No. 207599.

4.7 Appendix

Experimental Techniques

The setup described in Ref. [32] was improved as follows. First, a ceramic chip carrier was replaced by silver epoxy parts which remain metallic to the lowest temperatures, allowing more efficient cooling. Further, the sample – previously mounted openly inside the cold-plate radiation shield together with the nuclear stage – is enclosed in an additional silver shield, sealed with silver paint against the silver epoxy socket, and thermalized to one of the Cu refrigerators, see Fig. 4.4. Finally, each wire is fed into the sample shield through an additional silver epoxy microwave filter. While previously saturating at 10 mK or above [32], metallic CBTs have given temperatures around 7 mK after the improvements [13, 34], comparable to the NIS temperatures presented here.

Estimates of the Subgap Conductance

The Dynes parameter γ can be attributed to the higher-order processes such as Andreev tunneling events. Assuming ballistic transport and an effective area of the conduction

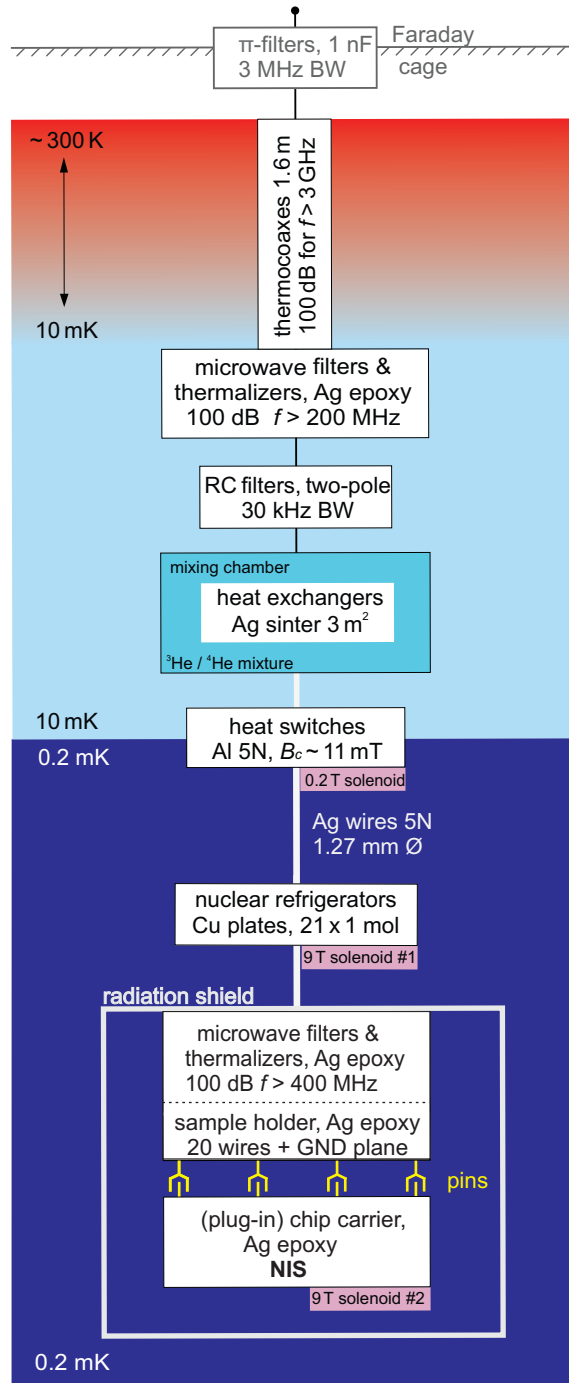


Figure 4.4: Scheme of a dilution unit together with a nuclear stage. Radiation shields (not shown) are attached to the still and cold plate (~ 50 mK). The RC filters are $1.6\text{ k}\Omega/2.2\text{ nF}$ and $2.4\text{ k}\Omega/470\text{ pF}$. The 21 NR plates are $(32 \times 2.5 \times 90)\text{ mm}^3$ each, amounting to 64 g Cu per plate. The NRs cool as low as 0.2 mK. In the present experiment, the lowest T_{bath} used is 3 mK. Compared to Ref. [32], the improved setup depicted here features a Ag epoxy socket, a Ag epoxy chip carrier, and a second filtering stage with radiation-tight feedthroughs into an additional sample radiation shield. The abbreviations BW, B_c and GND presented in the schematic stand for bandwidth, critical magnetic field and electrical ground, respectively.

channel $A_{ch} = 30 \text{ nm}^2$ [95, 96], a simple estimate of subgap Andreev conductance reads $\sigma_{AR} = R_K/(8NR_T) = 8.5 \cdot 10^{-5}$ in units of R_T^{-1} , where R_K is the resistance quantum, N is the effective number of conduction channels, $N = A/A_{ch}$, where A is the area of the junction. Alternatively, the estimate based on diffusively enhanced Andreev conductance yields $7.5 \cdot 10^{-5}$ of corresponding dimensionless conductance. These values are of the same order of magnitude as in our experiment ($\gamma = 2.2 \cdot 10^{-5}$) and fall in the range of earlier experiments [83].

Theoretical Estimates for the Relative Deviations of the Present Thermometer

The theoretical deviations of $dV/d(\ln I)$ at $\gamma = 2.2 \cdot 10^{-5}$ numerically calculated from I - V , Eq. (4.1), are rather large, particularly at low temperatures ($\sim 30\%$ at 1 mK; see solid blue curve in Figs. 4.1(a) and 4.5). Measuring differential conductance $g = dI/dV$ rather than current I significantly reduces the predicted deviations $t_g = T_N^{slope,g}/T_N - 1$, where $T_N^{slope,g} = [dV/d(\ln g)]e/k_B$. The minimum of these deviations gets broader and potentially reduces measurement noise since it is a lock-in measurement – overall strengthening method B. In Fig. 4.5, we show two sets of curves for t_g (thick purple curves) and t (thin blue curves) from left to right for comparison. Sets are calculated based on the experimental parameters for $\gamma = 2.2 \cdot 10^{-5}$, $\Delta = 200 \text{ } \mu\text{eV}$, and $R_T = 7.7 \text{ k}\Omega$. Each set corresponds to the temperatures 1, 3, and 7 mK and is shown as dash-dotted, dashed and solid lines, respectively. Here, the t set is identical to the set with $\gamma = 2.2 \cdot 10^{-5}$ that is shown in Fig. 4.1(a).

Self-Heating of the Superconductor

We study the heat transport in the present geometry (see Fig. 4.2) by a diffusion equation assuming a thermal quasiparticle energy distribution [97, 98]

$$-\nabla(\kappa_S \nabla T_S) = u_S, \quad (4.6)$$

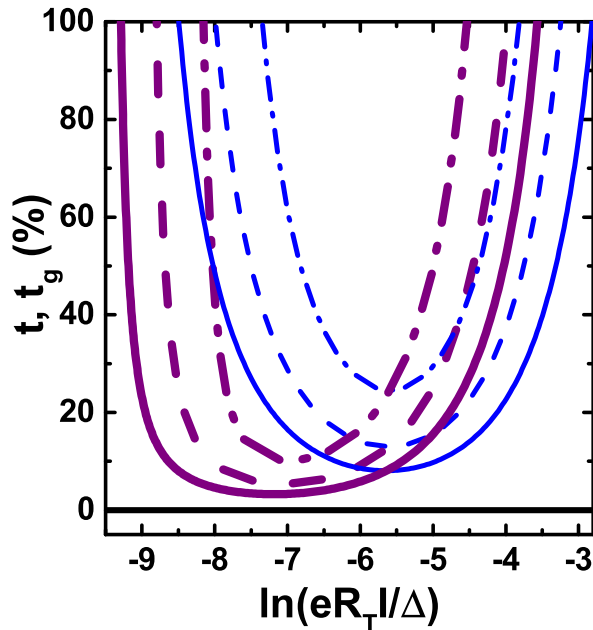


Figure 4.5: The theoretical deviations t and t_g of the thermometer reading using method B based on $I(V)$ and $g(V)$, respectively. These deviations are shown for temperatures 1, 3, and 7 mK as dash-dotted, dashed and solid lines, respectively. Parameters used are $\gamma = 2.2 \cdot 10^{-5}$, $\Delta = 200 \mu\text{eV}$, and $R_T = 7.7 \text{ k}\Omega$ as in the actual experiment.

where we set a boundary condition near the junction $-\bar{n}_{\text{inner}}\kappa_S\nabla T_S|_{\text{junct}} = \dot{Q}_{\text{NIS}}^S/A$, where \bar{n}_{inner} is the inner normal to the junction. The thermal conductivity in the superconductor is

$$\kappa_S = \frac{6}{\pi^2} \left(\frac{\Delta}{k_B T_S} \right)^2 \exp\left(\frac{-\Delta}{k_B T_S}\right) L_0 T_S \sigma_{Al}, \quad (4.7)$$

where L_0 is the Lorenz number, and $\sigma_{Al} = 3 \cdot 10^7 (\Omega\text{m})^{-1}$ is the electrical conductivity of the Al film in the normal state [98]. We take into account the T_S dependence of the gap at low temperatures, $\Delta(T_S)/\Delta \simeq 1 - \sqrt{2\pi k_B T_S/\Delta} \exp(-\Delta/k_B T_S)$. The absorbed heat is given by $u_S = \dot{q}_{e-ph}^S + \dot{q}_{\text{trap}}$. Here, the first term is the electron-phonon power $\dot{q}_{e-ph,S} \simeq \Sigma_{Al}(T_S^5 - T_p^5) \exp(-\Delta/k_B T_S)$ [99], where $\Sigma_{Al} = 3 \cdot 10^8 \text{ W K}^{-5} \text{ m}^{-3}$ is the material-dependent electron-phonon coupling constant. The phonon temperature T_p is assumed to be equal to T_{bath} . Because of weak electron-phonon coupling, nearly all the heat is released through the (unbiased) normal-metal shadow (see Fig. 4.6) that acts as a trap for quasiparticles, \dot{q}_{trap} .

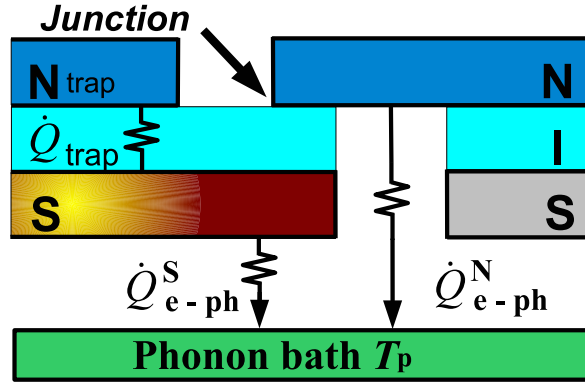


Figure 4.6: Thermal diagram of the NIS thermometer. This schematic does not reflect the real thicknesses of the materials. In this thermal model we assume the normal metal shadow that acts as the trap to be at T_{bath} .

Here, the conductance of the trap per unit area is the same as for the tunnel junction $\sigma_T = 1/(R_TA)$. Therefore, the heat removed per volume by this trap \dot{q}_{trap} can be calculated using Eq. (4.5) at $V = 0$, $T_N = T_{\text{bath}}$ and substituting R_T by d_S/σ_T . Thus, we derive the temperature of the superconductor T_S from Eq. (4.6) in 2D in polar coordinates using radial approximation for the sample geometry, which can then be written as [98]

$$\sqrt{\frac{2\pi k_B T_S}{\Delta(T_S)}} \exp\left(\frac{-\Delta(T_S)}{k_B T_S}\right) \equiv \alpha \dot{Q}_{\text{NIS}}^S. \quad (4.8)$$

Here, we assume $\dot{Q}_{\text{NIS}}^S \approx IV$, and $\alpha = \sqrt{\pi} e^2 G / [d_S \sigma_{Al} \sqrt{2k_B T_S \Delta^3(T_S)}]$ is a coefficient that depends on T_S and the dimensionless parameter $G = \ln(\lambda/r_0)/\theta \approx [2..3]$ is logarithmically dependent on the sample geometry [98]. Here, λ is the relaxation length of the order of $\sim [10..100] \mu\text{m}$, and $r_0 = 2A/(\pi d_N) \simeq 500 \text{ nm}$ is the radius of the contact in the present device. After substitution of all the parameters, we find that the superconductor temperature T_S does not influence the thermometer reading, as $T_S \lesssim 250 \text{ mK}$ in the subgap bias range $|V| \leq \Delta/e$. We estimate T_S to be $\sim 145 \text{ mK}$ in this bias range at $T_{\text{bath}} = 3 \text{ mK}$ corresponding to the power injected to the superconductor as $IV \sim 90 \text{ fW}$, and the quasiparticle density [98] as $n_{qp} = 0.3 \mu\text{m}^{-3}$. In addition, we evaluate the relative change of the slope to be small $|t| \lesssim 5 \cdot 10^{-3}$ at $I \lesssim 1 \text{ nA}$. In conclusion, the temperatures obtained from both methods A and B are affected by less

than 0.5 % by self-heating of the superconductor.

Self-Heating of the Normal Metal

For self-heating of the normal metal, one can solve the diffusion equation (4.6), taking into account the same boundary condition as above with all S indices replaced by N , where $\kappa_N = L_0\sigma_{Cu}T_N$ is the thermal conductivity of the normal metal, and the electrical conductivity of Cu is assumed to be $\sigma_{Cu} = 5 \cdot 10^7 (\Omega\text{m})^{-1}$ [100]. The heat absorbed in the normal metal is $u_N = \dot{q}_{e-ph}^N + \dot{q}_{\text{wire}}^N$. The heat conduction through the gold bonding wires \dot{q}_{wire}^N is taken into account only at the point where it is attached to the normal-metal pad, whereas the electron-phonon interaction \dot{q}_{e-ph}^N is effective in the full volume of the normal metal. The volumetric electron-phonon power is $\dot{q}_{e-ph}^N = \Sigma_{Cu}(T_N^5 - T_p^5)$, where $\Sigma_{Cu} = 2 \cdot 10^9 \text{ W K}^{-5} \text{ m}^{-3}$ is the electron-phonon coupling constant of copper. Here, we consider the effect of the heat removed by the bonding wires on temperature only in the normal metal, thus, $\dot{q}_{\text{wire}}^N = L_0\sigma_{Au}(T_N^2 - T_{\text{bath}}^2)/2L_{\text{wire}}d_N$. The length of the gold bonding wire is $L_{\text{wire}} \simeq 5 \text{ mm}$ and $\sigma_{Au} = 1.8 \cdot 10^9 (\Omega\text{m})^{-1}$ is the electrical conductivity of gold measured at low temperatures. The thermal relaxation length in the normal metal [60] is

$$l_N = \left(T_{\text{bath}}^{p/2-1}\right)^{-1} \sqrt{\frac{\sigma_{Cu}L_0}{2\Sigma_{Cu}}}. \quad (4.9)$$

We substitute $p = 5$ and $T_{\text{bath}} = 10 \text{ mK}$ and obtain $l_N = 17.5 \text{ mm}$. Since all the dimensions of the present device are smaller than 1.5 mm, there is only a weak temperature gradient over the normal-metal electrode due to its good heat conduction, and the weak electron-phonon coupling at low temperatures. By solving the heat-balance equation $\dot{Q}_{\text{NIS}}^N = \dot{Q}_{e-ph}^N + \dot{Q}_{\text{wire}}^N$ and assuming no external heat leaks, one can calculate T_N . Here, the heat released through electron-phonon coupling is $\dot{Q}_{e-ph}^N = \Omega_N \dot{q}_{e-ph}^N$, where $\Omega_N = A_N d_N$ is the volume of the N electrode. The heat released through $N_{\text{wire}} = 2$ bonding wires is $\dot{Q}_{\text{wire}}^N = \dot{q}_{\text{wire}}^N N_{\text{wire}} A_{\text{wire}} d_N$, where its cross-sectional area

is $A_{\text{wire}} = \pi r_{\text{wire}}^2$ with a radius $r_{\text{wire}} = 16 \mu\text{m}$. The temperatures obtained from both methods A and B are affected by less than 0.5% by self-heating of the normal metal down to a temperature of 1 mK. In addition, we can evaluate at low temperatures (i.e. $T_N \leq T_S \ll \Delta/k_B$) the maximum cooling at optimum bias voltage $V_{\text{opt}} \approx (\Delta - 0.66k_B T_N)/e$ [60],

$$\dot{Q}_{\text{NIS}}^N(V_{\text{opt}}) \approx \frac{\Delta^2}{e^2 R_T} \left[-0.59 \left(\frac{k_B T_N}{\Delta} \right)^{3/2} + \sqrt{\frac{2\pi k_B T_S}{\Delta}} \exp\left(-\frac{\Delta}{k_B T_S}\right) + \gamma \right] \quad (4.10)$$

to be 90 pW at $T_{\text{bath}} = 1 \text{ mK}$.

5 Sub-gap bound-states in normal metal-insulator-superconductor junctions

M. Palma¹, L. Casparis^{1,2}, C. P. Scheller¹, T. Patlatiuk¹, L. Chirolli³, D. Maradan⁴,
A. V. Feshchenko⁵, M. Meschke⁵, J. P. Pekola⁵ and D. M. Zumbühl¹

¹ *Department of Physics, University of Basel, CH-4056 Basel, Switzerland*

² *Center for Quantum Devices, Niels Bohr Institute, University of Copenhagen, 2100
Copenhagen, Denmark*

³ *IMDEA-Nanoscience, Calle de Faraday 9, E-28049 Madrid, Spain*

⁴ *Physikalisch-Technische Bundesanstalt (PTB), Bundesallee 100, 38116
Braunschweig, Germany*

⁵ *Low Temperature Laboratory, Aalto University, FI-00076 Aalto, Finland*

Abstract

We present the investigation of current steps appearing in the sub-gap region of the I-V characteristic of a NIS junction. The steps are manifestation of Andreev bound states enhanced by the disorder and geometry of the junction. Some of the steps show thermal broadening from 100 mK down to 4 mK, serving as primary thermometry. Numerical calculation captures the steps and the sub-gap conductance, which dependences on the disorder and on the geometry. Magnetic field characterization shows a minigap, which decreases in magnetic field.

This chapter is prepared for publication.

5.1 Introduction

Superconducting tunnel junctions are the building blocks for Josephson junctions and superconducting qubits [16], as well as many other applications, ranging from thermometry [42, 43] to on-chip refrigeration [60]. Defects in the junction are one of sources of decoherence in superconducting qubits [101–105]. Traditional tunnel barriers are obtained by thermal oxidation of the Al layer giving an amorphous AlO_x , however by growing single-crystal Al_2O_3 , it is possible to reduce two level systems present in the barrier [106]. An additional source of decoherence in superconducting qubits is due to quasiparticle poisoning [107], which could be reduced by using metallic quasiparticle traps [108], gap engineering [109, 110] or vortex states [111]. Low temperatures are important to be utilized in quantum computing, since the quasiparticle population is strongly suppressed at low temperatures.

A practical way to examine the quality of a superconducting tunnel junction is to investigate the quasiparticle leakage current in the sub-gap region, which can be phenomenologically taken into account by adding a finite broadening γ to the BCS density of states (DOS) [81]. γ , also known as Dynes parameter, is defined as the ratio of the normal state resistance R_N to the sub-gap resistance R_G and may serve as figure of merit for the quality of superconducting tunnel junctions. Various origins for the Dynes parameter have been identified, including high frequency noise and background radiation that lead to photon assisted tunneling [80], as well as coherent Andreev processes [82, 83].

In this Letter, we study normal metal-insulator-superconductor (NIS) tunnel junctions at low temperature [34] and in a high-frequency shielded setup [34]. we observe narrow current steps in the sub-gap region of the I-V characteristics, that are identified with localized bound states. The sub-gap steps exhibit thermal broadening down to 4mK and may serve as precise primary on-chip thermometers. The steps show distinct evolution with in-plane magnetic field, scaling with the normal metal thickness. Furthermore,

their position in energy (bias voltage) is susceptible to thermal cycling, suggesting disorder and geometry as possible origin. We develop a model, which assumes impurities and disorder as origin of the steps. The model qualitatively agrees with the data and it reproduces a linear leakage current associated with the impurity landscape and the geometry of the junction. Such a finding could add some additional insight on the origin of the Dynes parameter for tunnel junctions measured in well shielded and filtered setup [31, 32, 43]. Furthermore, the model predicts the occurrence of a minigap related to the geometry of the junction that closes with the applied field.

5.2 NIS Device and Setup

The devices consist of two rectangular 40 nm thick Aluminum slabs with triangular tip pointing towards each other; see Fig.1(a). After in-situ thermal oxidation, the sample is overgrown with a 20 nm, 50 nm, or 150 nm thick Cu layer of the same geometry but under different tilt angles (shadow mask evaporation [43, 92]). This leads to the formation of a central resistive tunnel junction of area $380 \times 400 \text{ nm}^2$, and two outer low resistance tunnel junctions of macroscopic size (1.25 mm^2). Roughly half of the samples studied here are additionally equipped with a 50 nm thick gold ground-plane to shunt high frequency noise, which is separated by a 100 nm AlO_x barrier [80] from the rest of the device, see Fig.1(b).

The experiments are performed in two different dilution refrigerators with a base temperatures of about 9 mK and 5 mK, respectively. One of these dilution refrigerators is equipped with a parallel network of nuclear refrigerators (NRs), which employs magnetic cooling to reach roughly $T_{\text{Cu}} \sim 1 \text{ mK}$ in the Cu nuclear refrigerant. The cooling scheme relies on the standard adiabatic nuclear demagnetization technique, which was adapted for direct cooling of nanostructures [31, 32]. The performance of the Cu NRs was extensively studied in previous works [31, 32], allowing us to precisely estimate the electronic temperature of the NRs after each demagnetization for a given final B -field.

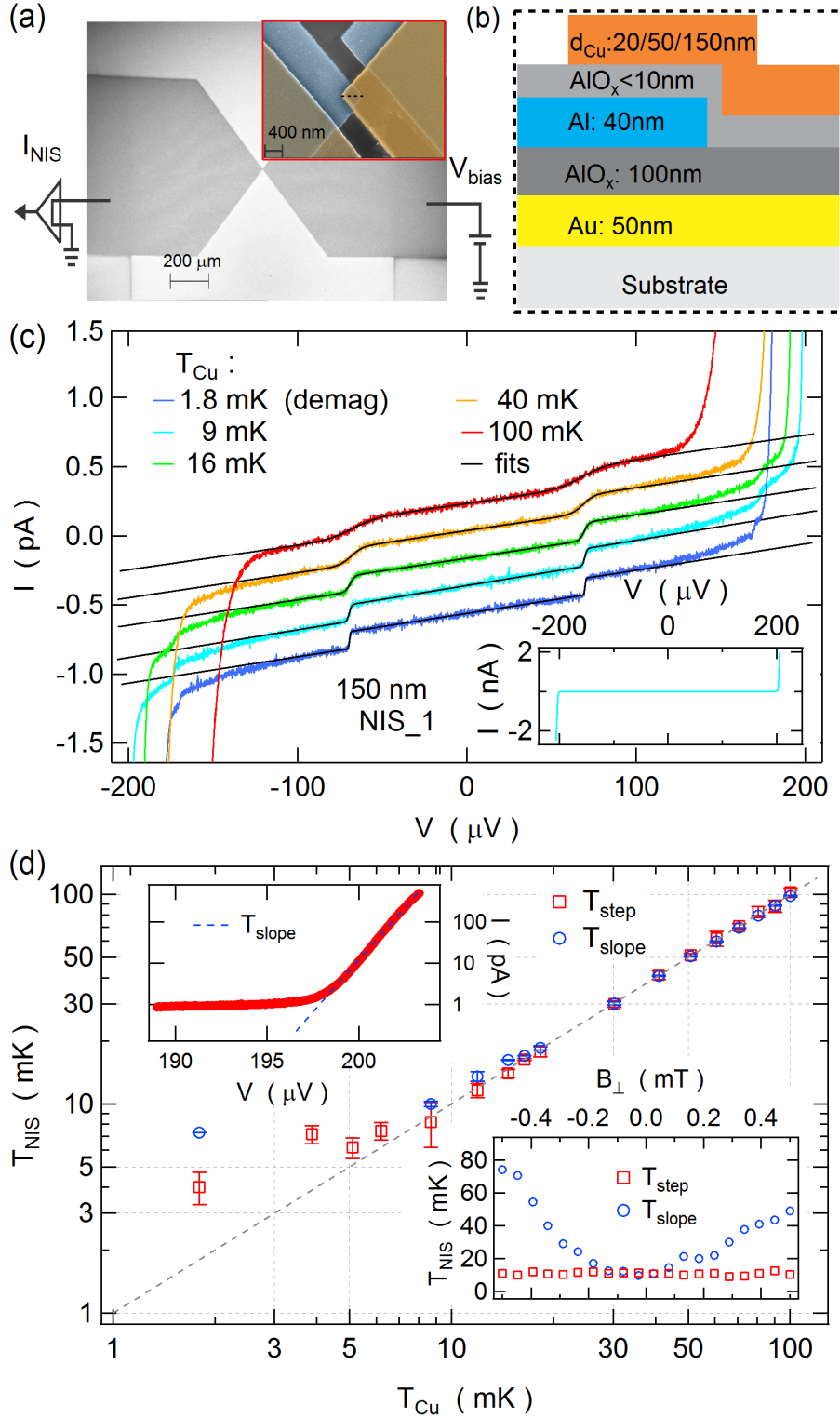


Figure 5.1: (a) Scanning electron micrograph of a co-fabricated NIS junction together with a schematic of the experimental setup. The inset shows a zoom-in of the junction. (b) A cross section of the NIS junction. (c) Zooms of the I-V curves in the sub-gap region for various temperatures. The black line indicates the double Fermi function fits used to extract T_{step} . To reduce the error on T_{step} the fit is performed on 10 consecutive I-V curves taken at the same temperature and we use the mean value as $\langle T_{\text{step}} \rangle$ and its standard deviation as error bar. The I-V characteristic for large current range is shown in the lower inset of Fig.1.(c). (d) T_{step} and T_{slope} as a function of T_{Cu} . The upper inset shows the region of the I-V curve where the semi-logarithmic fit is applied. The lower inset shows T_{step} and T_{slope} as a function of perpendicular magnetic fields.

5.3 Temperature and Thickness Dependence

In order to observe the sub-gap current steps we need to zoom-in the typical I-V characteristic, see inset of Fig. 5.1.(c), into the sub-gap region. We observe steps of roughly hundreds of fA, which are anti-symmetric in voltage bias. To characterize the steps, we first analyze their temperature dependence. We observe that the broadening of the steps increases together with the temperature, see Fig. 5.1.(c). Note that for higher temperatures, it becomes more difficult to identify the steps, since they become broadened and the sub-gap region shrinks for high temperatures.

To quantitatively analyze the data we fit a double Fermi function on top of a linear slope to account for γ and we find that the position and the amplitude of the steps as well as γ , i.e. the sub-gap leakage current, remain constant for different temperatures. Thus, we fixed these parameters and leave the broadening (δV) as the only fit parameter. Since the junction resistance in the sub-gap region is much larger than any series resistance from the leads, all the voltage drops across the junction. Therefore, we convert δV directly to temperature $e\delta V = k_B T_{\text{step}}$, where e is the elementary charge and k_B the Boltzmann constant. Indeed, we find that T_{step} agrees well with T_{Cu} in the temperature range between 9 mK and 100 mK, see red squares in Fig. 5.1.(d). Since no calibration is needed the steps can serve as a primary thermometer.

To verify the correct temperature reading of T_{step} , we compare it to another primary on-chip thermometer available on the same device. Close to the superconducting gap the current rises exponentially with inverse temperature $1/T$, $I \sim \exp(eV/k_B T)$ [43, 79], allowing us to extract the electronic temperature (T_{slope}) [43] from a linear fit to $\log(I)$, see upper inset of Fig. 5.1.(d). Indeed, T_{slope} agrees well with T_{step} in the temperatures range between 9 mK and 100 mK. After demagnetizing the Cu refrigerant cools down to $T_{\text{Cu}} \sim 1$ mK, T_{slope} saturates at 7.5 mK while T_{step} reaches 4.0 ± 0.7 mK, see supplementary material. This temperature is significantly lower compared to the previous NIS thermometers [42, 43] and it is close to the lowest temperature so far

measured in a solid state device [40].

Furthermore, T_{slope} is extremely susceptible to perpendicular magnetic fields (B_{\perp}), even on the scale of 1 G. Therefore, the temperature reading is correct only around $B_{\perp} = 0$. As soon as the magnetic field is increased, the thermometer spuriously reads higher temperatures, see lower inset of Fig. 5.1.(d). In contrast, T_{step} remains constant while sweeping the perpendicular magnetic field, showing that T_{step} is more robust against B_{\perp} .

In order to shed more light on the origin of the steps, we study their behavior upon thermal cycling. For each cycle the samples are cooled from room temperature down to base temperature of the cryostat. We observe a random movement of the energy positions for various cycles. Fig. 5.2.(a) shows the I-V curves of the device NIS_2 for four different cycles, which are indicated by shades of grey. This particular device features three separated discrete steps, two of them are stationary upon thermal cycling, while the lowest energy one changes significantly, see inset of Fig 5.2.(a).

Next, we characterize the steps as a function of the thickness of the Copper layer (d_{Cu}) in order to gain more insight about their origin. We measured several devices with Cu thickness of 20 nm, 50 nm and 150 nm. For all junctions investigated here, the steps are observed as shown in the I-V curves of Fig. 5.2.(b-d), appearing at random bias voltages. We note that the amplitude varies over one order of magnitude from few hundreds of fA up to pA regime, indicating no correlation between the amplitude of the steps at finite bias and d_{Cu} . Fig. 5.2.(b) shows two I-V curves for $d_{\text{Cu}} = 20$ nm, in addition to small steps close to the gap edge, there is a very pronounced zero bias step (ZBS). Such kind of step is weakly present in the devices with $d_{\text{Cu}} = 50$ nm, see Fig. 5.2.(c), in contrast this is completely absent for the devices with 150 nm of Cu layer, see Fig. 5.2.(d). The amplitude of the ZBS as a function of d_{Cu} is shown in the lower panel of Fig. 5.2.(e).

Furthermore, we notice that γ shows a thickness dependence, γ decreases as d_{Cu} is increased, see upper inset of Fig. 5.2.(e). Additionally, we observe that γ stays un-

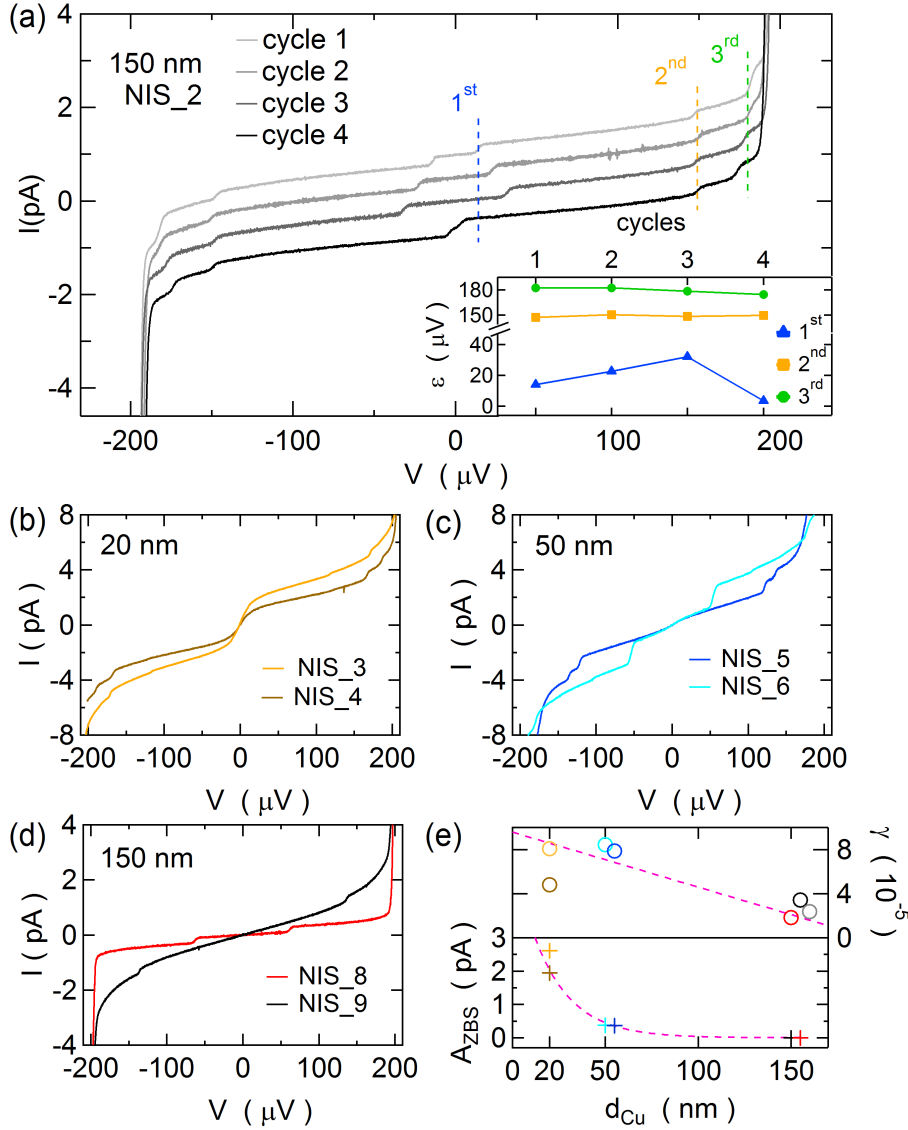


Figure 5.2: (a) I-V curves of the NIS_2 for various thermal cycles. (b-d) I-V curves for two different devices at Cu thickness of 20 nm, 50 nm and 150 nm, respectively. (e) the upper graph shows the Dynes parameter as a function of d_{Cu} and the lower graph shows the amplitude of the ZBS as a function of Cu thickness. Note that for both graphs the points at 50 nm and 150 nm are horizontally offset by 5 nm to avoid the overlap of the markers.

changed for devices with or without back-plane, see NIS_5 and NIS_6 in Fig. 5.2.(c) respectively, indicating that high-frequency radiation can be excluded as origin of γ in our setups.

5.4 In-plane Magnetic Field

In the last experimental section of this letter, we investigate the magnetic field dependence of both, zero bias and finite bias steps (FBSs). The in-plane magnetic field dependence of the steps is presented in Fig. 5.3.(a-d), which show the color-plots of the logarithm of the absolute value of the differential conductance G as a function of the voltage bias and B_{\parallel} for devices with different thicknesses. The measurements are performed in a cryostat equipped with a two-axis vector magnet with one component in the plane of the junction (B_{\parallel}) and the second component perpendicular to the plane of the junction (B_{\perp}). The B_{\perp} is used to dynamically compensate out of plane components, which arise due to sample misalignment.

We first analyze ZBS and then we turn our attention to the FBSs. Fig. 5.3.(a) shows that the ZBS gradually disappears as the B_{\parallel} moves away from zero, it completely dies out for $B_{\parallel} > 130$ mT while the superconducting gap closes at roughly $B_{\parallel} = 500$ mT. The amplitude and the width of the ZBS are shown in Fig. 5.3(f), which clearly shows that the amplitude decreases while the width grows as B_{\parallel} moves away from zero. The ZBS shows the same behavior also in the devices with $d_{Cu} = 50$ nm, but in this case the ZBS is suppressed already at 60 mT, see Fig. 5.3(b-c).

Overall the FBSs show a parabolic dependence as a function of B_{\parallel} . Beside to this dependence we observe Zeeman splitting given by $2g_e\mu_B B_{\parallel}$, where $g_e = 2$ is the electron g -factor and μ_B is the Bohr magneton, see Fig. 5.3.(b-d). However, for the device with $d_{Cu} = 20$ nm the FBS shows a linear dependence as a function of B_{\parallel} , indicating the presence of only Zeeman splitting without parabolic dependence, see Fig 5.3.(a). To quantitatively analyze the parabolic trajectories of the FBS, we plot the curvature of each trajectory as a function of the thickness and we observe that the curvature seems

to decrease together with thickness, see Fig. 5.3.(e).

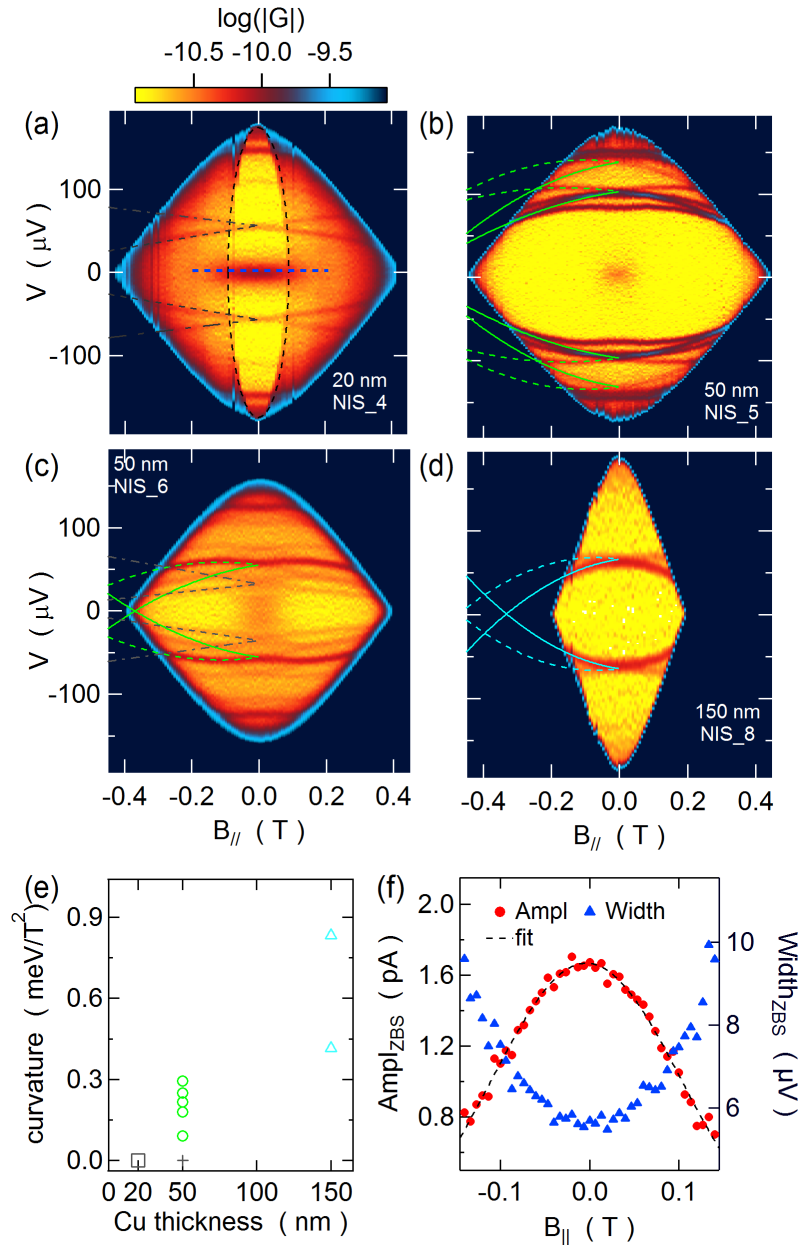


Figure 5.3: (a-d) The logarithm of the absolute of the differential conductance as a function of the in plane magnetic field and voltage bias for various thicknesses of Cu. The full colour lines in (a-d) indicate the parabolic trajectories describe by the steps in $B_{||}$, they are shifted from the dashed lines by the Zeeman energy. (e) the thickness dependence of the curvature of the steps in-plane magnetic field. The amplitude and the width of ZBS as a function of in-plane field are shown in (f). The black dashed line is a Gaussian fit of the Ampl_{ZBS} as a function of $B_{||}$

5.5 Discussion and Model

Some of these steps are weakly coupled to the leads and exhibits a temperature dependence down to 4 mK, although others saturated at higher temperatures. The ZBS exhibits a temperature dependence, however the temperature extracted by fitting to ZBS a Fermi function is systematically higher than T_{Cu} up to 150 mK. The deviation between the two temperatures is reduced for higher T_{Cu} and they agree for temperatures above 150 mK. In addition, the ZBSs are independent from the thermal cycling while the position of FBS randomly change for each thermal cycle, giving evidences that the impurities might be the origin of the steps. It seems clear that the FBS are due to impurities located in the superconductor, insulator or in the normal metal close to the junction.

We exclude impurities hosted in the superconductor, since they need to pin vortices to show features in transport experiments. Vortices appear only when an orthogonal external magnetic field is applied to the superconductor, however the steps are always present regardless which B_{\perp} is applied as long as the gap is not closed, see supplementary chapter for the measurements in B_{\perp} . Thus, we reject the vortices as possible origin for our sub-gap steps.

We perform extensive numerical calculations to simulate the device behavior⁷. The model assumes a uniform distribution of disorder and a geometry that aims to model the section of the junction. Carriers can be Andreev reflected at the NS interface, that is a rare process due the low transparency of the barrier of the junction in use, see upper inset of Fig. 5.4. In addition, the carriers can be normal reflected at the sample edges or at the barrier.

The interplay between disorder and the geometry produces many unresolvable small steps in the I-V curve, that result in a linear slope in the sub gap region. For a linear geometry the conductance decreases upon increasing the disorder strength. Numerically,

⁷P. San-Jose, www.icmm.csic.es/sanjose/MathQ/MathQ.html

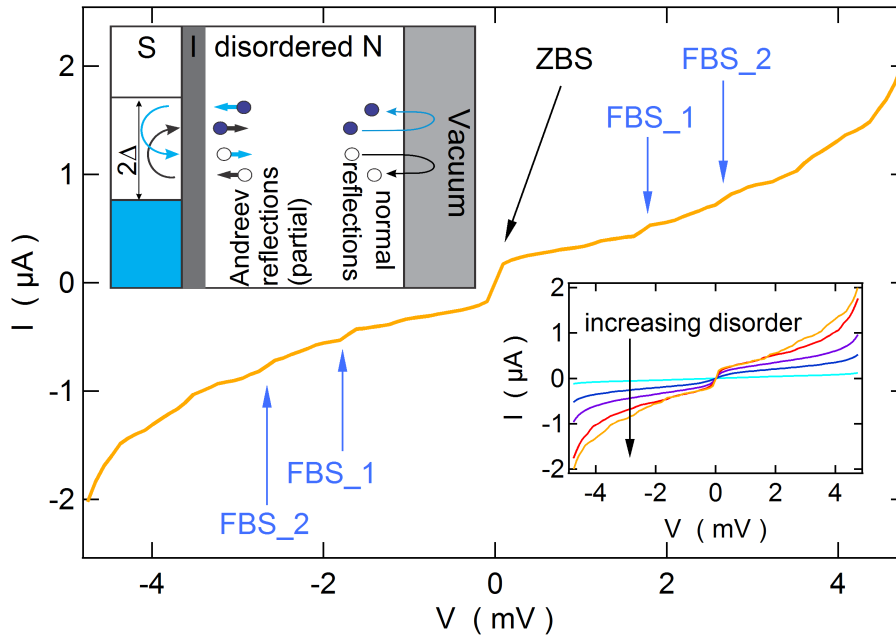


Figure 5.4: (a) Simulation of the I-V curve. The upper inset shows Energy diagram of the NIS junction. Showing Andreev reflections (light blue arrows) at NIS interface and normal reflections (black arrow) at the edge of the normal metal. The lower inset shows simulated I-V curve for different disorder strengths

we observe that the background conductance increases with disorder in the tunneling regime, see lower inset of Fig. 5.4. This is understood as two-particle tunneling enhanced by interference effects taking place on a scale on order of the superconducting coherence length scales, that are strongly amplified by the geometry of the junction [112]. The resulting background conductance has a different origin with respect to a Dynes broadening, in that the latter is due to a finite DOS in the superconductor, that allows single particle tunneling through it.

Reducing the thickness of the normal metal layer a carrier has higher probability to be Andreev reflected, since the carriers hit the NIS interface more frequently compared to the thicker layer. The coherent interference of all the possible carriers paths, where carriers bounce many times without losing phase coherence, gives rise to geometric resonances. Energetically speaking, the geometric resonances produce a discrete energy spectrum, allowing quasi bound states below the gap that give rise to sharp peaks in the differential conductance of the junction, which result in FBS in the I-V characteristic,

in agreement with the data, see Fig. 5.4. In a small clean system we observe that, beside relatively sharp peaks at finite energy, a broad peak occurs at zero energy. Disorder amplifies the heights of the peaks and reduces the width of the ZBP. The coherent interference between the carriers backscattered toward the NIS interface in the diffusive regime gives rise to reflectionless tunneling [113–115]. It is predicted that ZBS is progressively reduced until it disappears for fields higher than the critical field $B_c = \Phi_0/(W \cdot L)$, where Φ_0 is the flux quantum, W and L the dimensions of the junction [116, 117]. The estimated values of B_c for different thicknesses of Cu agree well with the values obtained in the experimental data.

As shown in Fig. 3 the FBSs show a parabolic trajectory in B_{\parallel} , which could be explained in the framework of our model as a bending of the trajectories of the electron due to the Lorentz force. To verify such a hypothesis we need to compare d_{Cu} with the cyclotron radius $r_c = mv_f/(e \cdot B_{\parallel})$, where the m is the bare electron mass and v_f is the Fermi velocity. For Cu we estimate $r_c \sim 18 \mu\text{m}$, thus $r_c \gg d_{cu}$ indicating that the orbital effect should be negligible.

The orbital magnetic field is introduced in the simulation by Peierls substitution for a given disorder realization. The energy position of the peaks evolves in a complicated way, whereby the peak positions oscillate and cross, giving rise to a intricate evolution that is qualitatively similar to the 50 nm thick junctions NIS_5 for magnetic fields two orders of magnitude larger than the experimental ones. The discrepancy in the field scale could be attributed to quantum effects in the disorder metal in the quasi ballistic regime [118].

Additionally, the simulation shows that the conductance versus energy and magnetic field shows regions of different background conductance, that strongly resemble the "evil eye" of NIS_4. We interpret the evil eye as a minigap [119–123] that opens in the junction area and closes with the field. The value of the minigap in a linear diffusive junction is on order of the Thouless energy. For the geometry under consideration the minigap at $B_{\parallel} = 0$ is the gap itself and it closes linearly with the field. For the thicker

junctions, 50 and 150 nm, that bright diamond can be interpreted as a minigap itself, whereas for the 20 nm junction we observe two minigaps that close with a different slope with the applied B_{\parallel} .

5.6 Conclusion

In conclusion, we observe current steps in the sub-gap region of the I-V characteristic, given by Andreev bound states enhanced by the disorder and the geometry of the junction. The FBSs show thermal broadening down to 4 mK, serving as primary thermometer. Furthermore, we observe a ZBS that is explained by the reflectionless tunneling theory and its B_{\parallel} dependence agrees well with theory. The numerical simulation capture the FBSs, the ZBS and the sub-gap conductance, which is interpreted as two-particle tunneling current given by interference effects amplified by disorder and the geometry of the junction. Additionally, we find evidence for minigap feature due to the geometry of the junction, which is suppressed by the magnetic field.

5.7 Supplementary material

5.7.1 Current Steps in Differential Conductance

In this section, we focus on the differential conductance G of the experimental traces, obtained by numerical differentiation of the measured I-V curves. The derivative of a step is a symmetric peak centered in voltage bias around the position (inflection point) of the step, see Fig. 5.5.(a-c). From now on, we refer in the text to peaks instead of current steps, since the supplementary material is presented in terms of differential conductance G .

Symmetric peaks are observed e.g. in Josephson junctions [79, 124], i.e. superconductor-insulator-superconductor junction, when microwave radiation is applied to the junction. Those are named Shapiro steps [125, 126] and are a direct consequence of the AC Josephson effect. We can exclude Shapiro steps as possible

origin for the current steps, since they appear periodically at voltages $V_n = hf/2e$ while the peaks presented in this work are randomly distributed in voltage bias.

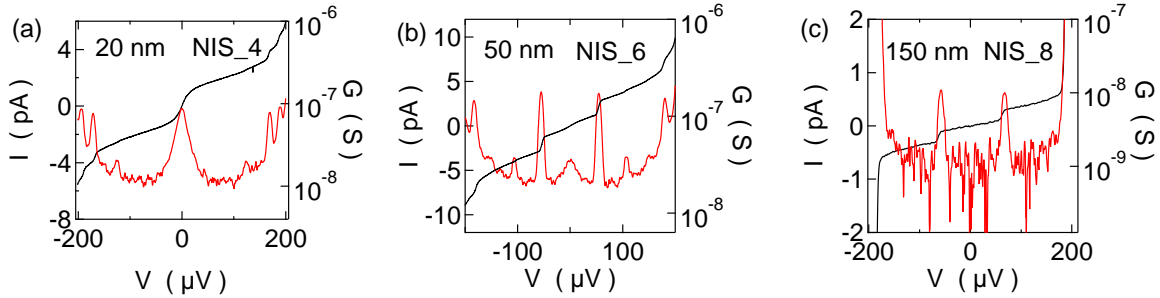


Figure 5.5: (a-c) I-V curves and the differential conductance G for NIS_4, NIS_6 and NIS_8. The steps observed in the I-V characteristic are transformed in symmetric peaks in the differential conductance.

5.7.2 Numerical Simulation

In the experiment we have three different junctions, characterized mainly by the thickness of the Cu layer. The geometry of the devices consists on a normal lead placed in proximity with a superconducting lead, in a way that on an area of 400 nm the two leads overlap. The overlapping region constitutes the NIS junction. Although the experimental device is three-dimensional, we simulate the system by focusing on the two-dimensional section, as shown in Fig. 5.6. The system is composed by a central region that mimics the actual geometry of the NIS junction. Attached to the central region there are a normal lead on the left side and a superconducting lead on the right side. Part of the central device is superconducting (red spots), to better model the NIS geometry. In every site of the central region there is an impurity, that is schematically represented by a white spot in Fig. 5.6.

The system is modeled by a tight-binding square lattice and impurities are inserted as a local on-site random energy shift of strength comprised between $-U$ and U . The simulations are performed with a Mathematica Package developed by Pablo San-Jose⁸

⁸P. San-Jose, <http://www.icmm.csic.es/sanjose/MathQ/MathQ.html>.

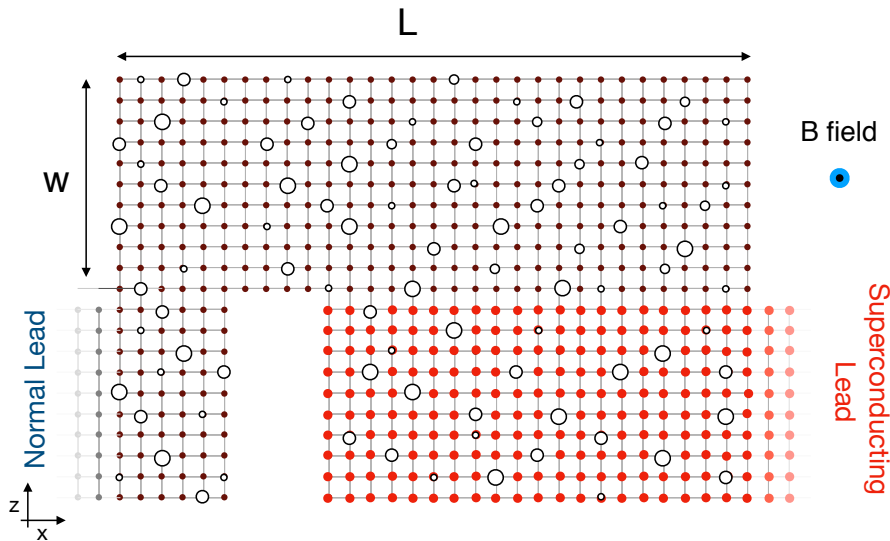


Figure 5.6: Devices simulated: The system is composed by a square lattice, on the left side we have the normal lead, that is represented by shaded spots that fade away from the device. Analogously, on the right side we have the superconducting lead, that is represented by red spots. The central region comprises also part of the superconducting lead. Impurities are modelled as a local shift of energy and are represented by some indicative white spot, whose size mimics the impurity strength.

We start the analysis by first addressing the conductance of the device as a function of the strength of the disorder U . We simulate a device with thickness $W = 100$ sites, $L = 200$ sites and with leads of thickness of 100 sites. Fixing a hopping parameter $t_0 = 1$ eV, a Fermi energy on order of $E_F = 2.25$ eV, and assuming bare electron mass, the lattice parameter is on order of the Angstrom, so that we simulate a relatively thin device $d_{Cu} = 10$ nm. We assume that the superconducting part in the central region (red in Fig. 5.6) is connected to the normal region by a hopping $t_1 = 0.015 t_0$, so to simulate a resistive barrier, and we choose the superconducting gap to be $\Delta = 0.005 t_0$.

In order to obtain a sample independent characterization of the device, we average over many disorder configurations, keeping fixed the strength of the disorder. This is a standard procedure that not only provides device-independent information of the system behavior, but it also better models a single device characterized by a disorder that changes on a scale of the device size.

In Fig. 5.7.(a) we plot the conductance of the device, each curve corresponding to a

different impurity potential strength $U/t_0 = 0, 0.3, 0.6, 0.9, 1.2$. We see that upon increasing the strength U the conductance starts to show a background finite value, that can be seen as composed of many resonances at all energies. The associated I-V characteristics is shown in Fig. 5.7.(b). We see that it acquires a finite slope due to the disorder induced background conductance. This behavior is contrary to the expectation of a NS junction with an ordinary linear geometry. In that case, upon increasing the disorder the conductance decreases. Such behavior is due to coherent two-particle tunneling, which dominates in the tunneling limit considered and it is strongly affected by geometrically enhanced interference effects taking place on a length scale of roughly the coherence length. It is worth to point out that it is completely different from a finite DOS in the superconductor modeled by a Dynes parameter.

Beside the background finite value, every curve presents a zero bias conductance peak, that is due to reflectionless tunneling [114, 115]. At small energy Andreev reflection is perfect for a transparent barrier and the phase i determines full current through the junction, regardless of the disorder configuration. Upon reducing the transparency of the barrier the conductance is depressed at finite energy and survives at zero energy in the form of a peak. The width of the peak does not depend on the strength of the disorder, but the height of the peak increases with disorder. The particular geometry enhances the Andreev reflections due to the back wall of junction, that reflects particles and let them collide many time onto the superconductor, where they are occasionally Andreev reflected. Regardless of the low rate of Andreev reflection at each collision due to the low transparency of the barrier, coherent sum over many path makes the Andreev reflection at zero bias particularly efficient.

Finally, we notice that well defined conductance peaks at finite energies appear upon increasing the disorder strength. Remarkably, the peaks survive disorder average. This is a very important result, stating that the origin of these resonances is related to the geometry of the system and it is strongly enhanced by disorder. Although every disorder realization presents a randomly distributed series of resonance, the averaged

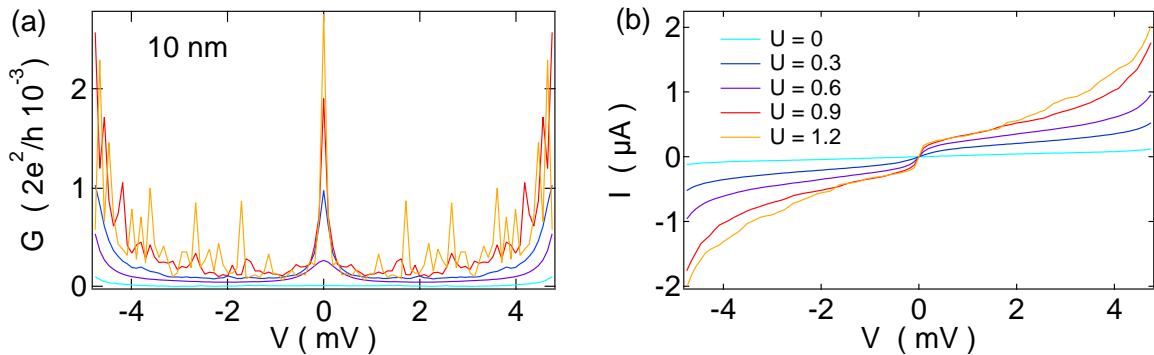


Figure 5.7: (a) Conductance as a function of the voltage bias and (b) I-V characteristics of a 10 nm thick NIS junction with the geometry of Fig. 5.6 for several values of the disorder strength $U/t_0 = 0.0, 0.3, 0.6, 0.9, 1.2$. and the conductance has been averaged over 100 configuration for each voltage V . The device has $W = 100$, $L = 200$, $t_0 = 1$ eV, $t_1 = 0.015 t_0$, $\Delta = 0.005 t_0$.

conductance makes manifest the underlying geometric origin of the resonances.

In the regime we are considering the bare coherence length of the superconductor is on the order of 200 lattice sites, that is on order of the linear sizes of the system, and interference effects in the two-particle coherent tunneling can be strongly enhanced by the geometry. The occurrence of a peak is consistent with a quasi-ballistic picture, in which the mean free path $\ell_{\text{m.f.}}$ is at on order of the length W . The latter can be estimated for a linear geometry by the Drude weight [114] $G_N = (2e^2/h)\pi N\ell_{\text{m.f.}}/2\tilde{L}$ and for about $N = 50$ number of propagating modes, taking as the linear size the geometric mean $\tilde{L} = \sqrt{LW}$ and calculating the average zero-energy conductance in the normal case with $t_1 = t_0$ and $U = 1.2 t_0$ we find $\ell_{\text{m.f.}} \sim 5 - 10$ lattice sites, that is an order of magnitude smaller than W . In a linear geometry such a ratio between the mean-free path and W would imply a diffusive/quasi-ballistic regime. We then conclude that the geometry of the system enhances coherence effect and that the correct regime is quasi ballistic.

The back wall of the junction reflects particles towards the interface with the superconductor and a quasi bound state occurs, in which a particle bounces many times between the corners of the normal region and the superconductor, experiencing both normal and Andreev reflection. Weak disorder randomizes the momentum at every

scattering event, so that it connects bound states that form in the junction to the scattering channels. For the strong disorder case the mechanism at the basis of finite energy peaks is similar to the reflectionless tunneling characterizing the zero bias peak. When normal reflection dominates, due to the low transparencies of the barrier, resonances occur also at finite energy thanks to the peculiar geometry. The energy of the resonance is inversely proportional to the path length of the bound state, that in turn is upper bounded by the width W . However, disorder randomizes the motion and resonances can occur at any energy in the gap.

5.7.3 Magnetic Field Dependence

We now study the magnetic field dependence of the resonances. We assign a given disorder configuration with strength $U = 0.9 t_0$ and we do not average over disorder. We assume $t_0 = 1$ eV, $\mu = -2.25$ eV, $t_1 = 0.015 t_0$, and $\Delta = 0.005 t_0$. We fix the sample size to $W = 200$ sites and $L = 400$ sites. In order to amplify the effect of the magnetic field we assume a lattice parameter $a \simeq 5$ Å and a large g -factor $g^*/g = m_0/m^* \simeq 27.6$. Although these number do not provide a good description of a metal, they allow us to study the putative effect of a magnetic field and to check the results with the experiment. The magnetic field is applied in the plane of the junction, that is orthogonal to the lattice in the simulation.

The results of the simulations are shown in Fig. 5.8.(a), where we show the conductance versus the applied field B and the energy ϵ , together with the $\log(G)$ in ig. 5.8.(b) and the $\log(G)$ after a cutoff for $G > 0.07$ is applied in ig. 5.8.(c). The resulting Zeeman splitting for 0.5 T is on the order of 0.0008 eV, so that Figs. 5.8 are almost entirely dominated by orbital effect. Two features clearly appear: i) the resonances move with the magnetic field and their trajectories depart from the Zeeman induced linear splitting, ii) the background conductance changes as a function of the B -field and produces three different regions.

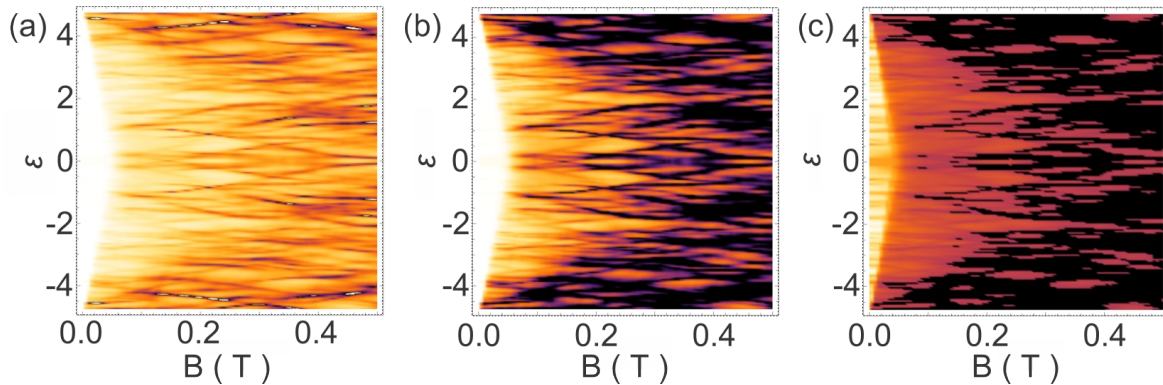


Figure 5.8: (a) Color plot of the conductance as a function of the magnetic field B (abscissa) and the energy ϵ (ordinata). (b) Color plot of $\log G$, and (c) color plot of $\log G$ with a cutoff for values $G > 0.07$. Parameters of the simulations are $t_0 = 1$ eV, $\mu = -2.25 t_0$, $\Delta = 0.005 t_0$, $t_1 = 0.015 t_0$, $g^*/g = 27.6$, $a \simeq 5$ Å.

5.7.4 Resonances versus B -field

The resonances clearly acquire a dependence from the orbital magnetic field. The evolution is quite complicated but a common feature can be seen: the peaks position oscillates with the magnetic field. This pattern is visible for every resonance and the evolution is the result of several crossings of the different resonances. The oscillation and crossing may result in a diverging or a converging resonance as a function of the applied field. For small B the resonances show a very tiny dependence on the applied field, as it is visible in Fig. 5.8 c). In order to further understand the dependence on the magnetic field we simulate a much smaller device with a slightly different geometry (see Fig. 5.9.(c)). We see that the finite-bias peak for the case $U = 0.8 t_0$ bend towards zero energy (Fig. 5.9.(b)). The values of the magnetic field are very high, whereby $2\pi\Phi/\Phi_0 = ea^2B/\hbar$ is the Peierls phase associated to the orbital magnetic field.

In Fig. 5.9.(d-e) we also plot the scattering states of two given transport channel in the cases $U = 0$ and $U = 0.8 t_0$, both for the ZBP and the FBP. The clean case shows how bound states develop in the junction region, confirming the geometric origin of the resonances. In the disordered case we see that the motion becomes highly irregular, but the comparison between the ZBP and the FBP confirms the common origin of the effect.

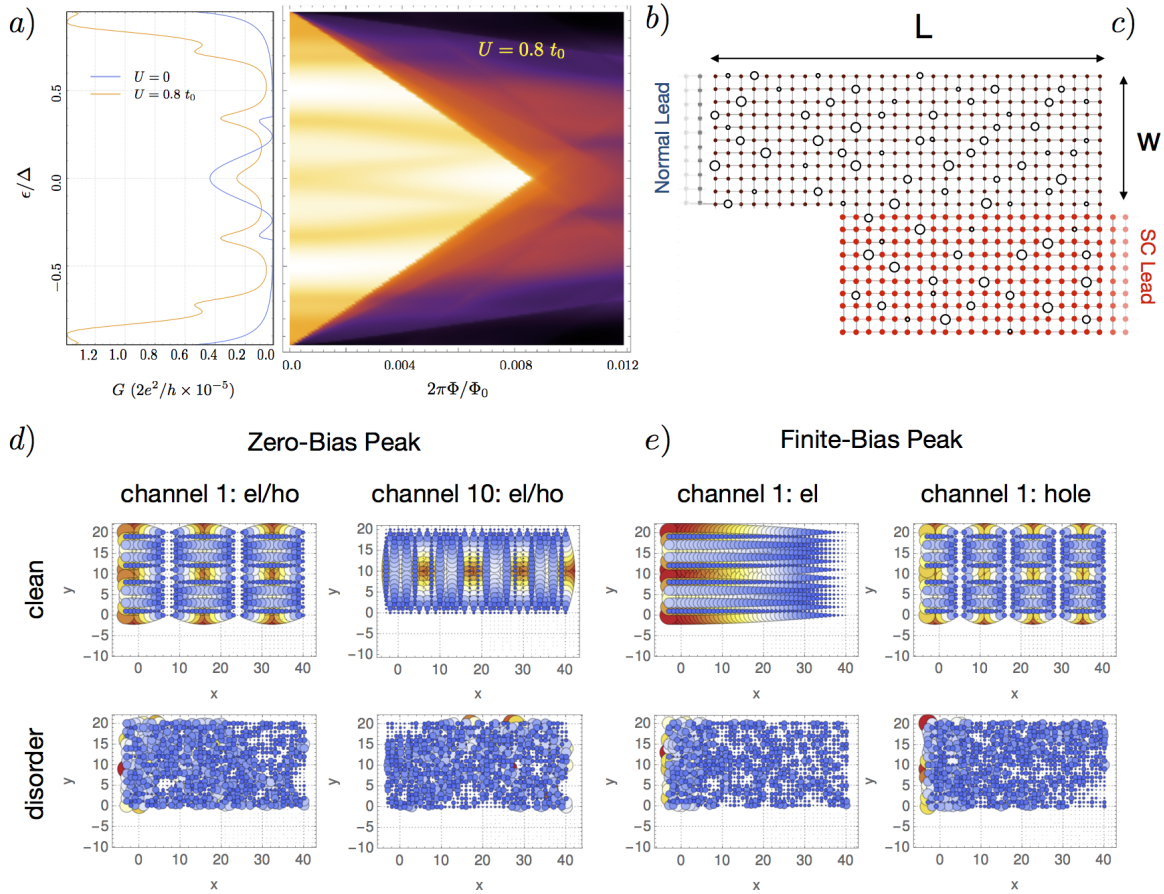


Figure 5.9: Study of the conductance for a slightly different geometry: $W = 20$ and $L = 40$ lattice sites. a) Conductance for two different values of $U/t_0 = 0, 0.8$. b) Color plot of the conductance as a function of the magnetic field B (abscissa) and the energy ϵ (ordinata) for the case $U = 0.8 t_0$. c) Device geometry. d) Scattering states of the ZBP for the $U = 0$ and $U = 0.8 t_0$ for two significant scattering channels. e) Scattering states of the FBP for a given scattering channel. The device is characterized by the following parameters: $t_0 = 1$ eV, $\mu = -2.25 t_0$, $\Delta = 0.1 t_0$, $t_1 = 0.01 t_0$, $g^* = 0$.

5.7.5 Background Conductance and Minigap

The background conductance as a function of the energy and the magnetic field shows two regions of different background value: very bright, bright, and slightly dark in Figs. 5.8. The first region is approximately comprised in the region $|\epsilon|/\Delta < 1 - \epsilon|B|/B_1^*$, with $B_1^* \sim 0.07$ T, and the second region approximately comprised in the region $|\epsilon|/\Delta < 1 - \epsilon|B|/B_2^*$, with $B_2^* \sim 0.5$ T. We interpret these two regions as two different minigap at finite field. Theoretical models predicts that the minigap in large junctions is on order of the Thouless energy and that the orbital magnetic field closes the minigap in a

dirty junction [112, 119–123, 127–129]. Here we observe a gap on order of Δ at $B = 0$ and two different values that detach from $\epsilon = \Delta$ and close with different slope with B . To our knowledge such a behavior has been never observed, nor theoretically predicted. Our numerical results show that the background conductance in a highly disordered NIS junction can develop regions in the plane (ϵ, B) characterized by different background DOS that close with the applied orbital B field with a law that approximately previous theoretical predictions for a minigap in a diffusive junction [119, 120]. We ascribe these features to the geometry under consideration.

5.7.6 Photon Absorption

Photon absorption processes in NIS junctions produce peaks in conductance. To exclude this process as possible origin of the sub-gap feature, we perform RF measurements. The RF setup comprises of a coaxial cable, connected to a free-standing few-turn coil surrounding the samples. The RF measurements are performed on NIS_8, since the device has no ground plane, which would shunt filter the RF signal. The photon absorption produces copies of the gap peaks (single particle DOS for the superconductor), which we show in Fig. 5.10 by shifting copies (black and blue traces) of the original data (red curve) in order to overlay the absorption peak of the copy with the gap peak of the original data. The photon absorption peak, produced by the RF signal of frequency f , is shifted by a voltage $V_n = hf/e$ compared to the gap peak, see Fig. 5.11.(b).

Next, we compare the shape of the observed sub-gap features with the photon absorption peaks. The sub-gap peaks are symmetric around their bias positions, in contrast to the photon absorption peaks are asymmetric and being characterized by two different slopes around the maximum of the peak, see Fig. 5.11.(d). The different shape of the peak compared to the photon absorption peak indicates that they are due to different processes. To further investigate the origin of the sub-gap peaks, we probe their position as a function of applied RF power normalized to 1 mW $P[dbm]$ and at

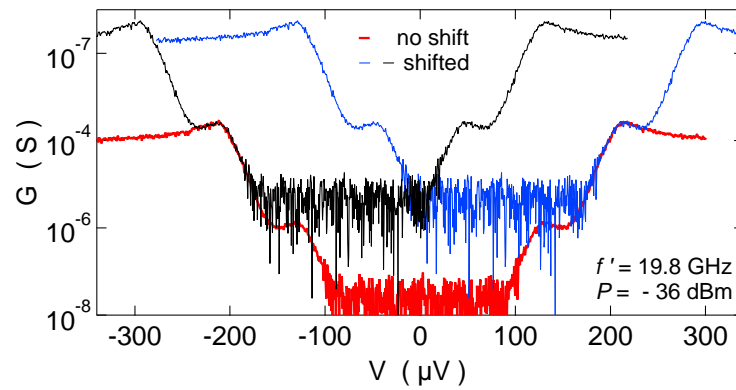


Figure 5.10: Logarithm of the absolute value of G as a function of the voltage bias for $P = -36$ dBm and $f' = 19.8$ GHz. The blue and the black traces are shifted copies of the original data (red trace).

frequency f . As shown in Fig. 5.11.(a). the position of the peaks (indicated by the red arrows) stays constant regardless of f and P , confirming that the sub-gap peaks are not due to photon absorption and they are independent from the RF radiation. Fig. 5.11.(e). shows multiphoton absorption for two different frequencies f and f' .

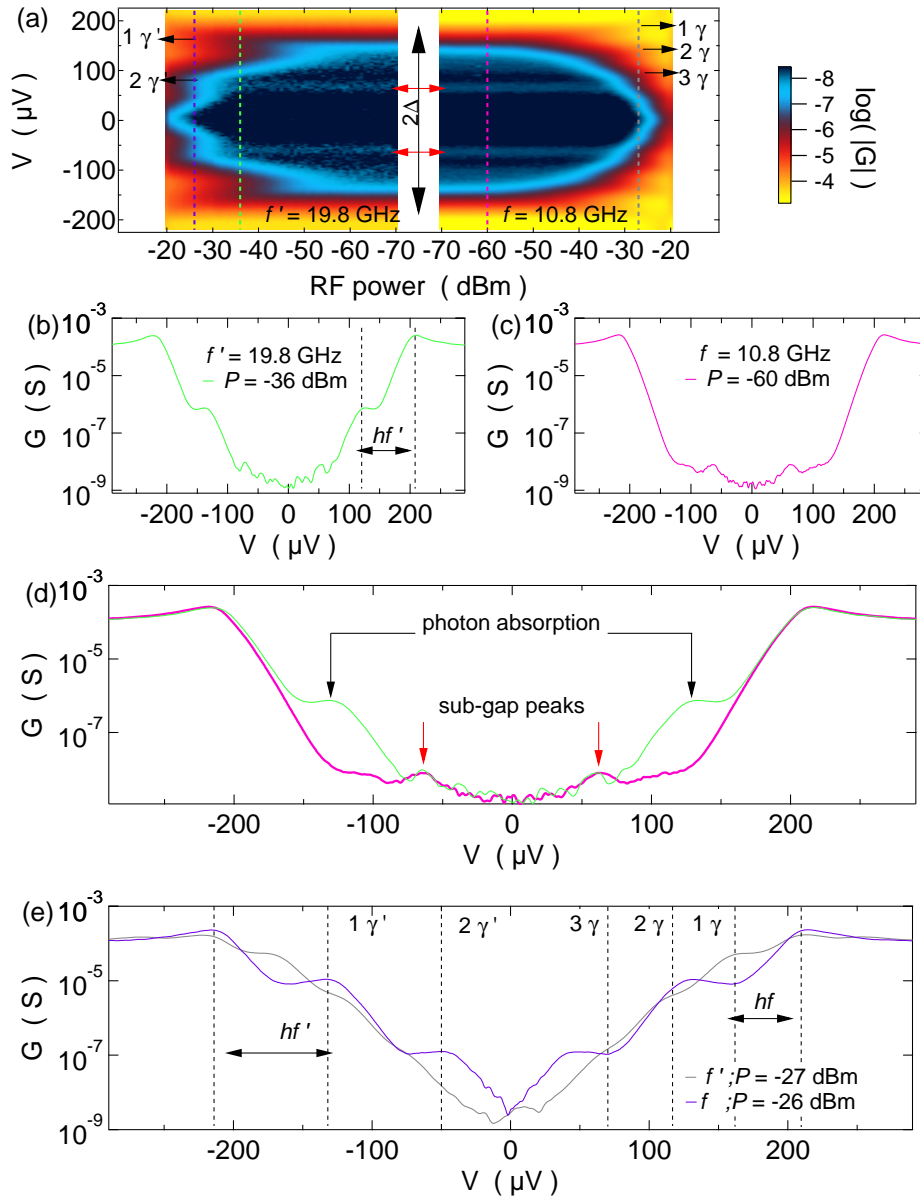


Figure 5.11: (a) Logarithm of the absolute value of G as a function of P and voltage bias for two different frequencies f and f' . Black arrows indicate the different multiphoton absorption processes. (b) A cut of the color plot shown in (a) for $P = -36$ dBm and $f' = 19.8$ GHz, where one photon is absorbed and it creates a replica of the gap peak shifted by $V_n = hf'/e$. The peaks are narrow features, thus we highlighted them by averaging many cuts at different powers without losing the main features. (c) The averaged cut at $P = -60$ dBm, where the peaks are clearly visible without photon absorption features. (d) Comparison between the cuts shown in (b) and (c), to point out the different shapes between sub-gap peaks and photon absorption peaks. (e) Logarithm of the absolute value of G , showing multiphoton absorption for the two different frequencies.

5.7.7 Perpendicular B-field

The main text shows the dependence of the ZBP and FBPs as a function of the B_{\parallel} , while here we present their dependence on the perpendicular magnetic field B_{\perp} . As shown in Fig. 5.12.(a-d), the zero bias peak is weakly reduced with increasing B_{\perp} . This is in agreement with the measurements in B_{\parallel} and the theory of the reflectionless tunneling, confirming that phase coherence interferences, responsible for the ZBP, are destroyed when an external field is applied. Figure 5.3 shows that the ZBP is already suppressed for B_{\parallel} higher than the critical field $B_c \sim 130$ mT, which is smaller than the B_{\parallel} needed to close the gap. In contrast, the ZBP is visible until the gap of the superconductor is completely closed at $B_{\perp} \sim 10$ mT, see Fig. 5.12.(a-d), because the junction area, affected by B_{\perp} is larger than the cross section to which B_{\parallel} is orthogonal. Panels (c) and (d) in Fig. 5.12 show that the FBPs move to higher energies with increasing B_{\perp} , in contrast to the case of B_{\parallel} . Additionally, the FBPs have a stronger dependence on B_{\perp} , showing changes of energies already at a few mT compared to the 100 mT needed in B_{\parallel} to observe changes of the energies. The different dependence of the FBPs for different field orientations is not yet understood.

The color plots in Fig. 5.12 show a faint zone (bright color) where the sub-gap conductance G_g is on the order of the normal state conductance and a well defined zone (dark color) where G_g is suddenly reduced by several orders of magnitude. These zones appear at different magnetic fields, which depend on the sweep directions. This dependence of the zones suggest entrance of vortices in the junction area, leading to a local suppression of the superconductivity in the faint region. In contrast when the vortices move out of the junction, the superconductivity is recovered, resulting in a reduction of G_g . This scenario is possible since it has been observed that a thin film of Al behaves as type II superconductor [79, 130, 131], allowing the presence of vortices in the superconducting layer. Additionally, Fig. 5.12 (a-d) show horizontal spikes, where G locally jumps at different values of B_{\perp} . The spikes might be due to the movement of vortices through the junction. The ZBP and the FBPs appear regardless of the spikes

and even at $B_{\perp} = 0$, indicating that vortices can be excluded as origin of the peaks.

In the main text we show that the temperature T_{slope} is not indicating anymore the right temperature reading once B_{\perp} is different from zero. To clarify this concept, we show in Figure 5.12.(e,f) the evolution of the gap as a function of B_{\perp} for a specific sweep direction and at base temperature of the fridge. The superconducting gap seem to be qualitative very different when approaching the gap at zero magnetic field region (I) and moving away from the zero magnetic field region (II). The gap edges evolve from a soft gap to a hard gap when B_{\perp} is reduced to zero, see Fig. 5.12.(f). Further reducing B_{\perp} the inflection points of the gap edge move towards the middle of the gap. We conclude that the gap edges are strongly modified by B_{\perp} and they are not anymore only a function of the temperature and voltage bias.

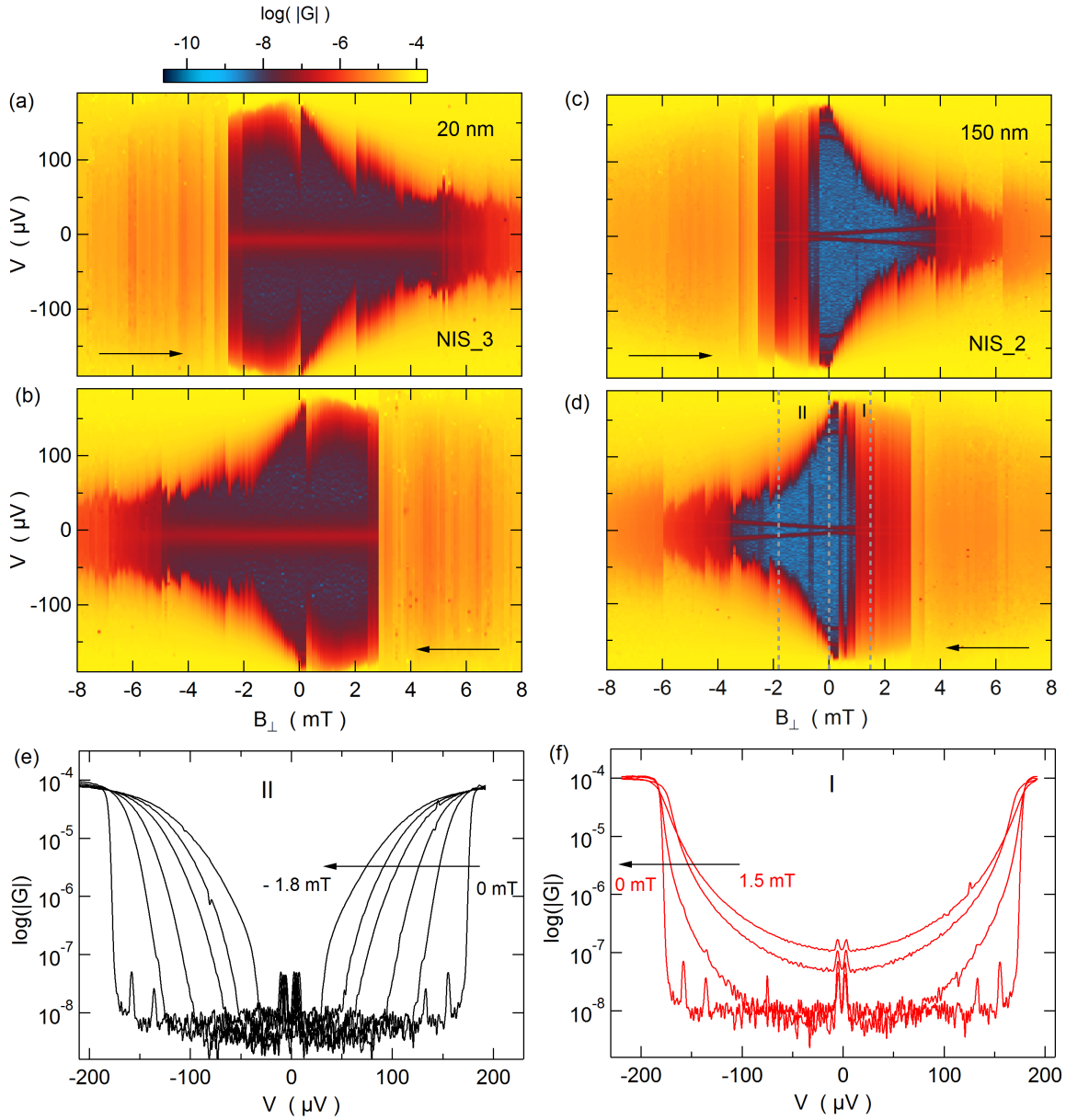


Figure 5.12: (a-d) Logarithm of the absolute value of the differential conductance is shown as a function of B_{\perp} and voltage bias. Black arrows indicate the sweep direction of B_{\perp} . The grey dashed lines in (d) indicate two regions I and II of the analysis. (e) Vertical cuts of region II, showing the evolution of the gap. (f) Vertical cuts for the region I.

5.7.8 Demagnetization

We present measurements of the step temperature T_{step} after performing a demagnetization process, which cools the Cu plate temperature T_{Cu} down to ~ 1 mK. As shown in Fig. 5.13, T_{step} decreases from roughly 7 mK down to 4 mK in the first few hours after

the demagnetization process. The values of T_{step} are scattered around a mean value of 4 mK with a standard deviation of 0.7 mK. The spread of the temperature values and the lowest temperature might be limited by the voltage noise, which needs to be less than 400 nV to resolve a temperature broadening of 4 mK, by using $eV_{noise} = k_B T_{step}$.

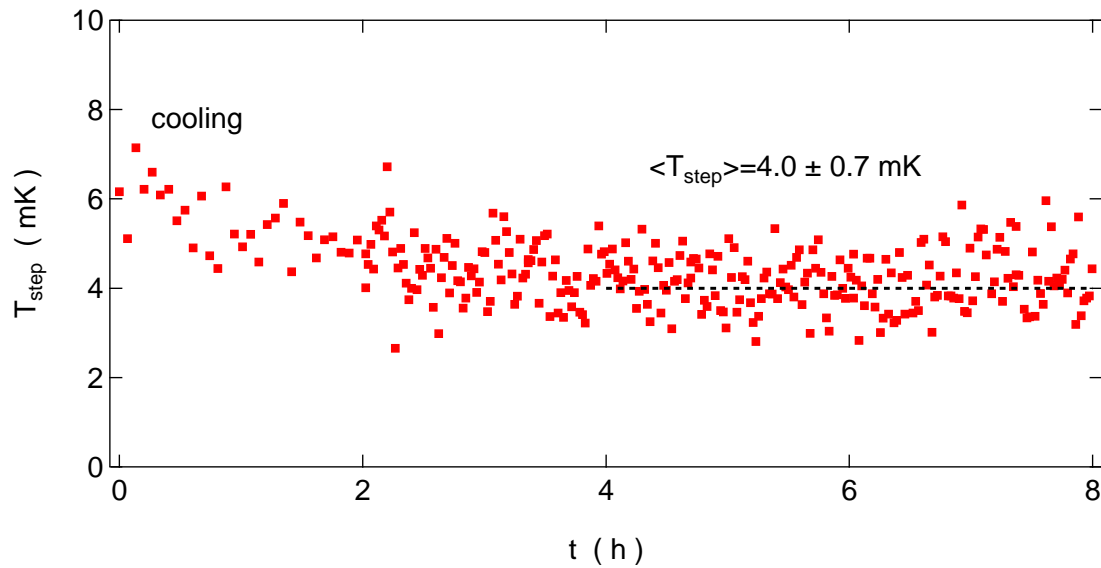


Figure 5.13: T_{step} as a function of the time after performing an adiabatic nuclear demagnetization. The black dashed line indicates the mean value of T_{step} in the time interval between 4 and 8 hours

6 On-and-off chip cooling of a Coulomb blockade thermometer down to 2.8 mK

M. Palma^{1*}, C. P. Scheller^{1*}, D. Maradan^{1,2}, A. V. Feshchenko³, M. Meschke³ and
D. M. Zumbühl¹

¹ *Department of Physics, University of Basel, CH-4056 Basel, Switzerland*

² *Physikalisch-Technische Bundesanstalt (PTB), Bundesallee 100, 38116
Braunschweig, Germany*

³ *Low Temperature Laboratory, Aalto University, FI-00076 Aalto, Finland*

Abstract

Cooling nanoelectronic devices below 10 mK is a great challenge since thermal conductivities become very small, thus creating a pronounced sensitivity to heat leaks. Here, we overcome these difficulties by using adiabatic demagnetization of *both* the electronic leads *and* the large metallic islands of a Coulomb blockade thermometer. This reduces the external heat leak through the leads and also provides on-chip refrigeration, together cooling the thermometer down to 2.8 ± 0.1 mK. We present a thermal model which gives a good qualitative account and suggests that the main limitation is heating due to pulse tube vibrations. With better decoupling, temperatures below 1 mK should be within reach, thus opening the door for μ K nanoelectronics.

* These authors contributed equally to this work.

This chapter is submitted to *Appl. Phys. Lett.* [arxiv:1708.09491](https://arxiv.org/abs/1708.09491).

6.1 Introduction

Reaching ultralow temperatures in electronic transport experiments can be key to novel quantum states of matter such as helical nuclear spin phases [11–13], full nuclear spin polarization [132], quantum Hall ferromagnets [132] or fragile fractional quantum Hall states [5, 6]. In addition, the coherence of semiconductor and superconducting qubits [15–17] as well as hybrid Majorana devices [18–20, 133] could benefit from lower temperatures. With this motivation in mind, we built a parallel network of nuclear refrigerators [31] to adapt the very well established technique of Adiabatic Nuclear Demagnetization (AND) [1, 26, 27] for electronic transport experiments. In this approach, the concept is to cool a nanoelectronic device directly through the electronic leads, which remain effective thermal conductors also below 1 mK. Each wire is cooled by its own, separate nuclear refrigerator in form of a large Cu plate. However, despite recent progress [33, 37, 40, 41, 43, 63, 134, 135], it remains very challenging to cool nanostructures even below 10 mK. Due to reduced thermal coupling, these samples are extremely susceptible to heat leaks such as vibrations [33], microwave radiation [49, 89], heat release [1] and electronic noise [63].

Metallic Coulomb blockade thermometers (CBTs) have been established as precise and reliable electronic thermometers [32, 136, 137], operating down to 10 mK and slightly below [34, 40, 41, 43]. These typically consist of linear arrays of Al/AlO_x/Al tunnel junctions with metallic islands in-between, consisting mainly of copper, see Fig. 6.1. The array divides the electronic noise per island by the number of junctions in series. This makes them less susceptible to electronic noise, but thermal conduction via Wiedemann-Franz cooling is not very effective through a series of resistive tunnel junctions. For this reason, the islands were enlarged into giant cooling fins [137] providing a huge volume for effective electron-phonon coupling and cooling through the substrate. At low temperatures, however, this eventually fails due to the very strong T^5 temperature dependence of the electron phonon coupling.

For a *single* tunnel junction[42, 43], on the other hand, two low-resistance reservoirs adjacent to the junction can be cooled efficiently by electronic leads making contact to nuclear refrigerators. Thus, in a noisy environment, on-chip nuclear demagnetization of the large fins offers itself as an elegant solution for a CBT array, providing local, in-situ cooling without having to go through potentially ineffective tunnel barriers or an insulating substrate. The large volume of the metallic islands now is taken advantage of as the spin reservoir of an AND refrigerator. At sufficiently low temperature, the electron-phonon coupling becomes so weak that the islands decouple thermally from the substrate, thus giving a low heat leak, as desired for efficient cooling. Previously, AND was applied to AlMn based single electron transistors [138] and CBTs with electroplated islands [40, 41], in both cases reducing the electronic temperature by roughly a factor of two.

In this Letter, we perform AND in *both* the Cu plates in the leads *and* the massive CBT islands, thus combining direct on-chip cooling with a reduced external heat leak emanating from the leads. We obtain significantly improved cooling, lowering the electronic temperature by a factor of 8.6, from ~ 24 mK down to 2.8 ± 0.1 mK, thereby further reducing the lowest reported electronic temperature in a solid state device [41]. We present a simple model giving a qualitative account of the cooling cycle. The performance is limited by a heat leak caused by the pluse-tube vibrations. With improved decoupling, the micro-Kelvin regime in nanoelectronics should be within reach.

6.2 Experimental Setup and CBT Device

The present experiment is performed on a cryo-free platform [33, 51], where each of the 16 leads is equipped with its own nuclear refrigerator (see Fig.6.1), consisting of two moles of copper. The system allows for cooling of the Cu pieces down to $T_{\text{Cu}} = 150 \mu\text{K}$ [33], see supplementary chapter for details. To integrate the CBT, it is placed inside a Cu box, see Fig. 6.1(a), which will also be demagnetized and further

shields the CBT from high frequency radiation, arising e.g. from higher temperature stages of the refrigerator. The Cu box is equipped with coaxial MMCX connectors, and connected directly to additional Ag-epoxy microwave filters [34]. The microwave filters used here are made from rather thick copper wire (0.35 mm instead of 0.1 mm) and contain a thicker and longer copper core, thus facilitating direct demagnetization of the filters themselves. The Cu box and the microwave filters are glued onto a Cu nuclear refrigerator with conductive Ag-epoxy in order to ensure good thermalization. The CBT consists of an array of 16 large metallic islands with $1 \mu\text{m}^2$ AlO_x tunnel barriers in-between, as shown in Fig. 6.1(b,c). This gives a device resistance of $150 \text{ k}\Omega$ and provides a rather small charging energy $E_c \approx 6.5 \text{ mK}$, thus allowing accurate thermometry down to $\approx 2 \text{ mK}$ [139]. The islands are of almost macroscopic size (Cu layer $\approx 810 \cdot 260 \cdot 0.2 \mu\text{m}^3$), making available a large reservoir of nuclear spins for demagnetization, see supplementary chapter.

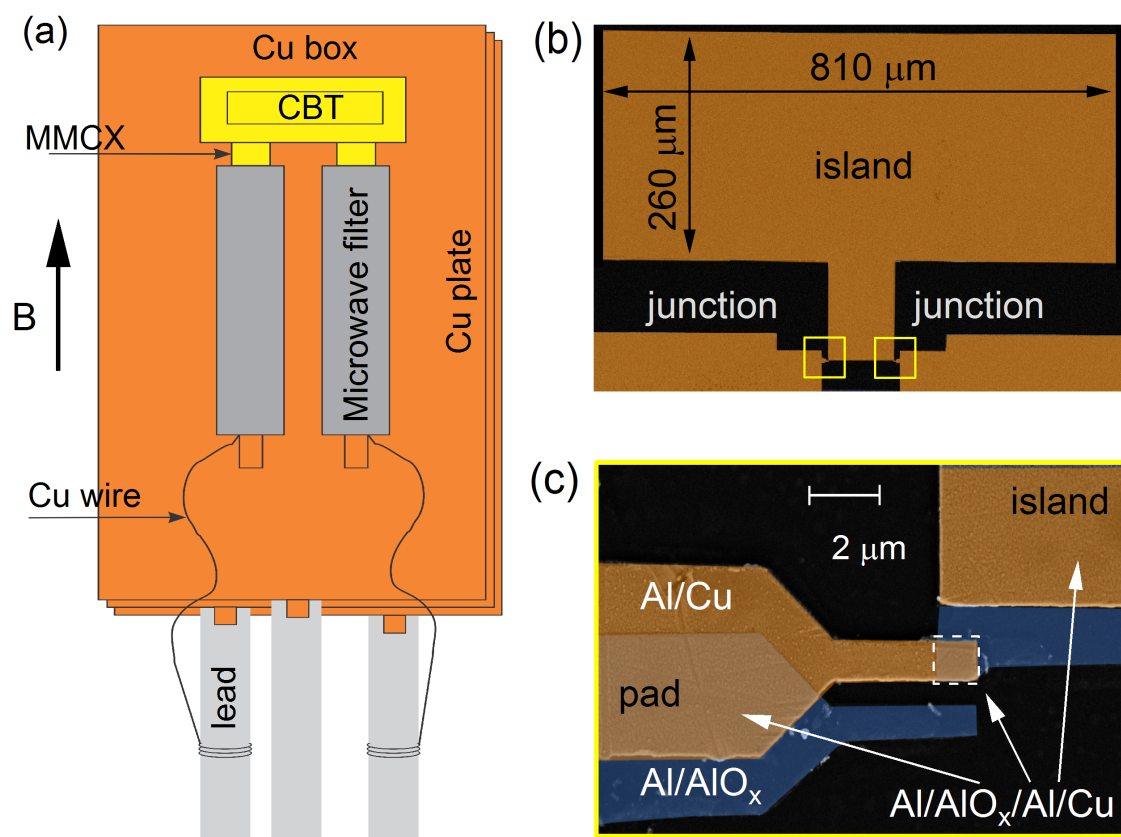


Figure 6.1: (a) Schematic with CBT enclosed in a copper box (yellow), connected to Ag-epoxy microwave filters (grey), and glued onto a Cu plate (orange) with Ag-epoxy. (b) Electron micrograph (false color) of the CBT island (volume $\approx 42,000 \mu\text{m}^3$), with tunnel junctions (inside yellow rectangles) to adjacent Al/AlO_x/Al/Cu pads. The brown sections comprise very large areas, giving very low resistances of these large junctions. (c) Zoom-in of a tunnel junction from (b), showing the overlap (white rectangle) between the top layer (Al/Cu, brown) and the bottom layer (Al/AlO_x, blue).

6.3 Measurements

In order to extract the electronic temperature of the device, we measure the 2-wire differential conductance g of the CBT as a function of the bias voltage V_{bias} by means of a standard low-frequency lock-in technique using a few μV of AC excitation. Figure 6.2(a) shows typical conductance traces, measured at various refrigerator temperatures, as indicated. Due to Coulomb blockade effects[140], the zero bias conductance g_0 is suppressed below its asymptotic, large bias value g_T . Both width and depth of the conductance dip are commonly used for thermometry[134, 137]. While fitting the full conductance trace allows one to use the CBT as a primary thermometer, using the depth of the zero bias dip requires pre-calibration and thus can be used only as a secondary thermometer. However, the primary mode is prone to overheating due to the large applied DC bias. This effect becomes particularly important at the lowest temperatures, illustrated in Fig. 6.2(a). The conductance g_0 measured while permanently staying at zero bias⁹ is clearly lower in conductance (dark blue marker) – and thus also lower in temperature – than the one obtained from a bias sweep at the same refrigerator temperature (dark blue trace), see also supplementary chapter. Therefore, the CBT is used in secondary mode here for the rest of this work [13, 134, 137].

The normalized Coulomb blockade zero bias dip $\delta g = 1 - g_0/g_T$ is given by the third order expansion [137]

$$\delta g = u/6 - u^2/60 + u^3/630, \quad (6.1)$$

for sufficiently small u (see below), where $u = E_c/k_B T_{\text{CBT}}$, and k_B is the Boltzmann constant. The inset of Fig. 6.2(b) shows the measured δg as a function of temperature T_{Cu} (red circles) along with a fit (solid black) performed in the high temperature regime above 30 mK using Eq. 6.1. The fit delivers the charging energy $E_c = 6.5 \pm 0.1$ mK, which now allows us to convert the measured δg to T_{CBT} for the whole temperature regime, thus providing the calibration of the secondary thermometer. The fit agrees very well

⁹This requires careful input voltage drift stabilization as provided by our home built IV converter, particularly below 10 mK [141]

with the data for high temperatures, but weak overheating is seen at lower temperatures $T_{\text{CBT}} \lesssim 30$ mK, see Fig. 6.2b inset.

The CBT calibration curve Eq. 6.1 is becoming more benign at the lowest temperatures, where a much larger change in δg is required for a given change in T_{CBT} compared to high temperatures. Thus, a small deviation in δg has a very small effect on the temperature reading and the calibration curve becomes more accurate at the lowest temperatures. The validity of Eq. 6.1 was investigated in detail in Ref. [139], showing that an accurate temperature reading to within $\sim 10\%$ error or less is obtained as long as $u \lesssim 3$. In practice, this means that the extracted CBT temperature, shown in Fig. 6.2(b) as a function of Cu plate temperature T_{Cu} , would be quite precise down to roughly 2 mK.

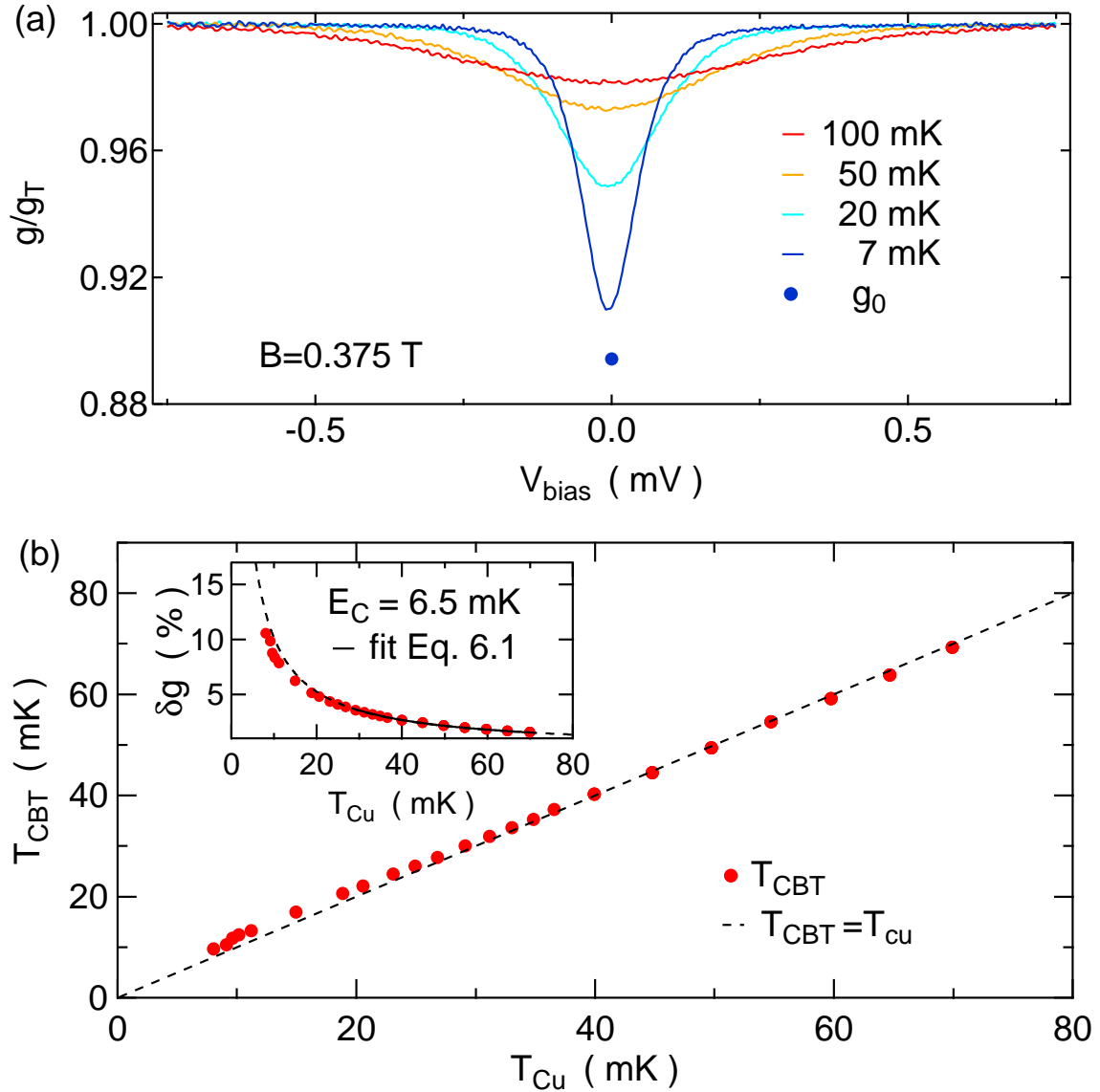


Figure 6.2: (a) Bias dependence of the differential conductance g normalized with the high bias conductance g_T , shown for various Cu plate temperatures T_{Cu} . An in-plane field $B = 0.375$ T drives the Al thin films normal. The zero bias conductance (dark blue circle, measured after equilibrating at $T_{\text{Cu}} = 7$ mK) remains clearly below the bias sweep (dark blue curve). (b) CBT temperature T_{CBT} versus T_{Cu} . The diagonal dashed line indicates ideal thermalization $T_{\text{CBT}} = T_{\text{Cu}}$. The inset shows the normalized zero bias conductance dip δg as a function of T_{Cu} . A fit using Eq. 6.1 is done over the high temperature, well thermalized regime $T_{\text{Cu}} \geq 30$ mK (solid black curve) and delivers the charging energy E_c of the device as the only fit parameter. The dashed curve indicates the low temperature extension below 30 mK of the fit with the same E_c .

6.4 Magnetic Cooling of a CBT and Cu Plate

In the second part of this Letter, we address the simultaneous adiabatic nuclear demagnetization (AND) of the CBT and its leads. AND is a single shot technique comprising three stages. First, magnetization of the nuclear spins at large initial magnetic field $B_i = 9$ T is performed. Then, the actual demagnetization is carried out down to a final field B_f of 0.375 T. Finally, the warm up stage commences, where a heat load is warming up the system until the magnetization is exhausted. Here, B_f is limited by the critical field required to break superconductivity of the Al thin film in the CBT.

Upon increasing the magnetic field to 9 T, a large amount of heat due to the magnetization of the nuclear spins has to be drained into the mixing chamber in order to polarize the nuclear spins during precooling, depicted in Fig. 6.3(a). The heat switches of the parallel refrigerator network are therefore driven normal to obtain a strong thermal link to the mixing chamber. While T_{Cu} (orange markers, Fig. 6.3(a)), eventually closely approaches the mixing chamber temperature T_{MC} (red solid line), the CBT temperature (blue data) is increased much more during ramping of the magnetic field to $B_i = 9$ T and saturates significantly above T_{MC} , indicating a significant heat leak onto the CBT and a weak thermal link between the CBT and the Cu plates. After precooling for almost 3 days, we obtain $T_{\text{Cu}} \approx 10$ mK and $T_{\text{CBT}} \approx 24$ mK, which sets the starting point for the nuclear demagnetization¹⁰.

In the second AND step, shown in Fig. 6.3(b), the nuclear stage is thermally decoupled from the mixing chamber (heat switches in the superconducting state) and the magnetic field is ramped down slowly to its final value $B_f = 0.375$ T. This reduces the nuclear spin temperature according to $T_f = T_i \cdot B_f/B_i$ for an ideal adiabatic process, where T_i and T_f denote initial and final temperature, respectively. The efficiency $\xi \leq 1$ of the process can be defined as the ratio of the realized and the ideal, adiabatic temperature reduction [31] $\xi = T_i/T_f \cdot B_f/B_i$, where $\xi = 1$ corresponds to perfect adiabaticity. The

¹⁰This corresponds to a nuclear polarization of $\approx 40\%$ in the Cu plates and $\approx 17\%$ in the CBT islands[1].

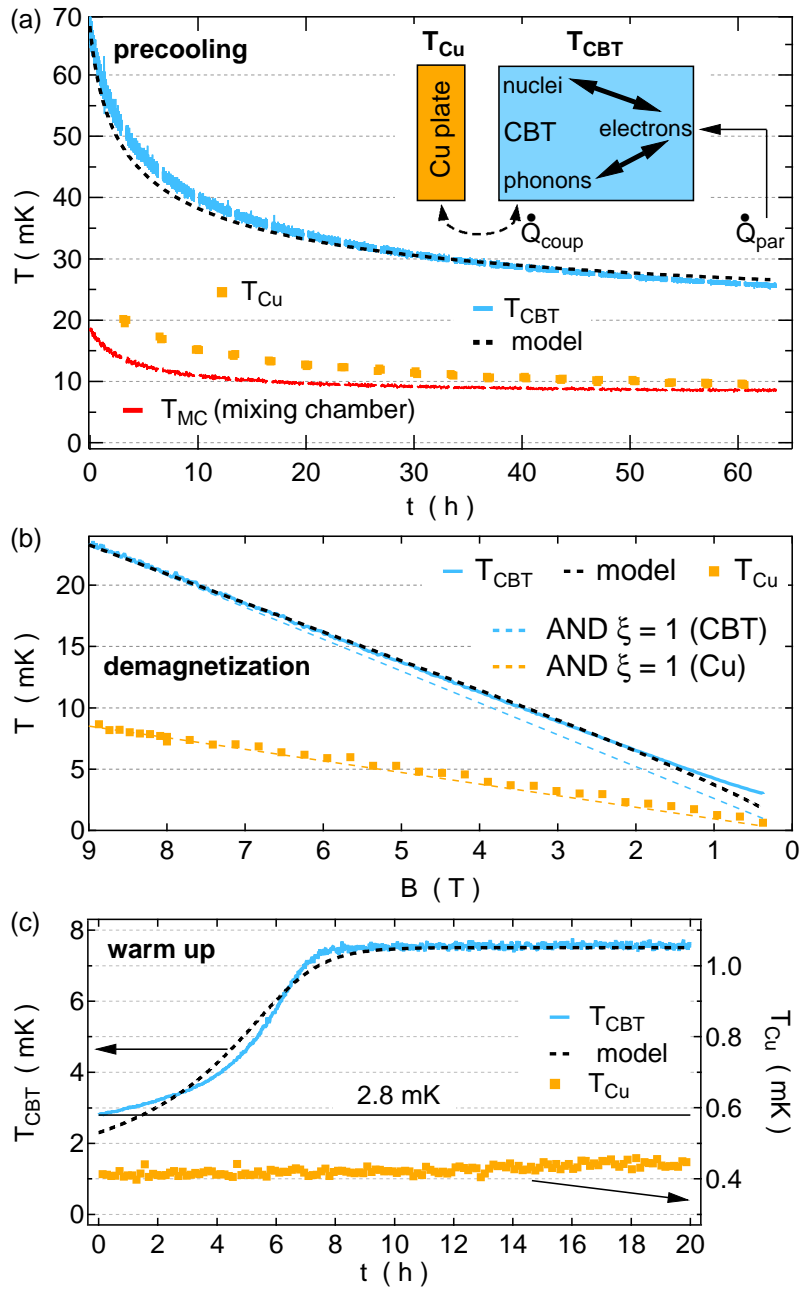


Figure 6.3: (a) Various temperatures as a function of the precooling time, as labeled. The inset shows a schematic of the thermal model. (b) Evolution of various temperatures during the AND process. Blue and orange dashed line indicate ideal cooling of CBT and Cu plates, respectively. (c) Warm up curves for various thermometers. The model is shown as black dashed curve for all panels.

AND process for the Cu plates (orange markers in Fig. 6.3(b)) is almost ideal (orange dashed line), resulting in an efficiency $\xi \gtrsim 0.9$. A larger deviation is observed for the CBT (compare blue data and dashed blue line), resulting in $\xi \gtrsim 0.35$. However, despite the reduced efficiency for the CBT, we obtain a significant reduction in CBT

temperature by a factor of 8.6, giving a final T_{CBT} of 2.8 ± 0.1 mK. These error bars result from the uncertainty in E_c , obtained from the curve fit in the inset of Fig. 6.2(b). The present measurement shows significantly improved AND efficiency compared to previous works [40, 41] and constitutes an important step towards the μK regime.

To get more insight about the thermal coupling of the CBT to its environment, we monitor the warm up process after AND, shown in Fig. 6.3(c). While T_{Cu} remains almost constant during the twenty hours period of time investigated here (increase by less than $50 \mu\text{K}$), the CBT starts to warm up immediately and reaches an equilibrium value of 7.5 mK after eight hours. Furthermore, the CBT conductance does not recover its low temperature zero bias value when returning to zero bias after performing a bias sweep of the CBT after AND (not shown). Instead, it saturates at 7.5 mK, while the Cu plates are still well below 1 mK. These observations indicate a rather limited spin reservoir due to the finite size of the CBT islands as well as a significant heat leak due to applied bias, in a limit where the CBT is well decoupled from the Cu plates. This indicates that the AND process directly demagnetizes the CBT while little cooling power is provided externally from the Cu plates.

6.5 Thermal Model

In order to obtain a more quantitative insight, a simple thermal model is developed (schematic in inset of Fig. 6.3(a)) to qualitatively capture the main features of the experiment. For the Cu plates and the CBT islands, we have three different thermal subsystems, namely phonons, electrons and nuclei. We note that at low temperature, the largest contribution to the specific heat by far is provided by the nuclei. Electrons are coupled on one hand to the nuclear bath by the hyperfine interaction via the Korringa link [1], and on the other hand to the phonon bath by means of the electron-phonon interaction. Hence, nuclei and phonons are only indirectly coupled through the electronic system.

The CBT device with its large metallic islands is in principle connected thermally to the

Cu plates through its electronic leads and through its substrate. For an array of resistive tunnel junctions separating the islands from the leads, the resulting Wiedemann-Franz cooling turns out to be weak. Given the insulating substrate on which the CBT resides, there is only the phonon degree of freedom available for transferring heat between Cu plates and CBT islands – thus again giving only weak coupling. This phonon process contains several thermal resistances in series, namely the weak electron-phonon coupling in the CBT islands (negligibly weak resistance in the Cu plates due to their much larger size), the acoustic mismatch at the metal-semiconductor interfaces giving rise to a Kapitza boundary resistance [1, 142] and finally the weak thermal conductivity within the insulating substrate itself. In presence of a finite heat leak onto the CBT islands, these weak thermal links lead to a significant temperature difference between CBT and Cu plates and associated long time constants, as observed, particularly during precooling.

Given such a limiting bottle neck between Cu plates and CBT islands, we assume the electronic, phononic and nuclear temperature within the CBT itself to be well coupled (bold arrows in the schematics) and equilibrated. Thus, in a simplified model, the CBT is taken as a single thermal system carrying the nuclear specific heat and is assumed to be weakly coupled to the Cu plate through $\dot{Q}_{\text{coup}} = A(T_{\text{CBT}}^p - T_{\text{Cu}}^p)$ (dashed arrows), where the coupling constant A and the exponent p are fit parameters. In addition, a parasitic heat load \dot{Q}_{par} to the CBT is assumed to subsume e.g. electronic noise, heat release, or pulse tube eddy current heating, see supplementary chapter.

We obtain qualitative agreement between model and data for all three stages of the AND process – precool, demagnetization and warm up – using a single coupling constant $A = 7.6 \cdot 10^{-12} \text{ W/K}^3$, and a static parasitic heat leak (during precool and warm up) of $\dot{Q}_{\text{par}} = 32 \text{ aW}$ per island. However, a substantially increased dynamic heat load of $\dot{Q}_{\text{par}} = 485 \text{ aW}$ has to be assumed during demagnetization in order to explain the low demagnetization efficiency in Fig. 6.3(b). Furthermore, we allow for a weak temperature dependence of the coupling exponent p , reducing its value from $p = 3.2$

during precool to $p = 2.7$ during demagnetization and further down to $p = 2.5$ for the warm up process. Similar exponents were also obtained in earlier works [13, 134]. Under these assumptions, the thermal response of the CBT is qualitatively captured by the model.

We note that significant temperature differences between electronic and nuclear system would lead to initial cooling effects during the warm up process due the much smaller static heat leak compared to the dynamic case. This is in contrast to the measurements, thus supporting the hypothesis of equilibrated subsystems within the CBT. We also observe that the parasitic heat determined from warm up curves of the Cu plates[33] is similar to that obtained from the CBT model here ¹¹. This suggests that both the cooling power as well as the parasitic heat leak scale with the volume and area of copper used. This is confirmed with measurements on a different CBT (see supplementary chapter), showing very similar demagnetization performance despite CBT islands which are about 150 times smaller in area and volume. Thus, the predominant heat leak is not coupling in through the leads of the CBT (e.g. electronic noise or external electronic heat leak), but rather through the area or volume of the islands (e.g. microwave absorption or eddy currents and material heat release).

6.6 Conclusion

In conclusion, we demonstrate simultaneous on-and-off chip magnetic cooling of a CBT with an efficiency of 35 %, thereby lowering the device temperature by a factor of 8.6 from 24 mK down to 2.8 mK. The CBT remains colder than the dilution refrigerator mixing chamber for more than 6 hours. Future improvements include improved microwave filtering, reduction of vibration induced eddy current heating due to active damping, better mounting and by rigidly fixing the support structure of the nuclear stage to the mixing chamber shield and magnet support assembly [39]. This should

¹¹Static heat leak: 32 aW per CBT junction, corresponding to 5.4 nW/mol Cu, compared to typically 1 – 2 nW/mol Cu for the large plates. Dynamic heat leak: 485 aW per junction during AND, corresponding to 82 nW/mol Cu, compared to an estimated 30 nW/mol Cu for the large plates. [33]

improve the currently inefficient precooling process as well as reduce the large dynamic heat leak, and thus reduce the final temperature after AND.

6.6.1 Acknowledgments

We would like to thank H. J. Barthelmeß, R. Blaauwgeers, J. P. Pekola, G. Pickett, and P. Vorselman for useful input and discussions. The work shop teams of M. Steinacher and S. Martin are gratefully acknowledged for technical support. This work was supported by the Swiss NSF, NCCR QSIT, the Swiss Nanoscience Institute, the European Microkelvin Platform (EMP), an ERC starting grant (DMZ), and EU-FP7 MICROKELVIN and ITN Q-NET 264034 (AVF).

6.7 Supplementary Material

6.7.1 Sample Fabrication and Mode of Operation

The device is fabricated on top of a silicon wafer with an insulating SiO₂ layer in two steps using electron-beam lithography. In the first lithography step, a ground plane is created that consists of 50 nm of Cu and is covered by a 100 nm of Al₂O₃ insulator, grown by atomic layer deposition. In the second lithography step, a 40 nm thick Al bottom electrode is evaporated and subsequently *in-situ* thermally oxidized. After the oxidation, a 40 nm thick top Al electrode is evaporated under a different tilt angle (two-angle shadow mask evaporation), thereby forming an Al-AlO_x-Al tunnel junction of 1 μm² area. Finally, the top Al electrode is overgrown with a 200 nm thick Cu layer of the same geometry and tilt angle. Hence, the Cu layer of the top electrode makes available a large reservoir of nuclear spins that may be used for adiabatic nuclear demagnetization (AND) experiments.

Metallic Coulomb blockade thermometers (CBTs) can be operated in two different modes, either as a primary thermometer, where the electronic temperature is inferred from the full bias dependence (or simply the full width at half maximum of the zero bias

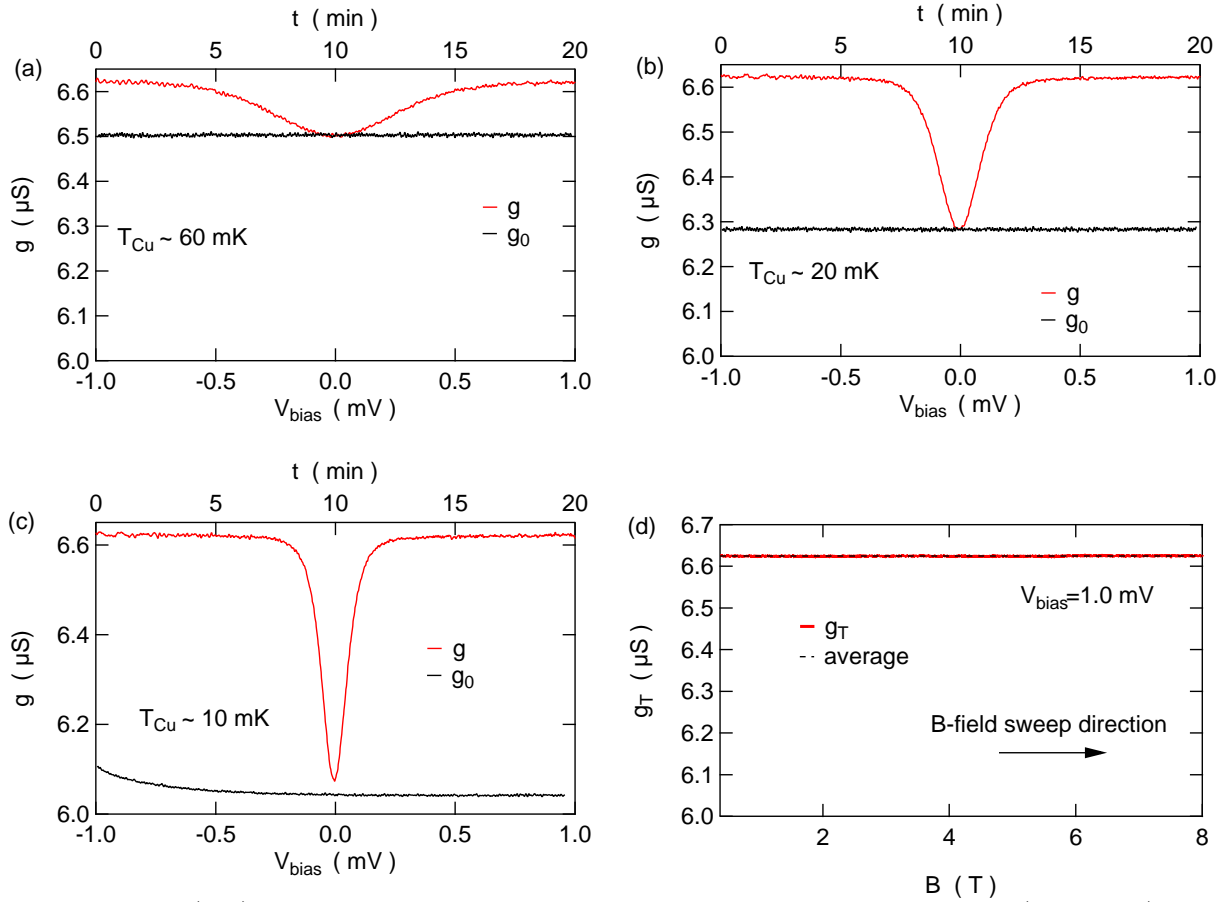


Figure 6.4: (a-c) Differential conductance as a function of voltage bias (red data), shown for different temperatures as indicated. In addition, the differential conductance measured at zero bias as a function of time (data taken immediately after the corresponding bias scan) is shown in black, plotted versus the upper axis. (d) High bias ($V_{\text{bias}} = 1$ mV) magneto-conductance g_T and its average value are shown in red and black, respectively. No magnetic field dependence is observed.

conductance dip, when neglecting ohmic heating effects), or as secondary thermometer. In the latter mode of operation, the relative conductance dip size $\delta g = (g_T - g_0)/g_T$ can be used as a measure of temperature after pre-calibration at high temperature where the device is at equilibrium with the Cu plates, $T_{\text{Cu}} = T_{\text{CBT}}$. Here, g_0 and g_T denote the conductance at zero and high bias, respectively. Figure 6.4(a,b,c) shows bias traces in red color, recorded at $T_{\text{Cu}} = 60$ mK, $T_{\text{Cu}} = 20$ mK, and $T_{\text{Cu}} = 10$ mK, respectively. In addition, the zero bias conductance traces (black curves), measured as a function of time right after the respective bias traces, are shown. At high temperature $T_{\text{Cu}} > 15$ mK, the minimum conductance from bias traces agrees very well with g_0 measured as a function of time at effectively zero bias, see Fig. 6.4(a,b). However, a clear deviation

is observed at low temperature e.g. $T_{\text{Cu}} = 10 \text{ mK}$, where the conductance g_0 drops over a time scale of roughly ten minutes and saturates well below the minimum value obtained from the bias scan, as seen in Fig. 6.4(c). This indicates overheating of the device at finite bias. The thermal relaxation time is very long and increases sharply at lower temperatures. Thus, there is not nearly enough time for adequate equilibration of the zero bias point taken during the scan. Scanning at sufficiently slow speed would consume hours or longer and is therefore not practical. In addition, while some steady state situation may be reached eventually after a long time, this may still be in an overheated state when not at zero bias. We therefore measure exclusively at zero bias to avoid overheating and use the relative conductance dip size after pre-calibration to measure temperature.

Staying very close to zero bias within a narrow window of tolerance over long periods of time e.g. hours or days is not trivial. Commercially available instruments usually have significant drift of $\pm 10 \mu\text{V}$ or more of the voltage emanating from the amplifier input (input voltage), thus changing the bias voltage. To avoid these problems, we have built a low noise, high stability current preamplifier which keeps its input voltage stable within $\pm 0.15 \mu\text{V/K}$, see Ref. [141] for details. This eliminates the need for any cumbersome corrections or external feedback to keep the bias very close to zero voltage. In addition, applying a high bias to the CBT quickly destroys any previous nuclear heat capacity and AND cooling, thus giving us yet another reason to only monitor the zero bias conductance, particularly during demagnetization and warm up in the main text. For reliable temperature extraction, we need to assume that the high bias tunneling conductance value g_T (needed for calculation of the relative conductance dip size $\delta g = 1 - g_0/g_T$) is independent of magnetic field. In order to test this assumption, the magneto-conductance at $V_{\text{bias}} = 1 \text{ mV}$ is shown in Fig. 6.4(d). Indeed, the high bias conductance is observed to be B-field independent to within our measurement error. This guarantees that the sole measurement of the zero bias conductance is a reliable and simple thermometer.

6.7.2 Experimental Setup

Efficient thermalization and filtering of the leads from room temperature down to the mixing chamber (MC) is required in order to sufficiently suppress microwave radiation. The leads consist of thermocoaxes [49], thermalized to the different temperature stages of the dilution refrigerator, followed by low resistance home-built Ag-epoxy microwave filters [34] and standard 2-pole RC-filters with 45 kHz cut-off frequency. After the filtering stages, the leads are fed through the mixing chamber, where they are efficiently thermalized with the ^3He – ^4He mixture by means of Ag-sinters [31, 33]. They continue as massive, annealed Ag-wires and finally, each wire is spot-welded to its own Cu plate. In order to thermally decouple the Cu pieces from the mixing chamber during AND, the silver wires are fused to Aluminum heat switches [50]. The temperature of the Cu pieces is measured with a magnetic field fluctuation thermometer [45, 46, 52], connected to a SQUID amplifier¹². This thermometer performs an inductive read-out of the thermal currents inside an annealed Ag-wire [53, 54], which is well thermally coupled to one of the Cu pieces.

6.7.3 Warm up With Heat Applied to the Cu Plates

In the main text, the warm up of the CBT was monitored for the first 20 hours after nuclear demagnetization. After roughly 8 hours the CBT temperature increased and saturated at 7.5 mK electron temperature, while the Cu plate temperature T_{Cu} is almost unchanged during this period. Here, we discuss the further warm up behavior of the CBT, when the Cu plates themselves start to warm up. In order to speed up this process, a heat load is applied to three Cu plates (100 nW/plate). One of these plates carries the MFFT thermometer, used to measure the Cu plate temperature, and serves at the same time as one of the leads for the CBT. The other two plates are left without additional function.

¹²1-stage current sensor C4L1W DC-SQUID, Magnicon GmbH, Hamburg, Germany.

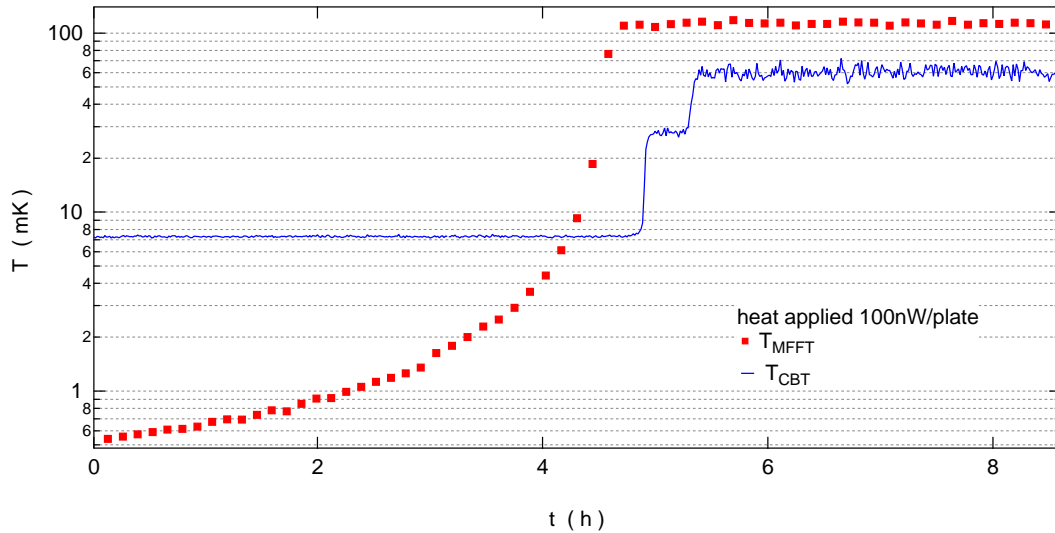


Figure 6.5: Warm up curves T_{CBT} and T_{Cu} for the CBT and the Cu plate, respectively, upon applying an external heat load of 100 nW/plate (for 3 different Cu plates).

The Cu plate reacts immediately to the large external heat load, rises above 1 mK after a bit more than 2 hours, and finally heats above the CBT temperature after more than 4 hours. About half an hour after this crossing of temperatures, and roughly ten minutes after the complete Cu plate warm up, T_{CBT} jumps abruptly up to ≈ 30 mK, see first step in T_{CBT} in Fig. 6.5. Before that, the CBT temperature remains constant for the first ≈ 5 hours, indicating strong thermal decoupling of those systems. After waiting another ≈ 15 minutes at ≈ 30 mK, a second step is observed, raising the CBT temperature to ≈ 60 mK. The second step is possibly due to a delayed warm up of the Cu plate hosting the CBT, which is not directly heated.

6.7.4 High Charging Energy CBT

Here, we compare on-and-off chip magnetic cooling of a second CBT device with higher charging energy ($E_c = 17.2$ mK instead of $E_c = 6.5$ mK), different number of junctions (64 instead of 32 junctions) and much smaller CBT island volume ($300 \mu\text{m}^3$ instead of $42,000 \mu\text{m}^3$) compared to the one shown in the main text, see Fig. 6.6(b). As described in the main text, this can deliver some important clues about the origin of the heat leak. Both CBTs are mounted in the same Cu box (Faraday cage), use the same microwave filters, and are measured in two different cool-downs. While the relative conductance dip size in Fig. 6.6(a,b) clearly reflects the differing charging energies, the extracted electron temperature is the same in both cases, as expected. This holds also for the adiabatic nuclear demagnetization process, giving a final temperature of ≈ 2.5 mK after demagnetization, close to the 2.8 mK reported in the main text for the low charging energy device. However, while the $E_c = 17.2$ mK device is more accurate for the high temperature regime, precise temperature extraction (to within 10 %) is only guaranteed down to roughly 5 mK [137, 139]. Nonetheless, the demagnetization behavior of the two devices are consistent, thus giving additional confirmation for the low temperature results in the main text.

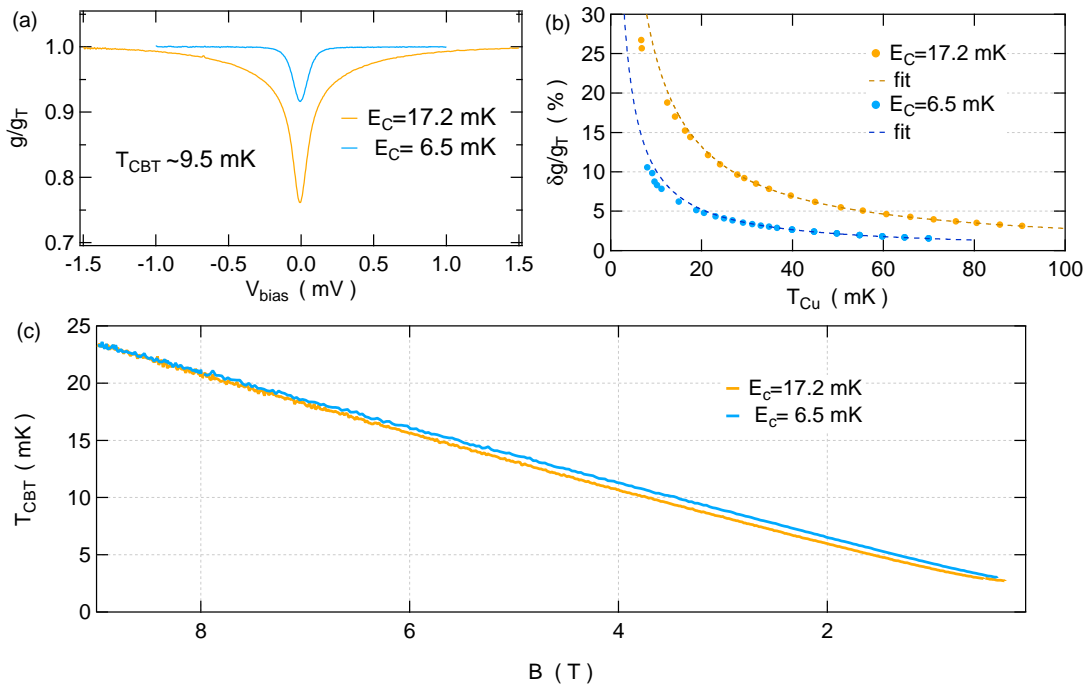


Figure 6.6: (a) Differential conductance as a function of voltage bias, normalized to the high bias value, shown for 2 devices with different charging energy, and recorded at base temperature of the refrigerator. (b) Relative conductance dip size versus temperature for the two devices in (a). Dashed traces are curve fits to Eq.1 from the main text, used to extract the charging energy. (c) CBT temperature for both devices, measured as a function of applied magnetic field during the adiabatic nuclear demagnetization process.

6.7.5 Vibrations and Electrical Noise

The large precooling temperature of the CBT (see main article) and the reduced efficiency during the adiabatic nuclear demagnetization process are the two main limiting factors for reaching lower temperatures. In this section, we discuss vibration induced eddy current heating as a possible cause for both factors. In order to investigate this scenario, the voltage across the CBT is measured during 50 s using a fast DAQ with the sample mounted in perpendicular configuration (in contrast to all other data). Fig. 6.7(a,b) show the Fast Fourier Transform (FFT) for such time traces, recorded at magnetic fields ranging from 80 mT up to 8 T.

The FFT shows frequency bands with varying noise level. In particular, up to 20 Hz, the level is rather low (note that lock-in measurements are done at 7 Hz) while it increases significantly above 20 Hz and has a pronounced peak structure around 140 Hz

(see integrated noise at 4 T in Fig. 6.7(c)). A zoom in around 140 Hz shows a clear substructure with very sharp peaks, separated exactly by the pulse tube frequency of 1.4 Hz. This suggests that around 140 Hz the nuclear stage vibrates at an eigenfrequency and is driven by the slow vibrations of the pulse tube. As the field is changing, some of these vibration noise peaks seem to grow while others become weaker. We note that at low field <0.1 T, the overall noise integrated up to 1 MHz is about $1 \mu\text{V}_{\text{rms}}$. At higher fields this increases by about an order of magnitude with a broad peak around 2-3 T. In addition to vibration induced noise, also the omnipresent 50 Hz noise peak (and its multiples, e.g. at 150 Hz) are clearly seen in the FFT spectrum. The electrical noise at 150 Hz shows small frequency variations, in contrast to the vibration induced peaks.

In conclusion, Fig. 6.7 suggests that there is a significant level of vibrations in the present system, which displaces the sample periodically from the center of the solenoid and therefore results in a time-dependent magnetic field. The resulting vibration induced eddy current heating may present one of the limiting factors for the current measurement and will be addressed in future experiments.

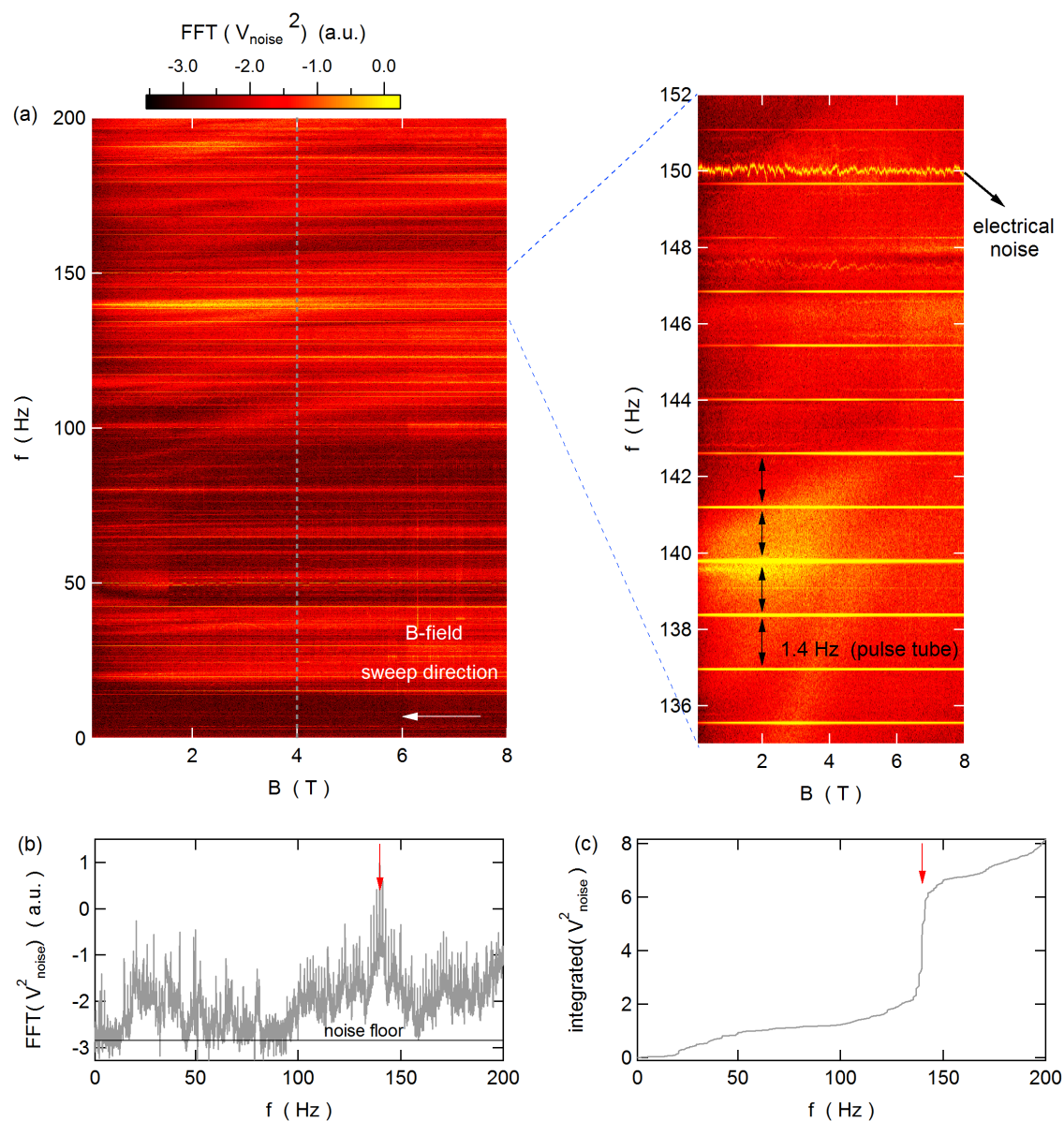


Figure 6.7: (a) Logarithm of the absolute value of the noise spectrum as function of the frequency and magnetic field. A zoom-in of the frequency range between 135 Hz and 152 Hz is shown on the right hand side. (b) Vertical cut of (a) at 4 T. (c) Integrated noise of the spectrum shown in (b). A red arrow indicates a large increase in the noise level around 140 Hz.

7 Conclusion & Outlook

In the first part of the thesis the focus is on the realization of a parallel network of Nuclear Refrigerator (NRs). We demonstrate successful cooling of the nuclear refrigerant down to $150\ \mu\text{K}$ and a reduction the residual heat leak to few nW/mol of Copper. Additionally, a simple thermal model of the demagnetization process, which takes into account the dynamic heat leak and the hyperfine link between electrons and nuclei, describes well the efficiency of the process. Now, the setup is being completed with a chip-socket to perform experiments on different devices. Two different chip-sockets have been tested, one made of Ag-epoxy with incorporated microwave filters and the other made of Sapphire without microwave filters. The latter performs better than the former, since it has less heat release so that the samples are cooled down to $13\ \text{mK}$ while for the Ag-epoxy socket the lowest temperature is only $16\ \text{mK}$ and the heat release is large. To improve the performance the Sapphire socket can be modified by incorporating microwave filters and using a Cu box instead of Ag-foil to shield samples from radiations and electrical noise.

The next step is to characterize the cooling power of our setups. For this purpose, we need on-chip thermometer, which is capable of operating below $10\ \text{mK}$. Thus, we employed a normal metal-insulator-superconducting (NIS) junction as the primary and secondary thermometer. The temperature is extracted by fitting the entire I-V curve or by a linear fit of the logarithm of the current in the exponential region of the I-V curve. A thermal model predicts the potential to reach $1\ \text{mK}$ in the junction, however, both methods saturate at $7.3\ \text{mK}$. One possible cause for the higher saturation temperature is the heat release of the Ag-epoxy socket, while another results from a residual magnetic field present in the sample after demagnetization. A small residual field at level of a Gauss might smear the superconducting density of states, which leads to higher temperature reading. Subsequent experiments on the sub-gap current steps demonstrate that some of the steps can be used as precise on-chip thermometer down

to 4 mK. The temperature reading of the steps is robust against the residual magnetic field, giving rise to a precise temperature reading after the demagnetization process. The lowest temperature measured by the steps might be limited by the voltage noise, which needs to be lower than 400 nV to resolve a thermal broadening lower than 4 mK. Additionally, since some steps cool and others do not, it might also be that some steps are more strongly coupled, leading to life-time broadening which at some finite temperature takes over and makes the thermometer saturates. The implementation of cryogenic amplifiers [143] and additional on-chip filtering [40, 144] can reduce the noise, which could lead to lower temperatures if the life-time broadening is not the limiting factor.

To further refrigerate the NIS junctions might be useful to perform on-chip magnetic cooling of them. The NIS has large Copper leads with low resistance, which makes a strong thermal link between the junction and the NRs, leading to a good thermalization during the precooling. There are two possible operation modes, one relies on-chip magnetic cooling of the NIS, and the other relies on magnetic cooling of the NRs, which transfer the cooling power to the NIS through the leads. One drawback of the first operation mode is that it is impossible to monitor the temperature during the demagnetization process, since the superconductivity of the junction is destroyed. However, it is possible to align the junction with the magnetic field in order to reduce perpendicular components once the demagnetization is finished, in order to recover the superconductivity and to use the steps as thermometer. In the Second mode the NIS junction needs to be shielded with superconducting shields, to preserve the superconductivity on the junction during the whole demagnetization process.

Besides serving as a thermometry, the sub-gap steps are related to Andreev bound states amplified by the disorder and the geometry of the junction. The numerical simulation used to describe the steps predicts an increase of the sub-gap conductance together with the disorder. The observation suggests that in a well filtered setup where the photon absorption is negligible, the sub-gap conductance for a diffusive junction

is only due to two-particle tunneling current given by interference effects enhanced by disorder and geometry. To complete the characterization of the steps and quantify the disorder, we can vary the metal thickness to observe the effects of surface defect on the disorder. Furthermore, changing the metal layer from Cu to Au might also help reduce surface defects, - i.e. roughness, surface oxidation-, which can affect the disorder.

In the last part of the thesis we demonstrate on-chip magnetic cooling of an array of Coulomb Blockade Thermometers with huge Copper islands down to 2.8 mK, which is the lowest temperature reported so far in electronic devices. The reduction in temperature is roughly a factor 8 compared to the previous experiments [41, 138], indicating an increased efficiency of the cooling technique, possibly due to the improved filtering and shielding of our setup. To further reduce the temperature, we need to decrease the rather high precooling temperature (~ 25 mK), which is limited by the weak coupling to the NRs and parasitic heat leaks due to vibrations and voltage noise. The coupling can be enhanced by using a conductive substrate, e.g. Si doped substrate or metallic substrate with thin oxide layer on top, instead of an insulating one.

Recent experiments have demonstrated cooling of GaAs heterostructure as low as 6 mK, using a large metallic island galvanically connected to the two-dimensional electron gas formed within the semiconductor heterostructure [135]. This approach together with conductive substrate can help lower the temperature of the two-dimensional electron gas. On this note, it may be useful to perform experiments on quantum dot thermometry on a filtered Sapphire socket, since they were performed by using a Macor socket [63], which is a well known source of heat release. Additionally, experiments on quantum dot at low temperatures can lead to new insights on the back-action effect of the charge sensing on the dot [145, 146], which may be relevant for the design and the operation of charge and spin qubits. It is interesting to carry out the magnetic cooling of GaAs heterostructures. Since Ga and As atoms have gyromagnetic ratios similar to Cu, ultra low temperature are likely to be achieved in such system. Significantly, at such low temperature, the two-dimensional ferromagnetic transition of the

nuclei in GaAs might be observed, which occurs at a transition temperature of roughly 1 mK [11, 12].

At sub-mK temperatures, many other phenomena can be explored such as fractional quantum Hall states with small gap [6, 147], strip of stripes phase [148, 149] in quantum Hall effect. In addition, ultra low temperature can solve the enigma of the saturation [150] or not of the coherence time at low temperatures [151]. Low electronic temperature can also benefit correlated many body system like Kondo effect [152].

References

- [1] F. Pobell. *Matter and Methods at Low Temperatures* (Springer, Berlin, 2007).
- [2] G. Frossati. *Obtaining ultralow temperatures by dilution of ^3He into ^4He* . Journal de Physique Colloques **39**, 1578 (1978).
- [3] D. J. Cousins, S. N. Fisher, A. M. Guénault, R. P. Haley, I. E. Miller, G. R. Pickett, G. N. Plenderleith, P. Skyba, P. Y. A. Thibault, and M. G. Ward. *An Advanced Dilution Refrigerator Designed for the New Lancaster Microkelvin Facility*. J. Low Temp. Phys. **114**, 547 (1999).
- [4] W. Pan, J. S. Xia, V. Shvarts, D. E. Adams, H. L. Störmer, D. C. Tsui, L. N. Pfeiffer, K. W. Baldwin, and K. W. West. *Exact quantization of the even-denominator fractional quantum Hall state at $\nu=5/2$ Landau level filling factor*. Phys. Rev. Lett. **83**, 3530 (1999).
- [5] W. Pan, K. W. Baldwin, K. W. West, L. N. Pfeiffer, and D. C. Tsui. *Fractional quantum Hall effect at Landau level filling $\nu = 4/11$* . Phys. Rev. B **91**, 041301 (2015).
- [6] N. Samkharadze, I. Arnold, L. N. Pfeiffer, K. W. West, and G. A. Csáthy. *Observation of incompressibility at $\nu = 4/11$ and $\nu = 5/13$* . Phys. Rev. B **91**, 081109 (2015).
- [7] C. Nayak, S. H. Simon, A. Stern, M. Freedman, and S. Das Sarma. *Non-Abelian anyons and topological quantum computation*. Rev. Mod. Phys. **80**, 1083 (2008).
- [8] J. D. Sau, R. M. Lutchyn, S. Tewari, and S. Das Sarma. *Generic New Platform for Topological Quantum Computation Using Semiconductor Heterostructures*. Phys. Rev. Lett. **104**, 040502 (2010).

-
- [9] S. Das Sarma, M. Freedman, and C. Nayak. *Topologically Protected Qubits from a Possible Non-Abelian Fractional Quantum Hall State*. Phys. Rev. Lett. **94**, 166802 (2005).
- [10] A. Stern and B. I. Halperin. *Proposed Experiments to Probe the Non-Abelian $\nu = 5/2$ Quantum Hall State*. Phys. Rev. Lett. **96**, 016802 (2006).
- [11] P. Simon, B. Braunecker, and D. Loss. *Magnetic ordering of nuclear spins in an interacting two-dimensional electron gas*. Phys. Rev. B **77**, 045108 (2008).
- [12] P. Simon and D. Loss. *Nuclear Spin Ferromagnetic Phase Transition in an Interacting Two Dimensional Electron Gas*. Phys. Rev. Lett. **98**, 156401 (2007).
- [13] C. P. Scheller, T.-M. Liu, G. Barak, A. Yacoby, L. N. Pfeiffer, K. W. West, and D. M. Zumbühl. *Possible Evidence for Helical Nuclear Spin Order in GaAs Quantum Wires*. Phys. Rev. Lett. **112**, 066801 (2014).
- [14] D. Loss and D. P. DiVincenzo. *Quantum computation with quantum dots*. Phys. Rev. A **57**, 120 (1998).
- [15] R. Hanson, L. P. Kouwenhoven, J. R. Petta, S. Tarucha, and L. M. K. Vandersypen. *Spins in few-electron quantum dots*. Rev. Mod. Phys. **79**, 1217 (2007).
- [16] J. Clarke and F. K. Wilhelm. *Superconducting quantum bits*. Nature **453**, 1031 (2008).
- [17] M. H. Devoret and R. J. Schoelkopf. *Superconducting Circuits for Quantum Information: An Outlook*. Science **339**, 1169 (2013).
- [18] V. Mourik, K. Zuo, S. M. Frolov, S. R. Plissard, E. P. A. M. Bakkers, and L. P. Kouwenhoven. *Signatures of Majorana Fermions in Hybrid Superconductor-Semiconductor Nanowire Devices*. Science **336**, 1003 (2012).

- [19] R. M. Lutchyn, J. D. Sau, and S. Das Sarma. *Majorana Fermions and a Topological Phase Transition in Semiconductor-Superconductor Heterostructures*. Phys. Rev. Lett. **105**, 077001 (2010).
- [20] J. Alicea. *Majorana fermions in a tunable semiconductor device*. Phys. Rev. B **81**, 125318 (2010).
- [21] J. Xia, E. Adams, V. Shvarts, W. Pan, H. Störmer, and D. Tsui. *Ultra-low-temperature cooling of two-dimensional electron gas*. Physica B: Condensed Matter **280**, 491 (2000).
- [22] J. S. Xia, W. Pan, C. L. Vicente, E. D. Adams, N. S. Sullivan, H. L. Störmer, D. C. Tsui, L. N. Pfeiffer, K. W. Baldwin, and K. W. West. *Electron Correlation in the Second Landau Level: A Competition Between Many Nearly Degenerate Quantum Phases*. Phys. Rev. Lett. **93**, 176809 (2004).
- [23] N. Samkharadze, A. Kumar, M. J. Manfra, L. N. Pfeiffer, K. W. West, and G. A. Csáthy. *Integrated electronic transport and thermometry at milliKelvin temperatures and in strong magnetic fields*. Rev. Sci. Instrum. **82**, 053902 (2011).
- [24] N. Deng, A. Kumar, M. J. Manfra, L. N. Pfeiffer, K. W. West, and G. A. Csáthy. *Collective Nature of the Reentrant Integer Quantum Hall States in the Second Landau Level*. Phys. Rev. Lett. **108**, 086803 (2012).
- [25] E. Kleinbaum, A. Kumar, L. N. Pfeiffer, K. W. West, and G. A. Csáthy. *Gap Reversal at Filling Factors $3+1/3$ and $3+1/5$: Towards Novel Topological Order in the Fractional Quantum Hall Regime*. Phys. Rev. Lett. **114**, 076801 (2015).
- [26] G. R. Pickett. *Microkelvin physics*. Rep. Prog. Phys. **51**, 1295 (1988).
- [27] G. Pickett. *Cooling metals to the microkelvin regime, then and now*. Physica B: Condensed Matter **280**, 467 (2000).
- [28] A. S. Oja and O. V. Lounasmaa. *Nuclear magnetic ordering in simple metals at positive and negative nanokelvin temperatures*. Rev. Mod. Phys. **69**, 1 (1997).

- [29] N. Kurti. *Cooling by Adiabatic Demagnetization of Nuclear Spins*. *Cryogenics* **1**, 2 (1960).
- [30] T. A. Jyrkkö, M. T. Huiku, O. V. Lounasmaa, K. Siemensmeyer, K. Kakurai, M. Steiner, K. N. Clausen, and J. K. Kjems. *Observation of Nuclear Antiferromagnetic Order in Copper by Neutron Diffraction at Nanokelvin Temperatures*. *Phys. Rev. Lett.* **60**, 2418 (1988).
- [31] A. C. Clark, K. K. Schwarzwälder, T. Bandi, D. Maradan, and D. M. Zumbühl. *Method for cooling nanostructures to microkelvin temperatures*. *Rev. Sci. Instrum.* **81**, 103904 (2010).
- [32] L. Casparis, M. Meschke, D. Maradan, A. C. Clark, C. P. Scheller, K. K. Schwarzwälder, J. P. Pekola, and D. M. Zumbühl. *Metallic Coulomb blockade thermometry down to 10 mK and below*. *Rev. Sci. Instrum.* **83**, 083903 (2012).
- [33] M. Palma, D. Maradan, L. Casparis, T.-M. Liu, F. N. M. Froning, and D. M. Zumbühl. *Magnetic cooling for microkelvin nanoelectronics on a cryofree platform*. *Rev. Sci. Instrum.* **88**, 043902 (2017).
- [34] C. P. Scheller, S. Heizmann, K. Bedner, D. Giss, M. Meschke, D. M. Zumbühl, J. D. Zimmerman, and A. C. Gossard. *Silver-epoxy microwave filters and thermalizers for millikelvin experiments*. *Appl. Phys. Lett.* **104**, 211106 (2014).
- [35] W. P. Halperin. *The impact of helium shortages on basic research*. *Nat. Phys.* **10**, 467 (2014).
- [36] D. Butler. *Qatar blockade hits helium supply*. *Nature News* **547**, 16 (2017).
- [37] G. Batey, A. Casey, M. N. Cuthbert, A. J. Matthews, J. Saunders, and A. Shiba-hara. *A microkelvin cryogen-free experimental platform with integrated noise thermometry*. *New J. Phys.* **15**, 113034 (2013).

- [38] A. Casey, F. Arnold, L. V. Levitin, C. P. Lusher, J. Nyéki, J. Saunders, A. Shibahara, H. v. d. Vliet, B. Yager, D. Drung, T. Schurig, G. Batey, M. N. Cuthbert, and A. J. Matthews. *Current Sensing Noise Thermometry: A Fast Practical Solution to Low Temperature Measurement*. *J. Low Temp. Phys.* **175**, 764 (2014).
- [39] I. Todoshchenko, J.-P. Kaikkonen, R. Blaauwgeers, P. J. Hakonen, and A. Savin. *Dry demagnetization cryostat for sub-millikelvin helium experiments: Refrigeration and thermometry*. *Rev. Sci. Instrum.* **85**, 085106 (2014).
- [40] D. I. Bradley, R. E. George, D. Gunnarsson, R. P. Haley, H. Heikkinen, Y. A. Pashkin, J. Penttilä, J. R. Prance, M. Prunnila, L. Roschier, and M. Sarsby. *Nanoelectronic primary thermometry below 4 mK*. *Nat. Commun.* **7**, 10455 (2016).
- [41] D. I. Bradley, A. M. Guenault, D. Gunnarsson, R. P. Haley, S. Holt, A. T. Jones, Y. A. Pashkin, J. Penttilä, J. R. Prance, M. Prunnila, and L. Roschier. *On-chip magnetic cooling of a nanoelectronic device*. *Sci. Rep.* **7**, 45566 (2017).
- [42] M. Nahum and J. M. Martinis. *Ultrasensitive-hot-electron microbolometer*. *Appl. Phys. Lett.* **63**, 3075 (1993).
- [43] A. V. Feshchenko, L. Casparis, I. M. Khaymovich, D. Maradan, O.-P. Saira, M. Palma, M. Meschke, J. P. Pekola, and D. M. Zumbühl. *Tunnel-Junction Thermometry Down to Millikelvin Temperatures*. *Phys. Rev. Applied* **4**, 034001 (2015).
- [44] J. Engert, J. Beyer, D. Drung, A. Kirste, and M. Peters. *A Noise Thermometer for Practical Thermometry at Low Temperatures*. *Int. J. Thermophys.* **28**, 1800 (2007).
- [45] J. Engert, D. Heyer, J. Beyer, and H. J. Barthelmeß. *Noise thermometry at low temperatures: MFFT measurements between 1.6 K and 1 mK*. *J. Phys. Conf. Ser.* **400**, 052003 (2012).

- [46] J. Beyer, D. Drung, A. Kirste, J. Engert, A. Netsch, A. Fleischmann, and C. Enss. *A Magnetic-Field-Fluctuation Thermometer for the mK Range Based on SQUID-Magnetometry*. IEEE Trans. Appl. Supercond. **17**, 760 (2007).
- [47] R. Mueller, C. Buchal, H. Folle, M. Kubota, and F. Pobell. *A double-stage nuclear demagnetization refrigerator*. Cryogenics **20**, 395 (1980).
- [48] NOSV Cu-ETP1 grade, Aurubius AG, Hamburg (Germany).
- [49] A. B. Zorin. *The thermocoax cable as the microwave frequency filter for single-electron circuits*. Rev. Sci. Instrum. **66**, 4296 (1995).
- [50] N. S. Lawson. *A simple heat switch for use at millikelvin temperatures*. Cryogenics **22**, 121 (1982).
- [51] BlueFors Cryogenics Oy Ltd., Helsinki, Finland.
- [52] D. Rothfuss, A. Reiser, A. Fleischmann, and C. Enss. *Noise thermometry at ultra low temperatures*. Appl. Phys. Lett. **103**, 052605 (2013).
- [53] J. B. Johnson. *Thermal Agitation of Electricity in Conductors*. Phys. Rev. **32**, 97 (1928).
- [54] H. Nyquist. *Thermal Agitation of Electric Charge in Conductors*. Phys. Rev. **32**, 110 (1928).
- [55] T. Varpula and T. Poutanen. *Magnetic field fluctuations arising from thermal motion of electric charge in conductors*. J. Appl. Phys. **55**, 4015 (1984).
- [56] F. C. Wellstood, C. Urbina, and J. Clarke. *Low-frequency noise in dc superconducting quantum interference devices below 1 K*. Appl. Phys. Lett. **50**, 772 (1987).
- [57] K. Gloos, C. Mitschka, F. Pobell, and P. Smeibidl. *Thermal conductivity of normal and superconducting metals*. Cryogenics **30**, 14 (1990).

- [58] S. Brunauer, P. H. Emmett, and E. Teller. *Adsorption of Gases in Multimolecular Layers*. J. Am. Chem. Soc. **60**, 309 (1938).
- [59] B. M. Abraham, O. Brandt, Y. Eckstein, J. B. Ketterson, M. Kuchnir, and P. Roach. *Heat Capacity of Diluted Cerium Magnesium Nitrate and Its Potential for the Production of Very Low Temperatures*. Phys. Rev. **187**, 273 (1969).
- [60] F. Giazotto, T. T. Heikkilä, A. Luukanen, A. M. Savin, and J. P. Pekola. *Opportunities for mesoscopics in thermometry and refrigeration: Physics and applications*. Rev. Mod. Phys. **78**, 217 (2006).
- [61] S. Gasparinetti, F. Deon, G. Biasiol, L. Sorba, F. Beltram, and F. Giazotto. *Probing the local temperature of a two-dimensional electron gas microdomain with a quantum dot: Measurement of electron-phonon interaction*. Phys. Rev. B **83**, 201306 (2011).
- [62] A. Mavalankar, S. J. Chorley, J. Griffiths, G. A. C. Jones, I. Farrer, D. A. Ritchie, and C. G. Smith. *A non-invasive electron thermometer based on charge sensing of a quantum dot*. Appl. Phys. Lett. **103**, 133116 (2013).
- [63] D. Maradan, L. Casparis, T.-M. Liu, D. E. F. Biesinger, C. P. Scheller, D. M. Zumbühl, J. D. Zimmerman, and A. C. Gossard. *GaAs Quantum Dot Thermometry Using Direct Transport and Charge Sensing*. J. Low Temp. Phys. **175**, 784 (2014).
- [64] M. Nahum, T. M. Eiles, and J. M. Martinis. *Electronic microrefrigerator based on a normal - insulator - superconductor tunnel junction*. Appl. Phys. Lett. **65**, 3123 (1994).
- [65] A. V. Feshchenko, J. V. Koski, and J. P. Pekola. *Experimental realization of a Coulomb blockade refrigerator*. Phys. Rev. B **90**, 201407(R) (2014).
- [66] A. M. Clark, A. Williams, S. T. Ruggiero, M. L. van den Berg, and J. N. Ullom. *Practical electron-tunneling refrigerator*. Appl. Phys. Lett. **84**, 625 (2004).

- [67] N. A. Miller, G. C. O’Neil, J. A. Beall, G. C. Hilton, K. D. Irwin, D. R. Schmidt, L. R. Vale, and J. N. Ullom. *High resolution x-ray transition-edge sensor cooled by tunnel junction refrigerators*. Appl. Phys. Lett. **92**, 163501 (2008).
- [68] J. P. Pekola, K. P. Hirvi, J. P. Kauppinen, and M. A. Paalanen. *Thermometry by Arrays of Tunnel Junctions*. Phys. Rev. Lett. **73**, 2903 (1994).
- [69] P. Dubos, H. Courtois, B. Pannetier, F. K. Wilhelm, A. D. Zaikin, and G. Schön. *Josephson critical current in a long mesoscopic S-N-S junction*. Phys. Rev. B **63**, 064502 (2001).
- [70] L. Spietz, K. W. Lehnert, I. Siddiqi, and R. J. Schoelkopf. *Primary Electronic Thermometry Using the Shot Noise of a Tunnel Junction*. Science **300**, 1929 (2003).
- [71] L. Spietz, R. J. Schoelkopf, and P. Pari. *Shot noise thermometry down to 10 mK*. Appl. Phys. Lett. **89**, 183123 (2006).
- [72] L. Spietz. *The Shot Noise Thermometer*. PhD Thesis, Yale University, Connecticut, United States (2006).
- [73] M. M. Leivo, J. P. Pekola, and D. V. Averin. *Efficient Peltier refrigeration by a pair of normal metal/insulator/superconductor junctions*. Appl. Phys. Lett. **68**, 1996 (1996).
- [74] P. A. Fisher, J. N. Ullom, and M. Nahum. *High-power on-chip microrefrigerator based on a normal-metal/insulator/superconductor tunnel junction*. Appl. Phys. Lett. **74**, 2705 (1999).
- [75] J. T. Muhonen, M. Meschke, and J. P. Pekola. *Micrometre-scale refrigerators*. Rep. Prog. Phys. **75**, 046501 (2012).
- [76] A. Stern. *Non-Abelian states of matter*. Nature **464**, 187 (2010).

- [77] O. E. Dial, M. D. Shulman, S. P. Harvey, H. Bluhm, V. Umansky, and A. Yacoby. *Charge Noise Spectroscopy Using Coherent Exchange Oscillations in a Singlet-Triplet Qubit*. Phys. Rev. Lett. **110**, 146804 (2013).
- [78] H. Paik, D. I. Schuster, L. S. Bishop, G. Kirchmair, G. Catelani, A. P. Sears, B. R. Johnson, M. J. Reagor, L. Frunzio, L. I. Glazman, S. M. Girvin, M. H. Devoret, and R. J. Schoelkopf. *Observation of High Coherence in Josephson Junction Qubits Measured in a Three-Dimensional Circuit QED Architecture*. Phys. Rev. Lett. **107**, 240501 (2011).
- [79] M. Tinkham. *Introduction to superconductivity* (Dover, New York, 1996), 2nd Edition.
- [80] J. P. Pekola, V. F. Maisi, S. Kafanov, N. Chekurov, A. Kemppinen, Y. A. Pashkin, O.-P. Saira, M. Möttönen, and J. S. Tsai. *Environment-Assisted Tunneling as an Origin of the Dynes Density of States*. Phys. Rev. Lett. **105**, 026803 (2010).
- [81] R. C. Dynes, V. Narayanamurti, and J. P. Garno. *Direct Measurement of Quasiparticle-Lifetime Broadening in a Strong-Coupled Superconductor*. Phys. Rev. Lett. **41**, 1509 (1978).
- [82] H. Courtois, S. Rajauria, P. Gandit, F. W. J. Hekking, and B. Pannetier. *Inherent Thermometry in a Hybrid Superconducting Tunnel Junction*. J. Low Temp. Phys. **153**, 325 (2008).
- [83] T. Greibe, M. P. V. Stenberg, C. M. Wilson, T. Bauch, V. S. Shumeiko, and P. Delsing. *Are "Pinholes" the Cause of Excess Current in Superconducting Tunnel Junctions? A Study of Andreev Current in Highly Resistive Junctions*. Phys. Rev. Lett. **106**, 097001 (2011).
- [84] H. Jung, Y. Kim, K. Jung, H. Im, Y. A. Pashkin, O. Astafiev, Y. Nakamura, H. Lee, Y. Miyamoto, and J. S. Tsai. *Potential barrier modification and interface*

- states formation in metal-oxide-metal tunnel junctions.* Phys. Rev. B **80**, 125413 (2009).
- [85] M. R. Nevala, S. Chaudhuri, J. Halkosaari, J. T. Karvonen, and I. J. Maasilta. *Sub-micron normal-metal/insulator/superconductor tunnel junction thermometer and cooler using Nb.* Appl. Phys. Lett. **101**, 112601 (2012).
- [86] S. Chaudhuri, M. R. Nevala, and I. J. Maasilta. *Niobium nitride-based normal metal-insulator-superconductor tunnel junction microthermometer.* Appl. Phys. Lett. **102**, 132601 (2013).
- [87] D. J. van Woerkom, A. Geresdi, and L. P. Kouwenhoven. *One minute parity lifetime of a NbTiN Cooper-pair transistor.* Nat. Phys. **11**, 547 (2015).
- [88] H. Q. Nguyen, M. Meschke, H. Courtois, and J. P. Pekola. *Sub-50 mK electronic cooling with large-area superconducting tunnel junctions.* Phys. Rev. Appl. **2**, 054001 (2014).
- [89] O.-P. Saira, A. Kemppinen, V. F. Maisi, and J. P. Pekola. *Vanishing quasiparticle density in a hybrid Al/Cu/Al single-electron transistor.* Phys. Rev. B **85**, 012504 (2012).
- [90] J. M. Hergenrother, J. G. Lu, M. T. Tuominen, D. C. Ralph, and M. Tinkham. *Photon-activated switch behavior in the single-electron transistor with a superconducting island.* Phys. Rev. B **51**, 9407 (1995).
- [91] F. W. J. Hekking and Y. V. Nazarov. *Subgap conductivity of a superconductor-normal-metal tunnel interface.* Phys. Rev. B **49**, 6847 (1994).
- [92] T. A. Fulton and G. J. Dolan. *Observation of single-electron charging effects in small tunnel junctions.* Phys. Rev. Lett. **59**, 109 (1987).
- [93] M. Steinacher. Low Noise/High Stability I to V converter SP893, Electronics Lab, Physics Department, University of Basel, Switzerland.

- [94] J. Jochum, C. Mears, S. Golwala, B. Sadoulet, J. P. Castle, M. F. Cunningham, O. B. Drury, M. Frank, S. E. Labov, F. P. Lipschultz, H. Netel, and B. Neuhauser. *Modeling the power flow in normal conductor-insulator-superconductor junctions*. J. Appl. Phys. **83**, 3217 (1998).
- [95] V. F. Maisi, O.-P. Saira, Y. A. Pashkin, J. S. Tsai, D. V. Averin, and J. P. Pekola. *Real-Time Observation of Discrete Andreev Tunneling Events*. Phys. Rev. Lett. **106**, 217003 (2011).
- [96] T. Aref, V. F. Maisi, M. V. Gustafsson, P. Delsing, and J. P. Pekola. *Andreev tunneling in charge pumping with SINIS turnstiles*. Europhys. Lett. **96**, 37008 (2011).
- [97] P. J. de Visser, J. J. A. Baselmans, P. Diener, S. J. C. Yates, A. Endo, and T. M. Klapwijk. *Number Fluctuations of Sparse Quasiparticles in a Superconductor*. Phys. Rev. Lett. **106**, 167004 (2011).
- [98] H. S. Knowles, V. F. Maisi, and J. P. Pekola. *Probing quasiparticle excitations in a hybrid single electron transistor*. Appl. Phys. Lett. **100**, 262601 (2012).
- [99] A. V. Timofeev, C. P. Garcia, N. B. Kopnin, A. M. Savin, M. Meschke, F. Giazotto, and J. P. Pekola. *Recombination-Limited Energy Relaxation in a Bardeen-Cooper-Schrieffer Superconductor*. Phys. Rev. Lett. **102**, 017003 (2009).
- [100] J. P. Pekola, A. J. Manninen, M. M. Leivo, K. Arutyunov, J. K. Suoknuuti, T. I. Suppala, and B. Collaudin. *Microrefrigeration by quasiparticle tunnelling in NIS and SIS junctions*. Physica B **280**, 485 (2000).
- [101] J. M. Martinis, K. B. Cooper, R. McDermott, M. Steffen, M. Ansmann, K. D. Osborn, K. Cicak, S. Oh, D. P. Pappas, R. W. Simmonds, and C. C. Yu. *Decoherence in Josephson Qubits from Dielectric Loss*. Phys. Rev. Lett. **95**, 210503 (2005).

- [102] M. V. Fistul. *Resonant enhancement of macroscopic quantum tunneling in Josephson junctions: Influence of coherent two-level systems*. Phys. Rev. B **92**, 014505 (2015).
- [103] C. Wang, C. Axline, Y. Y. Gao, T. Brecht, Y. Chu, L. Frunzio, M. H. Devoret, and R. J. Schoelkopf. *Surface participation and dielectric loss in superconducting qubits*. Appl. Phys. Lett. **107**, 162601 (2015).
- [104] J. B. Chang, M. R. Vissers, A. D. Córcoles, M. Sandberg, J. Gao, D. W. Abraham, J. M. Chow, J. M. Gambetta, M. Beth Rothwell, G. A. Keefe, M. Steffen, and D. P. Pappas. *Improved superconducting qubit coherence using titanium nitride*. Appl. Phys. Lett. **103**, 012602 (2013).
- [105] L. Zeng, D. T. Tran, C.-W. Tai, G. Svensson, and E. Olsson. *Atomic structure and oxygen deficiency of the ultrathin aluminium oxide barrier in Al/AlO_x/Al Josephson junctions*. Sci. Rep. **6**, 29679 (2016).
- [106] S. Oh, K. Cicak, J. S. Kline, M. A. Sillanpää, K. D. Osborn, J. D. Whittaker, R. W. Simmonds, and D. P. Pappas. *Elimination of two level fluctuators in superconducting quantum bits by an epitaxial tunnel barrier*. Phys. Rev. B **74**, 100502 (2006).
- [107] J. Aumentado, M. W. Keller, J. M. Martinis, and M. H. Devoret. *Nonequilibrium Quasiparticles and 2e Periodicity in Single-Cooper-Pair Transistors*. Phys. Rev. Lett. **92**, 066802 (2004).
- [108] H. Q. Nguyen, T. Aref, V. J. Kauppila, M. Meschke, C. B. Winkelmann, H. Courtois, and J. P. Pekola. *Trapping hot quasi-particles in a high-power superconducting electronic cooler*. New Journal of Physics **15**, 085013 (2013).
- [109] C. C. Chi and J. Clarke. *Enhancement of the energy gap in superconducting aluminum by tunneling extraction of quasiparticles*. Phys. Rev. B **20**, 4465 (1979).

- [110] M. G. Blamire, E. C. G. Kirk, J. E. Evetts, and T. M. Klapwijk. *Extreme critical-temperature enhancement of Al by tunneling in Nb/AlO_x/Al/AlO_x/Nb tunnel junctions*. Phys. Rev. Lett. **66**, 220 (1991).
- [111] M. Taupin, I. M. Khaymovich, M. Meschke, A. S. Mel'nikov, and J. P. Pekola. *Tunable quasiparticle trapping in Meissner and vortex states of mesoscopic superconductors*. Nat. Commun. **7**, 10977 (2016).
- [112] F. W. J. Hekking and Y. V. Nazarov. *Subgap conductivity of a superconductor-normal-metal tunnel interface*. Phys. Rev. B **49**, 6847 (1994).
- [113] C. W. J. Beenakker. *Quantum transport in semiconductor-superconductor microjunctions*. Phys. Rev. B **46**, 12841 (1992).
- [114] I. K. Marmoros, C. W. J. Beenakker, and R. A. Jalabert. *Three signatures of phase-coherent Andreev reflection*. Phys. Rev. B **48**, 2811 (1993).
- [115] J. Melsen and C. Beenakker. *Reflectionless tunneling through a double-barrier NS junction*. Physica B: Condensed Matter **203**, 219 (1994).
- [116] A. Kastalsky, A. W. Kleinsasser, L. H. Greene, R. Bhat, F. P. Milliken, and J. P. Harbison. *Observation of pair currents in superconductor-semiconductor contacts*. Phys. Rev. Lett. **67**, 3026 (1991).
- [117] P. H. C. Magnée, N. van der Post, P. H. M. Kooistra, B. J. van Wees, and T. M. Klapwijk. *Enhanced conductance near zero voltage bias in mesoscopic superconductor-semiconductor junctions*. Phys. Rev. B **50**, 4594 (1994).
- [118] B. Al'tshuler, A. Aronov, M. Gershenson, and Y. V. Sharvin. *Quantum effects in disordered metal films*. Sov. Sci. Rev. Sect. A. : Phys. Rev. **9**, 223 (1987).
- [119] W. Belzig, C. Bruder, and G. Schön. *Local density of states in a dirty normal metal connected to a superconductor*. Phys. Rev. B **54**, 9443 (1996).

-
- [120] B. Crouzy, E. Bascones, and D. A. Ivanov. *Minigap in a superconductor–normal metal junction with paramagnetic impurities*. Phys. Rev. B **72**, 092501 (2005).
- [121] G. Fagas, G. Tkachov, A. Pfund, and K. Richter. *Geometrical enhancement of the proximity effect in quantum wires with extended superconducting tunnel contacts*. Phys. Rev. B **71**, 224510 (2005).
- [122] A. Altland, B. D. Simons, and D. T. Semchuk. *Field theory of mesoscopic fluctuations in superconductor-normal-metal systems*. Adv. Phys. **49**, 321 (2000).
- [123] E. Scheer, W. Belzig, Y. Naveh, M. H. Devoret, D. Esteve, and C. Urbina. *Proximity Effect and Multiple Andreev Reflections in Gold Atomic Contacts*. Phys. Rev. Lett. **86**, 284 (2001).
- [124] G. P. Antonio Barone. *Physics and Applications of the Josephson Effect* (Wiley, 1982).
- [125] S. Shapiro. *Josephson Currents in Superconducting Tunneling: The Effect of Microwaves and Other Observations*. Phys. Rev. Lett. **11**, 80 (1963).
- [126] C. C. Grimes and S. Shapiro. *Millimeter-Wave Mixing with Josephson Junctions*. Phys. Rev. **169**, 397 (1968).
- [127] C. Beenakker. *Andreev Billiards*, 131–174 (Springer Berlin Heidelberg, Berlin, Heidelberg, 2005).
- [128] W. Belzig, F. K. Wilhelm, C. Bruder, G. Schön, and A. D. Zaikin. *Quasiclassical Green's function approach to mesoscopic superconductivity*. Superlattices Microstruct. **25**, 1251 (1999).
- [129] A. A. Golubov and M. Y. Kupriyanov. *Theoretical investigation of Josephson tunnel junctions with spatially inhomogeneous superconducting electrodes*. J. Low Temp. Phys. **70**, 83 (1988).

-
- [130] M. Tinkham. *Effect of Fluxoid Quantization on Transitions of Superconducting Films*. Phys. Rev. **129**, 2413 (1963).
- [131] F. E. Harper and M. Tinkham. *The Mixed State in Superconducting Thin Films*. Phys. Rev. **172**, 441 (1968).
- [132] S. Chesi and D. Loss. *Quantum Hall ferromagnetic states and spin-orbit interactions in the fractional regime*. Phys. Rev. Lett. **101**, 146803 (2008).
- [133] Y. Oreg, G. Refael, and F. von Oppen. *Helical Liquids and Majorana Bound States in Quantum Wires*. Phys. Rev. Lett. **105**, 177002 (2010).
- [134] L. Casparis, M. Meschke, D. Maradan, A. C. Clark, C. P. Scheller, K. K. Schwarzwälder, J. P. Pekola, and D. M. Zumbühl. *Metallic Coulomb blockade thermometry down to 10 mK and below*. Rev. Sci. Instrum. **83**, 083903 (2012).
- [135] Z. Iftikhar, A. Anthore, S. Jezouin, F. D. Parmentier, Y. Jin, A. Cavanna, A. Ouerghi, U. Gennser, and F. Pierre. *Primary thermometry triad at 6 mK in mesoscopic circuits*. Nat. Commun. **7**, 12908 (2016).
- [136] J. P. Pekola, K. P. Hirvi, J. P. Kauppinen, and M. A. Paalanen. *Thermometry by Arrays of Tunnel Junctions*. Phys. Rev. Lett. **73**, 2903 (1994).
- [137] M. Meschke, J. P. Pekola, F. Gay, R. E. Rapp, and H. Godfrin. *Electron Thermalization in Metallic Islands Probed by Coulomb Blockade Thermometry*. J. Low Temp. Phys. **134**, 1119 (2004).
- [138] C. Ciccarelli, R. P. Champion, B. L. Gallagher, and A. J. Ferguson. *Intrinsic magnetic refrigeration of a single electron transistor*. Appl. Phys. Lett. **108**, 053103 (2016).
- [139] A. V. Feshchenko, M. Meschke, D. Gunnarsson, M. Prunnila, L. Roschier, J. S. Penttilä, and J. P. Pekola. *Primary Thermometry in the Intermediate Coulomb Blockade Regime*. J. Low Temp. Phys. **173**, 36 (2013).

-
- [140] G.-L. Ingold and Y. V. Nazarov. *Charge tunneling rates in ultrasmlal junctions* (in Single Charge Tunneling: Coulomb Blockade Phenomena In Nanostructures, 1992).
- [141] Basel Electronics Lab, Physics Departement, University of Basel, Switzerland.
- [142] E. T. Swartz and R. O. Pohl. *Thermal boundary resistance*. Rev. Mod. Phys. **61**, 605 (1989).
- [143] A. T. Lee. *Broadband cryogenic preamplifiers incorporating GaAs MESFETs for use with low-temperature particle detectors*. Rev. Sci. Instrum. **60**, 3315 (1989).
- [144] L. Roschier, D. Gunnarsson, M. Meschke, A. Savin, J. S. Penttilä, and M. Prunnila. *Effect of on-chip filter on Coulomb blockade thermometer*. J. Phys. Conf. Ser. **400**, 052029 (2012).
- [145] O. Zilberberg, A. Carmi, and A. Romito. *Measuring cotunneling in its wake*. Phys. Rev. B **90**, 205413 (2014).
- [146] D. Bischoff, M. Eich, O. Zilberberg, C. Rössler, T. Ihn, and K. Ensslin. *Measurement Back-Action in Stacked Graphene Quantum Dots*. Nano Lett. **15**, 6003 (2015).
- [147] R. L. Willett, C. Nayak, K. Shtengel, L. N. Pfeiffer, and K. W. West. *Magnetic-Field-Tuned Aharonov-Bohm Oscillations and Evidence for Non-Abelian Anyons at $\nu = 5/2$* . Phys. Rev. Lett. **111**, 186401 (2013).
- [148] J. Klinovaja and D. Loss. *Integer and fractional quantum Hall effect in a strip of stripes*. Eur. Phys. J. B **87**, 171 (2014).
- [149] J. Klinovaja, Y. Tserkovnyak, and D. Loss. *Integer and fractional quantum anomalous Hall effect in a strip of stripes model*. Phys. Rev. B **91**, 085426 (2015).

-
- [150] A. G. Huibers, J. A. Folk, S. R. Patel, C. M. Marcus, C. I. Duruöz, and J. S. Harris. *Low-Temperature Saturation of the Dephasing Time and Effects of Microwave Radiation on Open Quantum Dots*. Phys. Rev. Lett. **83**, 5090 (1999).
- [151] I. G. Rau, S. Amasha, M. Grobis, R. M. Potok, H. Shtrikman, and D. Goldhaber-Gordon. *Nonsaturating Dephasing Time at Low Temperature in an Open Quantum Dot*. arXiv:1210.0087 (2012).
- [152] A. J. Keller, S. Amasha, I. Weymann, C. P. Moca, I. G. Rau, J. A. Katine, H. Shtrikman, G. Zarand, and D. Goldhaber-Gordon. *Emergent $SU(4)$ Kondo physics in a spin-charge-entangled double quantum dot*. Nat. Phys. **10**, 145 (2014).

List of Figures

- 1.1 History of refrigeration techniques developed in the past 160 years. The graph reproduces a previous graph shown in Ref. [1], but we add the experimental results obtained with a nuclear refrigeration network. Note that the network of nuclear refrigerator is not an entirely new technique, but rather is adapting nuclear magnetic demagnetization for the specific needs of cooling nanoelectronic devices. 2
- 1.2 (a) Lowest temperatures measured in the past 30 years in NIS junctions.
 (b) Lowest temperatures measured in past 30 years in CBTs. The dashed blue lines indicate the lowest temperatures reached for NIS junctions and CBTs 8
- 2.1 Schematic of the nuclear demagnetization stage. The measurement leads are thermalized with Ag powder sinters (*top right picture*, scale bar: 5 mm) in the mixing chamber (MC, blue) and pass through C-shaped Al heat switches (green) to the Cu plates. The gradiometer of the noise thermometer as well as the (L)CMN thermometers are positioned in a region of cancelled magnetic field between the MC and the NR stage. The gradiometer is double-shielded by a Nb tube and an outer NbTi tube (red). *Middle right inset*: photograph of the gradiometer pick-up coil made from insulated Nb wire with 100 μm diameter. The 2x20 turns are wound non-inductively on a high-purity silver wire which is spot-welded to a NR. Scale bar: 2 mm. *Lower inset*: schematic cross section through the network of 16 parallel NRs. Each NR is 2 mol of Cu (99.99% Cu, low- H_2 content [48], RRR \sim 500) and consists of two half-plates, spot-welded together at the top and bottom. Each half-plate is of dimension $3.4 \times 0.17 \times 12 \text{ cm}^3$ 14
- 2.2 Power spectral density $S_\phi(0, T_{\text{MFFT}})$ of the magnetic flux noise, in units of the flux quantum ϕ_0 , at various NR temperatures. The light gray solid curves are fits using Eq. (2.2) which are converted to T_{MFFT} as described in the text using the reference spectrum at $T_{\text{ref}} = 4.2 \text{ K}$. The noise peaks become more visible at lower temperatures where the thermal noise becomes smaller. The SQUID noise shown here in grey is from a similar SQUID with the inputs shorted, not from the SQUID used to measure the MFFT. 17

- 2.3 Warm-up curves: (a) Inverse of T_s measured with the MFFT versus time during the warm up at 80 mT (red squares) and 200 mT (orange squares) after AND. The linear fits (black dashed lines) reveal extrapolated electron temperatures $T_{\text{ex}} = 126/280 \mu\text{K}$ at the beginning of the warm up and heat leaks of $\dot{Q} = 0.9/1.16 \text{ nW/mol}$ for 80 mT and 200 mT, respectively. The solid blue curves are the fits to the heat flow model (see main text) with $\dot{Q}_s = 6\%$ at 80 mT and 18% at 200 mT of the total static heat leak. (b) Precool and warm up (PW) measurements: T_s^{-1} during warm up, from MFFT, CMN and LCMN thermometers versus the time after opening the heat switches at $B = 0.5 \text{ T}$, resulting in $\dot{Q} = 1.2/2.0/4.8 \text{ nW/mol}$, respectively. Inset: static heat leak \dot{Q} to the nuclear stage per mol of Cu, measured with the MFFT at various B -fields, extracted using Eq. (2.3) after AND (black crosses) and after PW (green circles). 23
- 2.4 Temperature measured by the noise thermometer T_{MFFT} versus temperature of the nuclear stage $T_{\text{e,Cu}}$. Above 7 mK, $T_{\text{e,Cu}}$ is measured with a calibrated RuO_2 thermometer sitting on the MC (red squares). In this temperature range the MC and the Cu stage are well thermally coupled. For temperatures below 7 mK, $T_{\text{e,Cu}}$ is extracted from warm ups after AND (blue squares) (see text and Fig. 3.1(a)). The black dotted line represents $T_{\text{MFFT}} = T_{\text{e,Cu}}$. *Inset*: the efficiency ξ as function of the final magnetic fields B_f . The dashed curves show simulations of the AND process, carried out at two different ramp speeds. The markers show the efficiency extracted from different AND runs as labeled. 25
- 2.5 Scheme of the dilution unit together with NRs. Compared to Ref. [3] we doubled the number of sinters per lead, the diameter of the silver wires and the amount of Cu per plate. Below the dashed red line, the socket design for future transport experiments is illustrated. The abbreviations in the figure are bandwidth (BW), critical magnetic field (B_c) and the electrical ground (GND). 29
- 2.6 (a) shows the temperature of the CMN thermometer and MFFT as function of the time during the precooling at 9 T. The dashed line indicates the behavior of the precooling temperature predicted from the theory [1]. (b) T_{MFFT} versus time for warm ups at 80 mT and 200 mT. The dashed line points out the hold time below 1 mK, which is important for transport experiments. 30
- 2.7 \dot{Q} at various B -fields measured with CMN and LCMN thermometers. The static heat leaks \dot{Q} are extracted with PW and AND methods introduced in the main text. 30

- 2.8 (a) inverse of T_s measured with the CMN thermometer versus time during the warm up at 80 mT and 200 mT. The warm up curves are plotted in semi-logarithmic scale, for this reason the lines appear as curves. The fit to Eq. (2) gives an extrapolated Cu electron temperature $T_{\text{ex}} = 105/268 \mu\text{K}$ and static heat leak $\dot{Q} = 2.6/3.1 \text{ nW/mol}$ for 80/200 mT, respectively. The solid blue line shows the heat flow model with $\dot{Q}_s = 9/10\%$ of \dot{Q} . (b) shows the same warm up curves for the LCMN thermometer. From the fit to Eq. (2) we extract $T_{\text{ex}} = 160/246 \mu\text{K}$ and $\dot{Q} = 2.1/3.6 \text{ nW/mol}$ for 80/200 mT, respectively. The heat flow equation reveals $\dot{Q}_s = 11/22\%$ of \dot{Q} for 80/200 mT, respectively. 32
- 2.9 The static heat leak \dot{Q} measured with MFFT for various magnetic fields and for three different socket designs: no socket, Ag-epoxy socket and sapphire socket. The dashed lines are guides for the eyes 34
- 2.10 Temperature measured by MFFT versus the temperature of the nuclear stage T_{Cu} with T_{Cu} extracted as in Fig. 4 of the main text. We compare two different gradiometer designs: old design with Ag-epoxy socket and improved design realized for no socket and sapphire socket. 36
- 3.1 Molar nuclear spin entropy at fixed magnetic fields of $B_i = 9 \text{ T}$ (red curve) and $B_f = 80 \text{ mT}$ (blue curve) as a function of the nuclear temperature T_n . After ramping up the B -field up to 9 T, we wait and cool in the point a. During the precooling, we move along the red curve from point a to b, until we reach $T_i \sim 10 \text{ mK}$. Note that for other magnetic fields, e.g. 4 T and 2 T, the molar entropy curves are shifted to the left compared to the one at 9 T, indicating lower nuclear temperatures are required to obtain the same value of S_n after precooling. During demagnetization, we move from b to c, indicated by the black arrow, the point c is located on the entropy curve at $B_f = 80 \text{ mT}$ with abscissa $T_f \sim 90 \mu\text{K}$ 39
- 3.2 A schematic showing the different degrees of freedom present in the Cu refrigerant. Electrons and phonons interact through \dot{Q}_{e-ph} , while electrons and nuclei exchange heat via \dot{Q}_{en} . A parasitic heat leak \dot{Q}_{par} is introduced in the system through the electronic degree of freedom. The direct interaction between phonons and nuclei is negligible. 42
- 3.3 Calculated T_e and T_n as a function of the magnetic field during the demagnetization. The red squares indicate T_{MFFT} during the demagnetization, while the black square is the temperature measured at static field $B_f = 0.08 \text{ T}$. The dashed line indicates the calculated nuclear temperature for the ideal adiabatic process 45
- 3.4 Efficiency as a function of the magnetic field. The orange line is the calculated efficiency for a standard AND, while the light blue line is the calculated efficiency obtained by doubling the ramp-rates. 46
- 3.5 The heat switch magnet as a function of the demagnetization magnet during the refrigeration cycle. The different parts of the refrigeration path are indicated by numbers. 48
- 4.1 Influence of the Dynes parameter on the NIS thermometer. Measurement of γ and the tunneling resistance R_T 52

4.2	SEM picture of the NIS device and schematic of the experimental setup.	55
4.3	Measured I - V 's of the NIS device at different temperatures along with theoretical fits.	57
4.4	Updated scheme of dilution unit together with NR stage.	61
4.5	Comparison of theoretical deviations for the NIS thermometer measuring current or conductance.	63
4.6	Thermal diagram of the NIS thermometer.	64
5.1	(a) Scanning electron micrograph of a co-fabricated NIS junction together with a schematic of the experimental setup. The inset shows a zoom-in of the junction. (b) A cross section of the NIS junction. (c) Zooms of the I - V curves in the sub-gap region for various temperatures. The black line indicates the double Fermi function fits used to extract T_{step} . To reduce the error on T_{step} the fit is performed on 10 consecutive I - V curves taken at the same temperature and we use the mean value as $\langle T_{\text{step}} \rangle$ and its standard deviation as error bar. The I - V characteristic for large current range is shown in the lower inset of Fig.1.(c). (d) T_{step} and T_{slope} as a function of T_{Cu} . The upper inset shows the region of the I - V curve where the semi-logarithmic fit is applied. The lower inset shows T_{step} and T_{slope} as a function of perpendicular magnetic fields.	70
5.2	(a) I - V curves of the NIS_2 for various thermal cycles. (b-d) I - V curves for two different devices at Cu thickness of 20 nm, 50 nm and 150 nm, respectively.(e) the upper graph shows the Dynes parameter as a function of d_{Cu} and the lower graph shows the amplitude of the ZBS as a function of Cu thickness. Note that for both graphs the points at 50 nm and 150 nm are horizontally offset by 5 nm to avoid the overlap of the markers.	73
5.3	(a-d) The logarithm of the absolute of the differential conductance as a function of the in plane magnetic field and voltage bias for various thicknesses of Cu. The full colour lines in (a-d) indicate the parabolic trajectories describe by the steps in B_{\parallel} , they are shifted from the dashed lines by the Zeeman energy. (e) the thickness dependence of the curvature of the steps in-plane magnetic field. The amplitude and the width of ZBS as a function of in-plane field are shown in (f). The black dashed line is a Gaussian fit of the Ampl_{ZBS} as a function of B_{\parallel}	75
5.4	(a) Simulation of the I - V curve. The upper inset shows Energy diagram of the NIS junction. Showing Andreev reflections (light blue arrows) at NIS interface and normal reflections (black arrow) at the edge of the normal metal. The lower inset shows simulated I - V curve for different disorder strengths	77
5.5	(a-c) I - V curves and the differential conductance G for NIS_4,NIS_6 and NIS_8. The steps observed in the I - V characteristic are transformed in symmetric peaks in the differential conductance.	80

- 5.6 Devices simulated: The system is composed by a square lattice, on the left side we have the normal lead, that is represented by shaded spots that fade away from the device. Analogously, on the right side we have the superconducting lead, that is represented by red spots. The central region comprises also part of the superconducting lead. Impurities are modelled as a local shift of energy and are represented by some indicative white spot, whose size mimics the impurity strength. 81
- 5.7 (a) Conductance as a function of the voltage bias and (b) I-V characteristics of a 10 nm thick NIS junction with the geometry of Fig. 5.6 for several values of the disorder strength $U/t_0 = 0.0, 0.3, 0.6, 0.9, 1.2$. and the conductance has been averaged over 100 configuration for each voltage V . The device has $W = 100$, $L = 200$, $t_0 = 1$ eV, $t_1 = 0.015 t_0$, $\Delta = 0.005 t_0$ 83
- 5.8 (a) Color plot of the conductance as a function of the magnetic field B (abscissa) and the energy ϵ (ordinata). (b) Color plot of $\log G$, and (c) color plot of $\log G$ with a cutoff for values $G > 0.07$. Parameters of the simulations are $t_0 = 1$ eV, $\mu = -2.25 t_0$, $\Delta = 0.005 t_0$, $t_1 = 0.015 t_0$, $g^*/g = 27.6$, $a \simeq 5$ Å. 85
- 5.9 Study of the conductance for a slightly different geometry: $W = 20$ and $L = 40$ lattice sites. a) Conductance for two different values of $U/t_0 = 0, 0.8$. b) Color plot of the conductance as a function of the magnetic field B (abscissa) and the energy ϵ (ordinata) for the case $U = 0.8 t_0$. c) Device geometry. d) Scattering states of the ZBP for the $U = 0$ and $U = 0.8 t_0$ for two significant scattering channels. e) Scattering states of the FBP for a given scattering channel. The device is characterized by the following parameters: $t_0 = 1$ eV, $\mu = -2.25 t_0$, $\Delta = 0.1 t_0$, $t_1 = 0.01 t_0$, $g^* = 0$ 86
- 5.10 Logarithm of the absolute value of G as a function of the voltage bias for $P = -36$ dBm and $f' = 19.8$ GHz. The blue and the black traces are shifted copies of the original data (red trace). 88
- 5.11 (a) Logarithm of the absolute value of G as a function of P and voltage bias for two different frequencies f and f' . Black arrows indicate the different multiphoton absorption processes. (b) A cut of the color plot shown in (a) for $P = -36$ dBm and $f' = 19.8$ GHz, where one photon is absorbed and it creates a replica of the gap peak shifted by $V_n = hf'/e$. The peaks are narrow features, thus we highlighted them by averaging many cuts at different powers without losing the main features. (c) The averaged cut at $P = -60$ dBm, where the peaks are clearly visible without photon absorption features. (d) Comparison between the cuts shown in (b) and (c), to point out the different shapes between sub-gap peaks and photon absorption peaks. (e) Logarithm of the absolute value of G , showing multiphoton absorption for the two different frequencies. 89

- 5.12 (a-d) Logarithm of the absolute value of the differential conductance is shown as a function of B_{\perp} and voltage bias. Black arrows indicate the sweep direction of B_{\perp} . The grey dashed lines in (d) indicate two regions I and II of the analysis. (e) Vertical cuts of region II, showing the evolution of the gap. (f) Vertical cuts for the region I. 92
- 5.13 T_{step} as a function of the time after performing an adiabatic nuclear demagnetization. The black dashed line indicates the mean value of T_{step} in the time interval between 4 and 8 hours 93
- 6.1 (a) Schematic with CBT enclosed in a copper box (yellow), connected to Ag-epoxy microwave filters (grey), and glued onto a Cu plate (orange) with Ag-epoxy. (b) Electron micrograph (false color) of the CBT island (volume $\approx 42,000 \mu\text{m}^3$), with tunnel junctions (inside yellow rectangles) to adjacent Al/AlO_x/Al/Cu pads. The brown sections comprise very large areas, giving very low resistances of these large junctions. (c) Zoom-in of a tunnel junction from (b), showing the overlap (white rectangle) between the top layer (Al/Cu, brown) and the bottom layer (Al/AlO_x, blue). 98
- 6.2 (a) Bias dependence of the differential conductance g normalized with the high bias conductance g_T , shown for various Cu plate temperatures T_{Cu} . An in-plane field $B = 0.375 \text{ T}$ drives the Al thin films normal. The zero bias conductance (dark blue circle, measured after equilibrating at $T_{\text{Cu}} = 7 \text{ mK}$) remains clearly below the bias sweep (dark blue curve). (b) CBT temperature T_{CBT} versus T_{Cu} . The diagonal dashed line indicates ideal thermalization $T_{\text{CBT}} = T_{\text{Cu}}$. The inset shows the normalized zero bias conductance dip δg as a function of T_{Cu} . A fit using Eq. 6.1 is done over the high temperature, well thermalized regime $T_{\text{Cu}} \geq 30 \text{ mK}$ (solid black curve) and delivers the charging energy E_c of the device as the only fit parameter. The dashed curve indicates the low temperature extension below 30 mK of the fit with the same E_c 101
- 6.3 (a) Various temperatures as a function of the precooling time, as labeled. The inset shows a schematic of the thermal model. (b) Evolution of various temperatures during the AND process. Blue and orange dashed line indicate ideal cooling of CBT and Cu plates, respectively. (c) Warm up curves for various thermometers. The model is shown as black dashed curve for all panels. 103
- 6.4 (a-c) Differential conductance as a function of voltage bias (red data), shown for different temperatures as indicated. In addition, the differential conductance measured at zero bias as a function of time (data taken immediately after the corresponding bias scan) is shown in black, plotted versus the upper axis. (d) High bias ($V_{\text{bias}} = 1 \text{ mV}$) magnetoconductance g_T and its average value are shown in red and black, respectively. No magnetic field dependence is observed. 108
- 6.5 Warm up curves T_{CBT} and T_{Cu} for the CBT and the Cu plate, respectively, upon applying an external heat load of 100 nW/plate (for 3 different Cu plates). 111

-
- 6.6 (a) Differential conductance as a function of voltage bias, normalized to the high bias value, shown for 2 devices with different charging energy, and recorded at base temperature of the refrigerator. (b) Relative conductance dip size versus temperature for the two devices in (a). Dashed traces are curve fits to Eq.1 from the main text, used to extract the charging energy. (c) CBT temperature for both devices, measured as a function of applied magnetic field during the adiabatic nuclear demagnetization process. 113
- 6.7 (a) Logarithm of the absolute value of the noise spectrum as function of the frequency and magnetic field. A zoom-in of the frequency range between 135 Hz and 152 Hz is shown on the right hand side. (b) Vertical cut of (a) at 4 T. (c) Integrated noise of the spectrum shown in (b). A red arrow indicates a large increase in the noise level around 140 Hz. . . 115

Curriculum Vitae

Mario Palma, from Italy

Weidengasse 43,
Basel 4052 (CH)

11 June 1986 born in Caserta, Italy
2006 Diploma Indirizzo Scientifico Tecnologico with 97/100
 at Istituto Liceale Statale S.Pizzi Capua (Italy)
2006-2010 Bachelor Degree in Physics Sciences and Technology with 106/110
 at Università degli Studi di Napoli Federico II (Italy)
2010-2012 Master Degree in Physics with 110/110 cum laude
 at Università degli Studi di Napoli Federico II (Italy)
2013-2017 PhD student at University of Basel (Switzerland)

Publications

- A. V. Feshchenko*, L. Casparis*, I. M. Khaymovich, D. Maradan, O.-P. Saira, M. Palma, M. Meschke, J. P. Pekola, D. M. Zumbühl, *Tunnel-Junction Thermometry Down to Millikelvin Temperatures*, Phys. Rev. Appl. **4**, 034001 (2015)
- M. Palma*, D. Maradan*, L. Casparis, T.-M. Liu, F. N. M. Froning, D. M. Zumbühl, *Magnetic cooling for microkelvin nanoelectronics on a cryofree platform*, Rev. Sci. Instr. **88**, 043902 (2017)
- M. Palma, C. P. Scheller, L. Chiroli, T. Patlatiuk, L. Casparis, A. V. Feshchenko, D. Maradan, M. Meschke, J. P. Pekola, D. M. Zumbühl, *Sub-gap bound-states in normal metal-insulator-superconductor junctions*, in preparation for publication
- M. Palma*, C. P. Scheller*, D. Maradan, A. V. Feshchenko, M. Meschke, D. M. Zumbühl, *On-chip cooling of a Coulomb Blockade Thermometer down to 2.8 mK*, submitted to *Appl. Phys. Lett.* *arxiv:1708.09491*